NASA/TM—2020-220344

Plasma Reactor Summary

Anthony J. Colozza
Vantage Partners, LLC, Brook Park, Ohio

Timothy G. Gray and Bruce M. Steinetz
Glenn Research Center, Cleveland, Ohio

Lawrence G. Edwards
Vantage Partners, LLC, Brook Park, Ohio

Ian J. Jakupca
Glenn Research Center, Cleveland, Ohio

Charles Castle
Vantage Partners, LLC, Brook Park, Ohio

Don Johnson
Gilcrest Electric and Supply Company, Elyria, Ohio

Christopher C. Daniels
The University of Akron, Akron, Ohio

August 2020

NASA STI Program . . . in Profile

Since its founding, NASA has been dedicated to the advancement of aeronautics and space science. The NASA Scientific and Technical Information (STI) Program plays a key part in helping NASA maintain this important role.

The NASA STI Program operates under the auspices of the Agency Chief Information Officer. It collects, organizes, provides for archiving, and disseminates NASA's STI. The NASA STI Program provides access to the NASA Technical Report Server—Registered (NTRS Reg) and NASA Technical Report Server—Public (NTRS) thus providing one of the largest collections of aeronautical and space science STI in the world. Results are published in both non-NASA channels and by NASA in the NASA STI Report Series, which includes the following report types:

- TECHNICAL PUBLICATION. Reports of completed research or a major significant phase of research that present the results of NASA programs and include extensive data or theoretical analysis. Includes compilations of significant scientific and technical data and information deemed to be of continuing reference value. NASA counter-part of peer-reviewed formal professional papers, but has less stringent limitations on manuscript length and extent of graphic presentations.

- TECHNICAL MEMORANDUM. Scientific and technical findings that are preliminary or of specialized interest, e.g., "quick-release" reports, working papers, and bibliographies that contain minimal annotation. Does not contain extensive analysis.

- CONTRACTOR REPORT. Scientific and technical findings by NASA-sponsored contractors and grantees.

- CONFERENCE PUBLICATION. Collected papers from scientific and technical conferences, symposia, seminars, or other meetings sponsored or co-sponsored by NASA.

- SPECIAL PUBLICATION. Scientific, technical, or historical information from NASA programs, projects, and missions, often concerned with subjects having substantial public interest.

- TECHNICAL TRANSLATION. English-language translations of foreign scientific and technical material pertinent to NASA's mission.

For more information about the NASA STI program, see the following:

- Access the NASA STI program home page at http://www.sti.nasa.gov

- E-mail your question to help@sti.nasa.gov

- Fax your question to the NASA STI Information Desk at 757-864-6500

- Telephone the NASA STI Information Desk at 757-864-9658

- Write to:
  NASA STI Program
  Mail Stop 148
  NASA Langley Research Center
  Hampton, VA 23681-2199

NASA/TM—2020-220344

Plasma Reactor Summary

Anthony J. Colozza
Vantage Partners, LLC, Brook Park, Ohio

Timothy G. Gray and Bruce M. Steinetz
Glenn Research Center, Cleveland, Ohio

Lawrence G. Edwards
Vantage Partners, LLC, Brook Park, Ohio

Ian J. Jakupca
Glenn Research Center, Cleveland, Ohio

Charles Castle
Vantage Partners, LLC, Brook Park, Ohio

Don Johnson
Gilcrest Electric and Supply Company, Elyria, Ohio

Christopher C. Daniels
The University of Akron, Akron, Ohio

National Aeronautics and
Space Administration

Glenn Research Center
Cleveland, Ohio 44135

August 2020

Acknowledgments

We would like to acknowledge Christina Gerber for her editorial review.

Level of Review: This material has been technically reviewed by technical management.

Available from

NASA STI Program
Mail Stop 148
NASA Langley Research Center
Hampton, VA 23681-2199

National Technical Information Service
5285 Port Royal Road
Springfield, VA 22161
703-605-6000

This report is available in electronic form at http://www.sti.nasa.gov/ and http://ntrs.nasa.gov/

Contents

Plasma Reactor Summary

Anthony J. Colozza
Vantage Partners, LLC
Brook Park, Ohio 44142

Timothy G. Gray and Bruce M. Steinetz
National Aeronautics and Space Administration
Glenn Research Center
Cleveland, Ohio 44135

Lawrence G. Edwards
Vantage Partners, LLC
Brook Park, Ohio 44142

Ian J. Jakupca
National Aeronautics and Space Administration
Glenn Research Center
Cleveland, Ohio 44135

Charles Castle*
Vantage Partners, LLC
Brook Park, Ohio 44142

Don Johnson*
Gilcrest Electric and Supply Company
Elyria, Ohio 44035

Christopher C. Daniels
The University of Akron
Akron, Ohio 44325

Summary

A reactor was designed and constructed to generate a plasma and expose various materials to this plasma. The reactor was capable of heating the plasma chamber and supplying a gas to the chamber at pressures from vacuum levels to 200 psi. A calorimeter was constructed around the plasma chamber to accurately monitor the thermal power exiting the plasma chamber. A steady state or pulsed plasma could be generated. The input and output electrical power for creating the plasma was monitored and the current and voltage waveforms were observed and recorded using a series of oscilloscopes. A description of the plasma reactor operation and results from a demonstration test are provided. The results showed the accuracy of measuring the plasma input power and of the calorimeter in measuring the total heat output of the system. It was determined that the system had a total power measurement accuracy of ±1.36 percent.

*Currently retired.

1.0 Introduction

Two separate plasma reactors were designed and constructed to evaluate material properties and effects within a plasma environment. They were designated the glow discharge reactor and the plasma reactor. The glow discharge reactor used an anode and cathode pair and operated such that the plasma runs directly between the electrodes by forcing the plasma column to intersect with material placed between the electrodes. The chamber is made of Pyrex® to allow for visualization of the plasma during testing. The calorimeter used with the glow reactor is a Seebeck type where excess heat is measured by temperature rise of thermoelectric chips whose output is carefully calibrated using known controlled heat inputs. Any excess heat generated during the testing is measured by calculating the difference in the total output heat (determined by the Seebeck thermoelectric chips) less the total input heat (circulating fan plus plasma electrical heat). Calibrations indicated the system is able to resolve 0.15 W of power.

This report focuses on the design and operation of the plasma reactor, although there are similarities in the equipment used and operation of both plasma-generating systems. The plasma reactor test rig was designed with standard anode and cathode electrode pair contained inside of a stainless-steel reaction chamber. The entire system was designed to operate with pulsed direct current (DC) plasma at pressures from integer torr to several atmosphere gas pressures. The system was designed to handle most gas types but was mainly used with hydrogen, deuterium, or inert gases. The stainless-steel reactor is wrapped in a water-cooled calorimeter capable of dissipating upwards of 2,500 W of power. The calorimeter removes the total power inputted into the chamber as either heat or electrical power and any heat generated within the chamber. Any heat generated within the chamber is measured by calculating the difference in the total output heat (determined by the measured temperature rise for the metered water flow) less the total input power (strap on heaters plus plasma electrical power). Measurement uncertainty analysis indicated the system is able to resolve power to 1.36 percent of the total. The chamber is designed flexibly. The plasma column either runs directly between the two electrodes or is forced to interact through porous beds of metal foam disks with or without powders pre-impregnated therein. For materials testing, a range of powders and metal foam combinations can be used. Tests that utilized hydrogen or deuterium gas also introduced the possibility of gas loading into the materials. Some disks contained powders made of materials that had no hydrogen or deuterium loading and others contained hydrogen or deuterium at high atomic number density (e.g., 1,021 atoms/cm^3).

2.0 Plasma Reactor Design Summary

The plasma reactor consists of a reactor chamber, heater blocks, and integrated calorimeter. The reactor is set up so that plasma can be generated within the chamber between two electrodes. The reactor system is designed so that the total heat into and out of the reactor can be determined and monitored. The layout of the reactor is shown in Figure 1. This figure shows the main components of the system and their configuration.

The reactor operates by filling a chamber with a gas (such as, argon, hydrogen, or deuterium) at a specified pressure (from vacuum up to 200 psi). Plasma is formed within the chamber by applying a sufficient voltage potential across the two electrodes, located at either end, within the reaction chamber. This occurs due to the breakdown of the gas according to its Paschen curve. This breakdown voltage is dependent on the gas selected, its pressure, and the spacing between the electrodes (Ref. 1). The space between these electrodes is used to house various test materials and expose them to the plasma. If the material between the electrodes is conductive, then this will effectively change the spacing between the electrodes and affect the breakdown voltage. The Paschen curves for hydrogen and deuterium are given in Figure 2, and an estimate of the required breakdown voltage over a range of electrode spacing and pressure is given in Figure 3 for hydrogen gas.

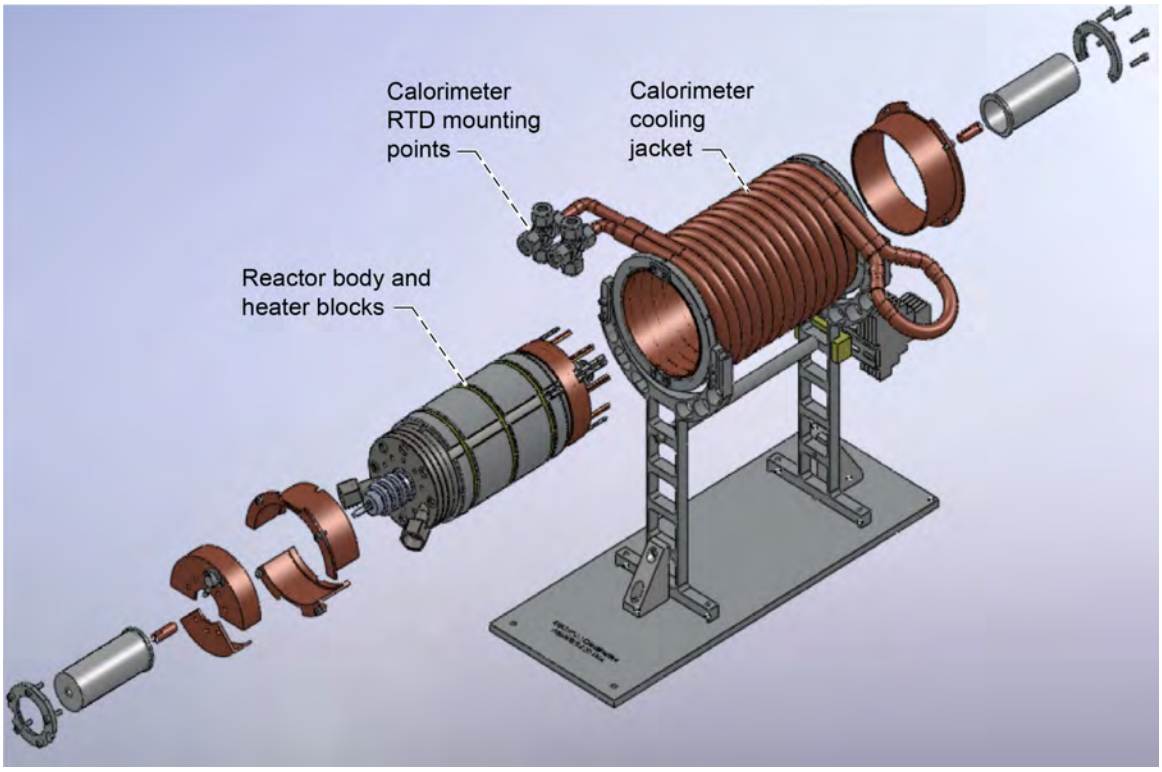

Figure 1.—Plasma reactor system main components. Resistance temperature detector (RTD).

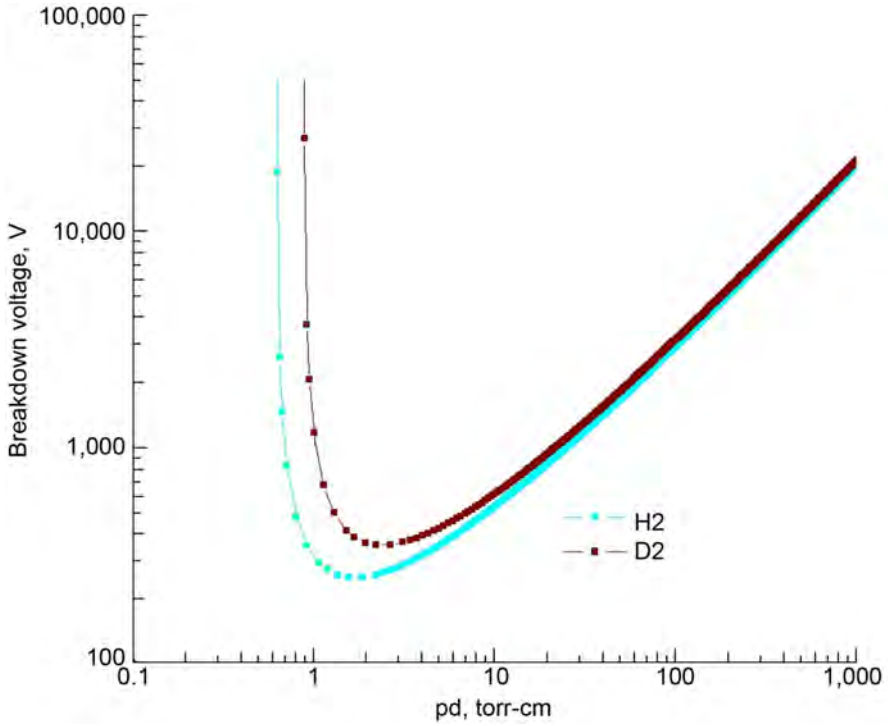

Figure 2.—Paschen breakdown curves for deuterium and hydrogen Reference 1.

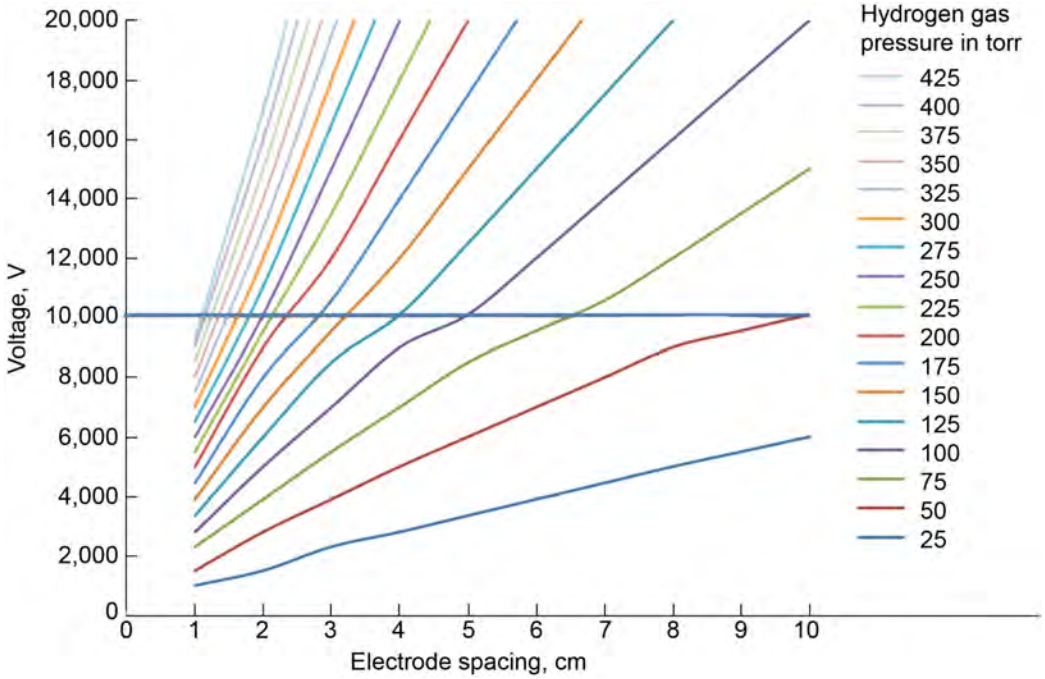

Figure 3.—Required breakdown voltage for hydrogen at different pressures.

Heater blocks are located along the outside of the reaction chamber. Four heater blocks are used each containing two cartridge heaters, as shown in Figure 4, for a total of eight heaters with a total heating capacity of 2 kW. The heaters are used to preheat the reaction chamber and to maintain the desired operating temperature during the testing.

A calorimeter is positioned around the outside of the heater blocks and reaction chamber, which consists of a coolant loop, and four resistance temperature detectors (RTDs) to measure the inlet and exit temperature of the coolant with mass flowmeters on both the inlet and outlet sides, as shown in Figure 5.

The system is also fully instrumented to monitor temperatures around the reactor body, cartridge heaters, outside of the coolant jacket, along the support stand legs, outside of the insulation wrap, and the ambient temperature near the test stand. This provides a detailed picture of the temperature distribution from the outside of the reactor to the test stand.

A diagram of the general internal layout for the reactor and its surrounding components is shown in Figure 6.

To determine the total heat generated within the reaction chamber during testing the total electrical input power to the reactor is monitored and subtracted from the total heat leaving the reactor, calculated from the RTDs and precision flowmeters, during the test. This difference between power in and power (heat) out determines the net power generated. The reactor is thermally isolated from the test stand and is heavily insulated during operation, as shown in Figure 7.

The reactor and calorimeter are located on a test stand that contains the ancillary equipment needed to operate the test and collect the data. This arrangement is shown in Figure 8.

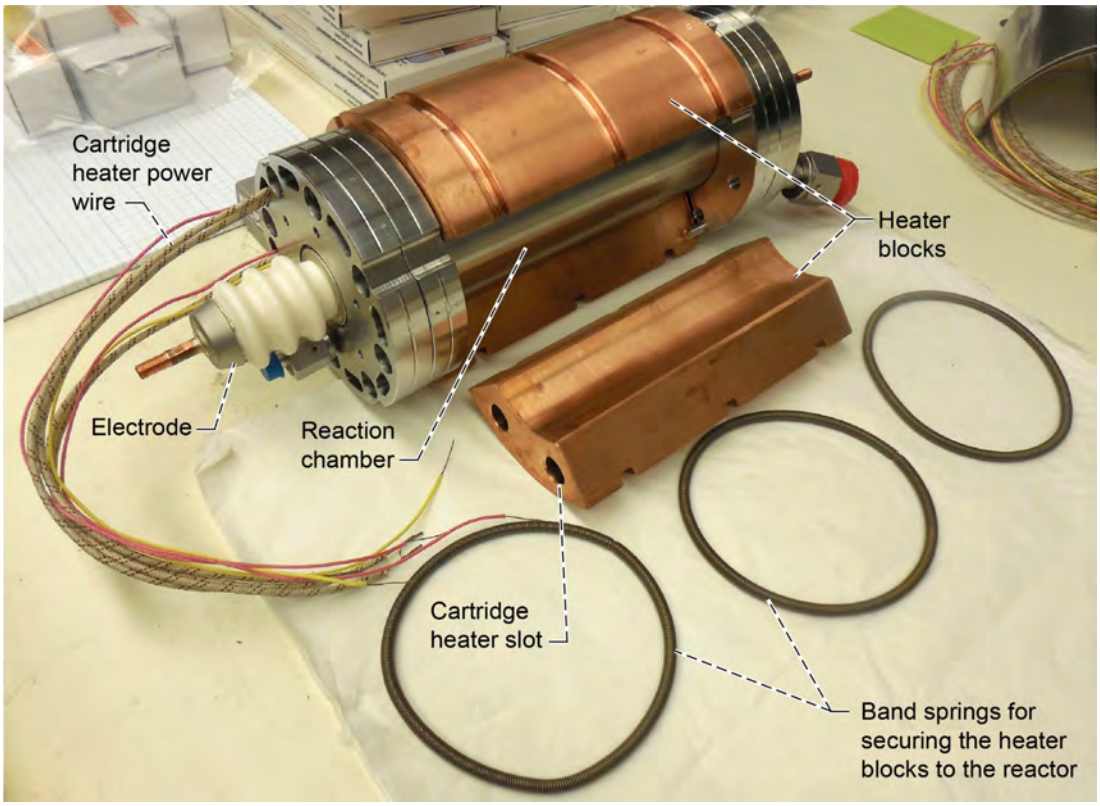

Figure 4.—Reactor chamber and heater blocks.

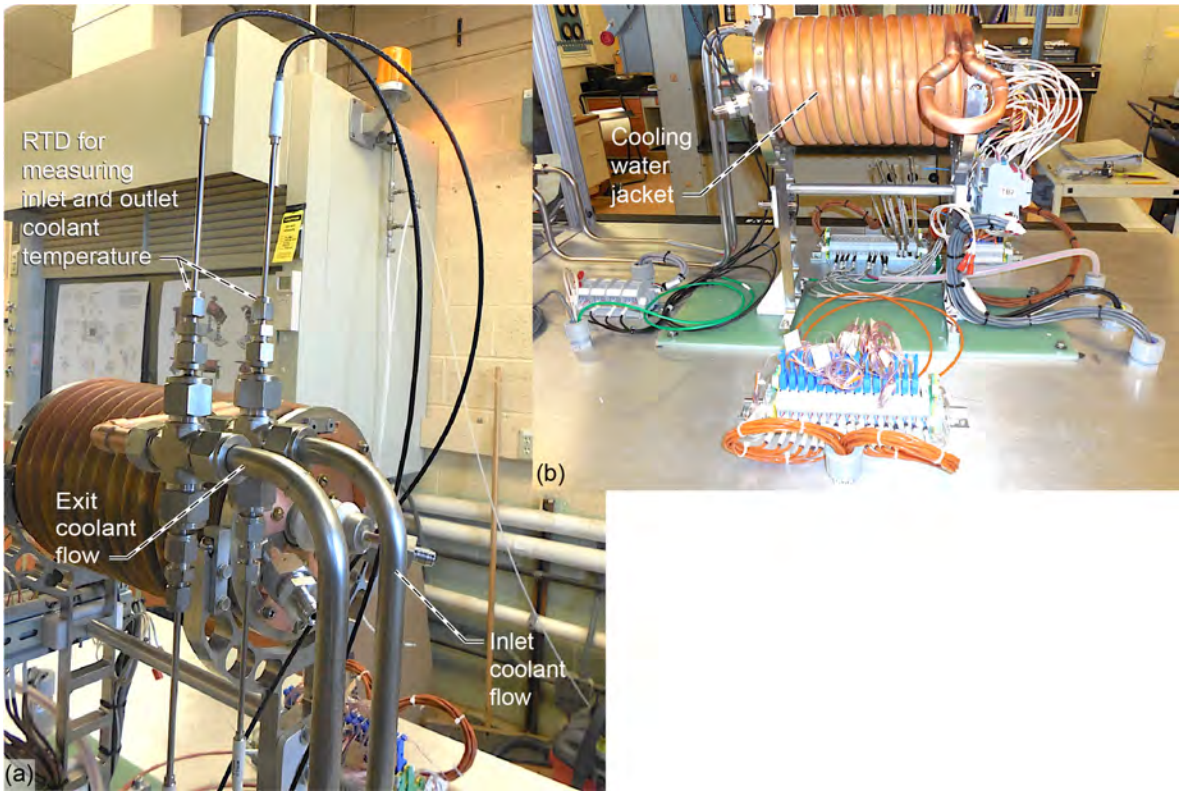

Figure 5.—Calorimeter cooling water jacket and resistance temperature detectors (RTDs). (a) Front view. (b) Side view.

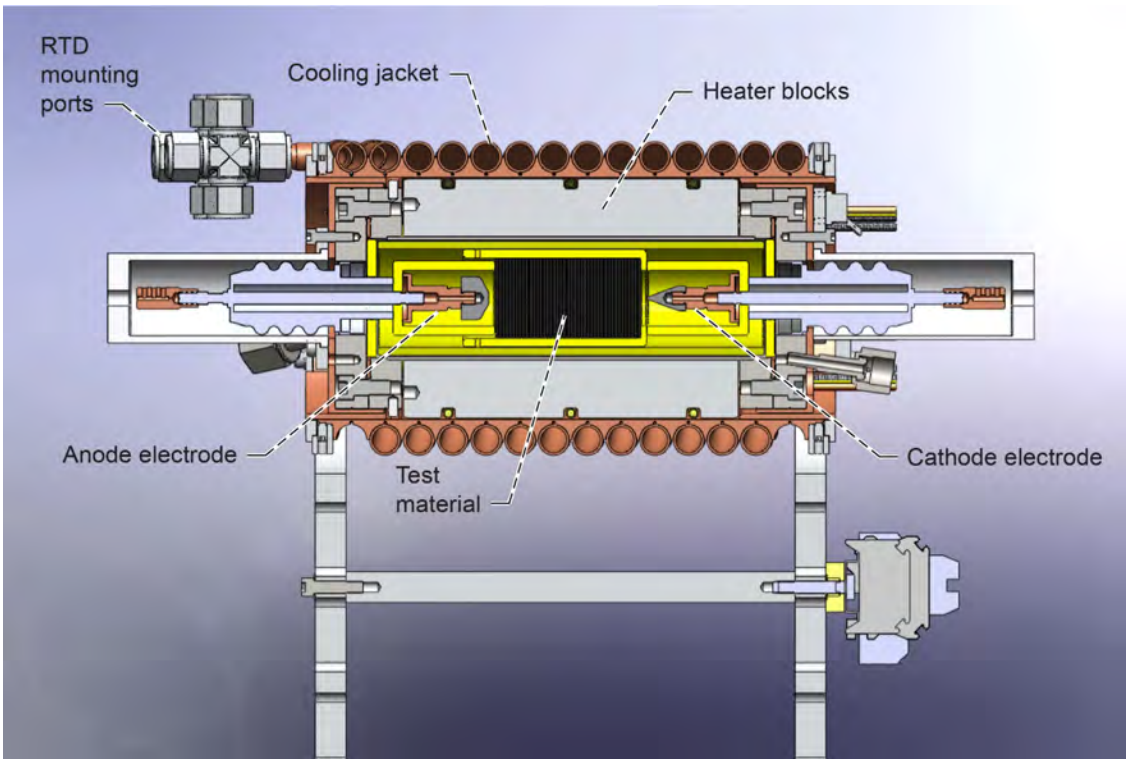

Figure 6.—Plasma reactor internal layout.

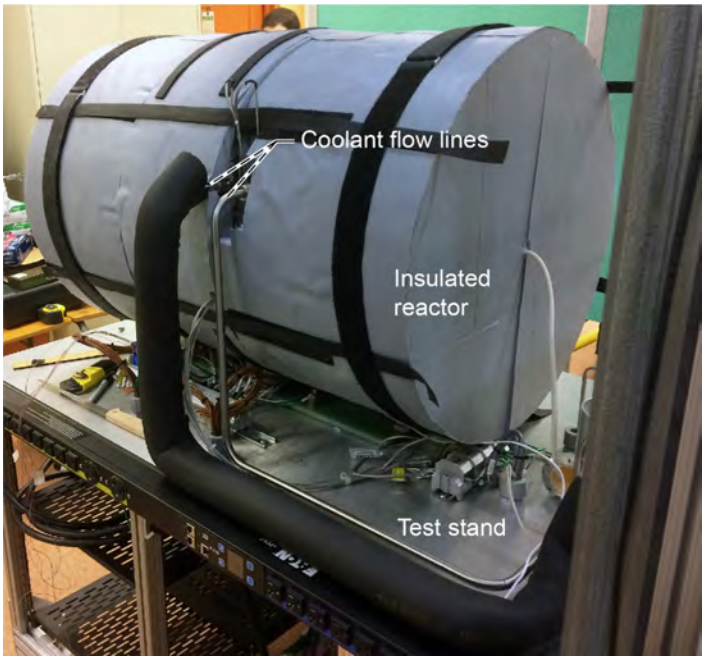

Figure 7.—Insulated plasma reactor and calorimeter cooling water jacket.

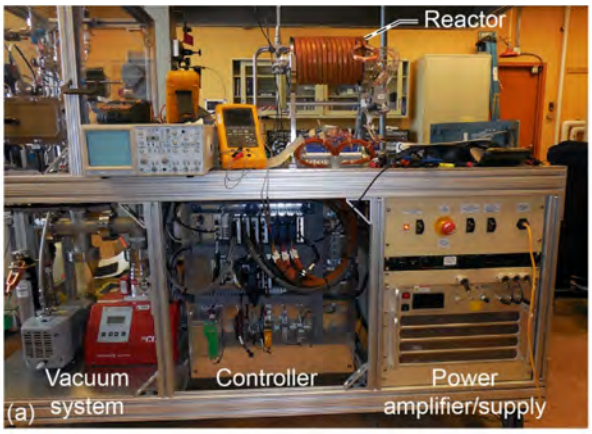

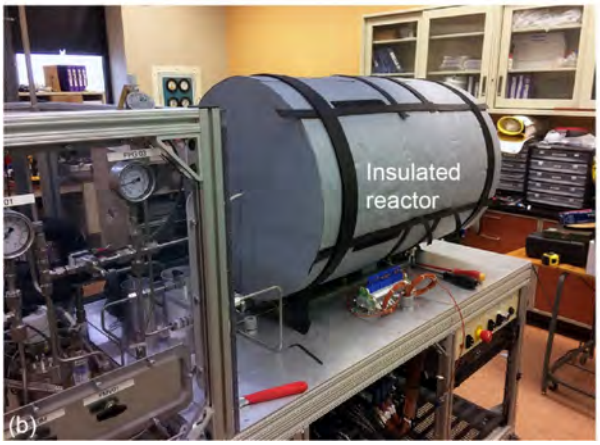

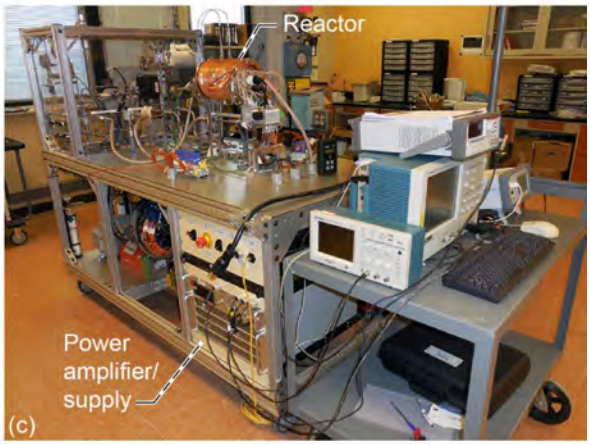

Figure 8.—Plasma reactor test stand. (a) Test stand side view. (b) Insulated reactor. (c) Test stand.

Figure 9.—Pfeiffer HiCube 80 high-vacuum pump.

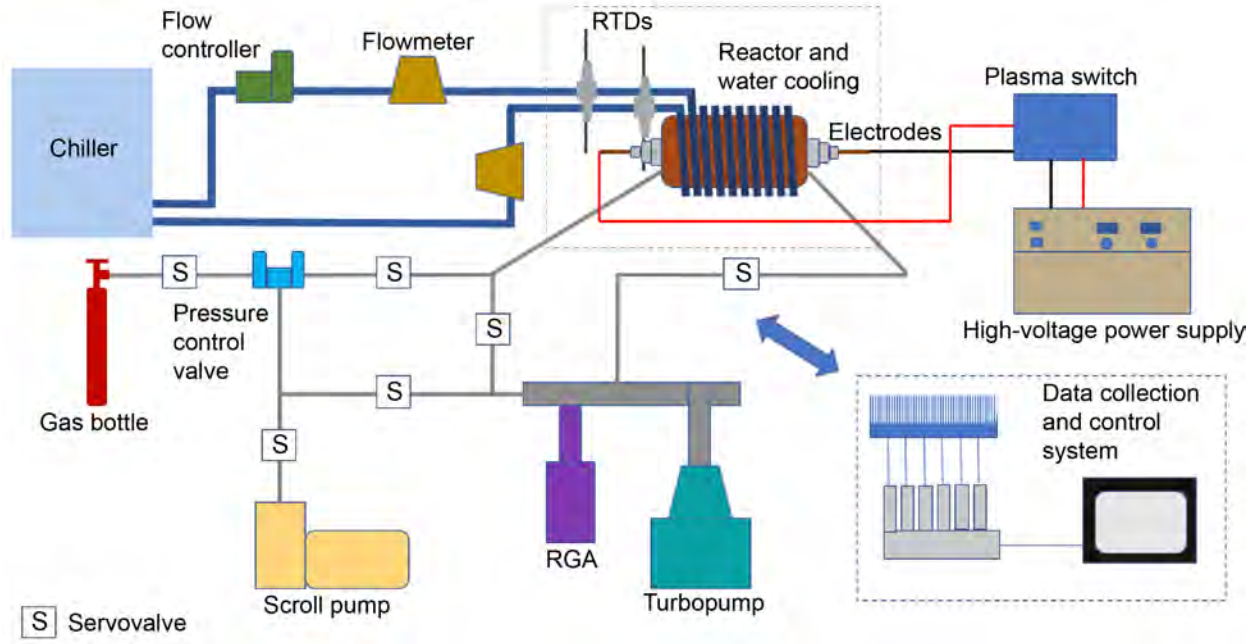

Figure 10.—Plasma reactor test stand general layout. Residual gas analyzer (RGA). Resistance temperature detector (RTD).

The ancillary equipment for operating the reactor includes the following items:

- Chiller (Section 3.2): for maintaining a constant input coolant temperature to the calorimeter cooling jacket.
- High-voltage pulsed power supply: to provide voltage to the electrodes in controlled pulses at a level sufficient to breakdown the gas within the chamber.
- Heater power supply: for powering the eight guard heaters located in the heater blocks around the reaction chamber.
- Vacuum pump system: consisting of a Pfeiffer HiCube 80 turbo pumping station, shown in Figure 9, scroll pump to evacuate the chamber prior to filling it with the test gas and maintain a low pressure sink for the gas pressure control valve, and a hard vacuum for the residual gas analyzer (RGA) operation.
- RGA (Section 6.0): used to sample the chamber gas during testing.
- Control system: used for data collection and control of the complete test stand.

A diagram showing their layout is given in Figure 10.

3.0 Instrumentation Summary

A number of different types of instrumentation and sensors are utilized to collect data and control the reactor operation. The sensors are monitored during the testing, displayed on the control screen, and recorded in the data file for future evaluation. The data from the sensors is collected by a National Instruments™ CompactRIO (cRIO) embedded control and data acquisition system. The cRIO data collection slot's layout, piping and instrumentation diagram (P&ID), is given in Appendix A. Details and specifications for all of the sensors and components utilized are given in Appendix B.

3.1 Temperature

The largest number of sensors are utilized to measure temperature. These are used to monitor temperature throughout the reactor system to ensure both that the desired temperatures are being achieved and that excessive temperatures do not occur that can damage components. This is accomplished with various types of thermocouples and RTDs. Some of the temperature measurement sensors and connections are shown in Figure 11.

There are 47 thermocouples on the reactor system components that are used to monitor temperatures and collect data. The four highest precision measurements are of the coolant water entering and leaving the reactor. Those measurements are taken by four RTDs, two each located on the inlet and exit cooling water line. The output from the RTDs is shown in Figure 12. The next series of temperature measurements are on the exterior of the cooling water jacket. These utilize type-T thermocouples. A total of six temperature measurements are made on the cooling jacket. An example of these temperatures are shown in Figure 13.

The cooling jacket was designed with a counter flow arrangement as illustrated in Figure 14, so that the cooling water temperature would be as uniform as possible when moving through the jacket. This was done to try to minimize any hotspots that could occur within the reactor system. Figure 13 shows that after the initial reading, the cooling jacket temperature, and in turn the cooling water temperature, is fairly uniform over the complete cooling jacket surface.

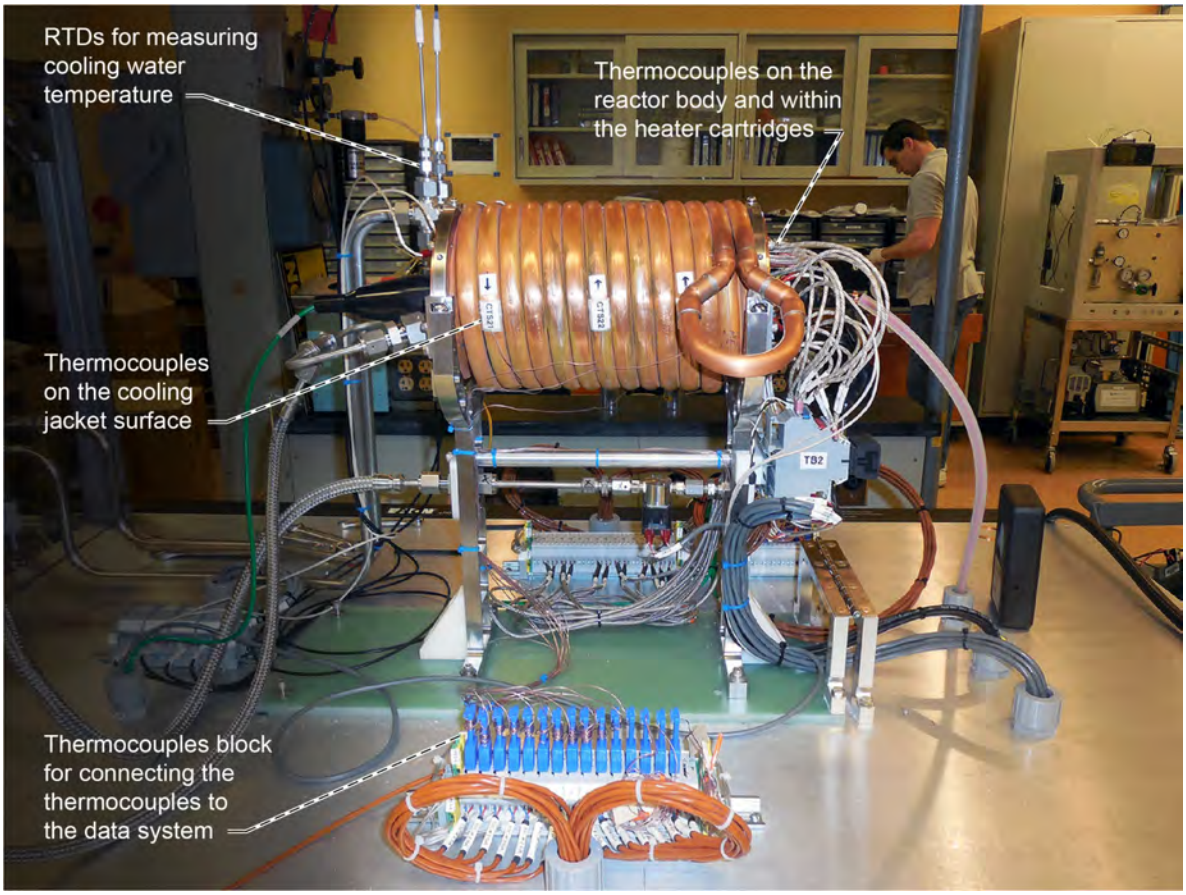

Figure 11.—Temperature measurement on the reactor. Resistance temperature detectors (RTDs).

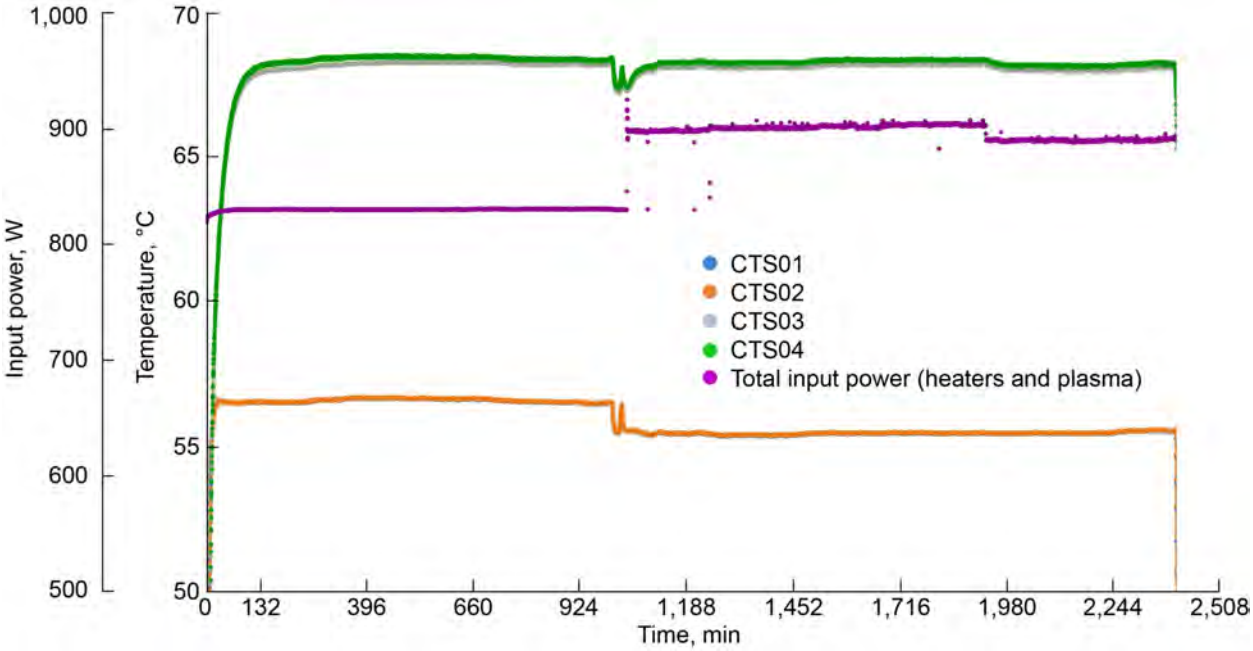

Figure 12.—Resistance temperature detector coolant water temperature measurements and corresponding locations: CTS01: inlet top, CTS02: inlet bottom, CTS03: exit top, CTS04: exit bottom.

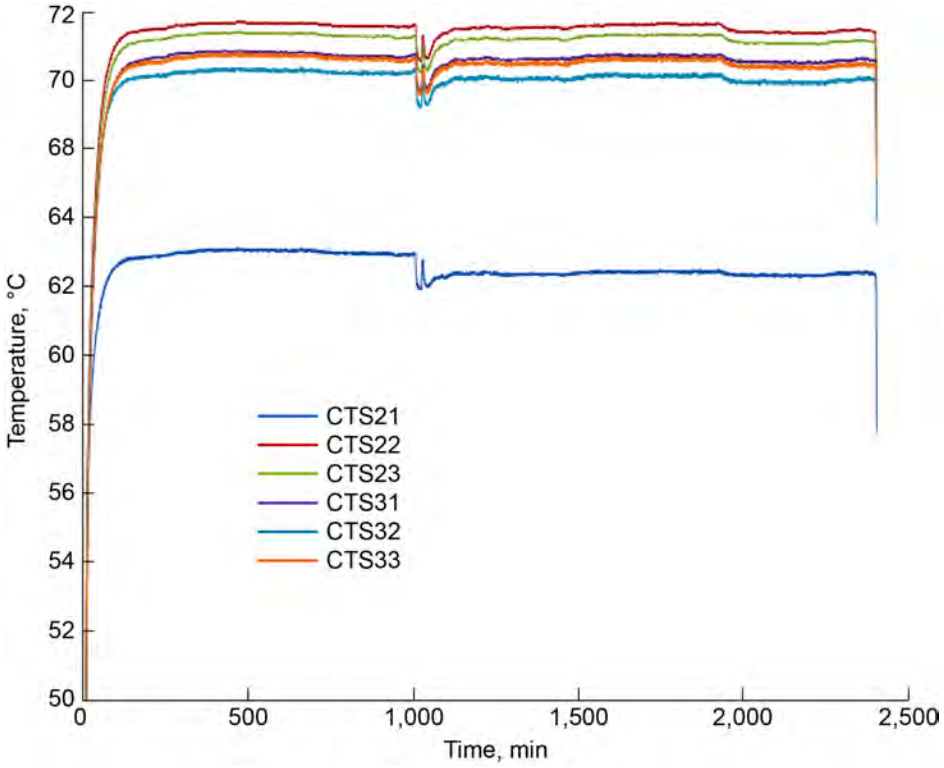

Figure 13.—Cooling jacket temperatures and corresponding locations: CTS21: side A, forward location, CTS22: side A, mid location, CTS23: side A, aft location, CTS31: side B, forward location, CTS32: side B, mid location, CTS33: side B, aft location.

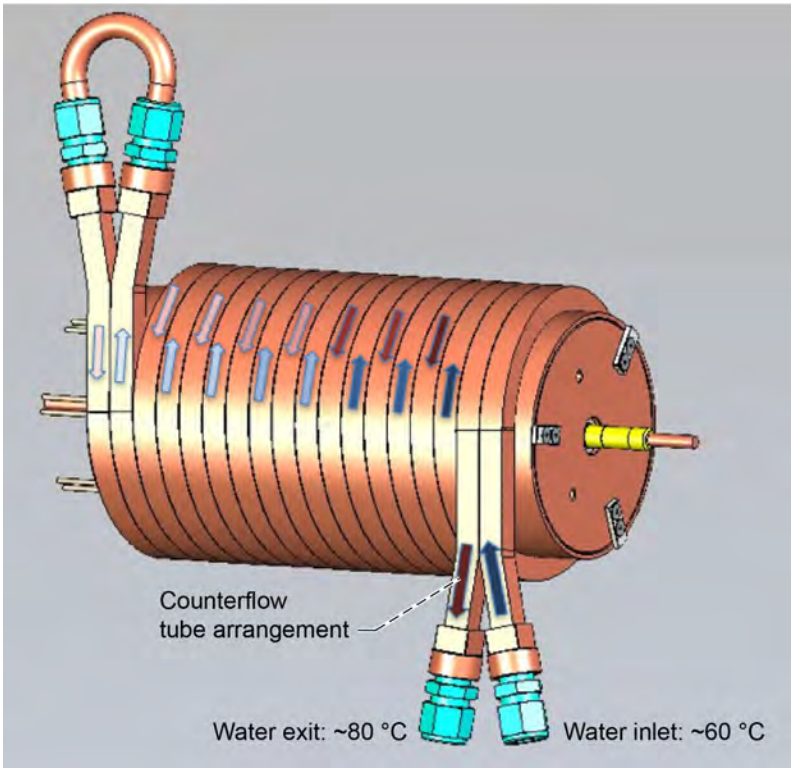

Figure 14.—Calorimeter coolant flow path. Note: Though figure shows square coolant flow tubes, final design utilized standard round tubes simplifying fabrication and helping meet schedule demands.

The calorimeter's cooling jacket was instrumented with six thermocouples. These were located on the sides, three on each side. Side A is the right side or the side opposite where the cooling lines connect. Whereas, side B is the left side where the cooling line connections are located. The thermocouples were distributed horizontally along the side, termed forward, mid, and aft with forward being closest to where the cooling lines connect. The six thermocouples are identified in the Figure 13 caption. From Figure 13, it can be seen that thermocouple CTS21 is registering a significantly lower temperature then the other five thermocouples, well outside the ±1 °C measurement error of the thermocouple. This lower temperature is due to the thermocouple being located on the cooling line closest to the inlet water connection and therefore registers a lower temperature then the others.

The tube size for the cooling jacket was selected so that the internal flow would transition from laminar to turbulent approximately three-quarters of the way through the tube for a flow rate 0.66 L/min. The transition location was used as a means of increasing or decreasing the heat transfer from the reactor to the calorimeter. By speeding up the coolant flow, the transition location would occur earlier in the tube and thereby increase the overall heat transfer to the coolant. Conversely, if the flow rate was reduced, the transition point would move further down the tube reducing the heat transfer rate to the coolant. This provided considerable control over the ability to remove heat over a wide range while maintaining a relatively constant internal temperature within the reactor.

The ends of the reactor are not directly cooled. Conductive copper caps are made to fit over the reactor end flanges and slide under the cooling jacket. These caps are used to conduct heat from the end flanges to the cooling jacket. Because the ends are not directly cooled, their temperature will be higher than the cooling jacket temperature. The reactor flange temperatures are measured using four type-K thermocouples, two on each end, as identified in the Figure 15 caption.

These temperatures are shown in the figure. Because the end flanges have different components and pass-through ports on them, the conduction paths to the cooling jacket are not the same. Therefore, temperatures on the end flanges differ at different locations. This causes about a 10 °C variation in the end flange temperatures. The top thermocouples were placed on the end faces above the centerline at the 12 o'clock position and the bottom thermocouples were located at the 6 o'clock position. The location of the end flange thermocouples is illustrated in Figure 16.

The hottest parts of the reactor system are the reactor body itself and the heater blocks. The stainless-steel reactor body temperatures are shown in Figure 17. The reactor has eight type-K thermocouples attached to its surface bolted with screws welded to the reactor surface. These thermocouples are located in the gaps between the heater blocks as shown in Figure 4 and illustrated in Figure 16. There are two thermocouples in each of the gaps between the four heater blocks. There is approximately a 40 °C range in the temperature measurements on the reactor. This is likely due to variations in the heater block output, and the differences in the thermal contact resistance between the different heater blocks as well as on the surface of a given heater block.

The heater block temperatures are shown in Figure 18. These temperatures are measured from a type-K thermocouple mounted inside the heater cartridge. The heater block temperatures follow a similar pattern to those for the reactor body. They were approximately 75 °C higher than the reactor body and had a variation between the blocks of approximately 30 °C.

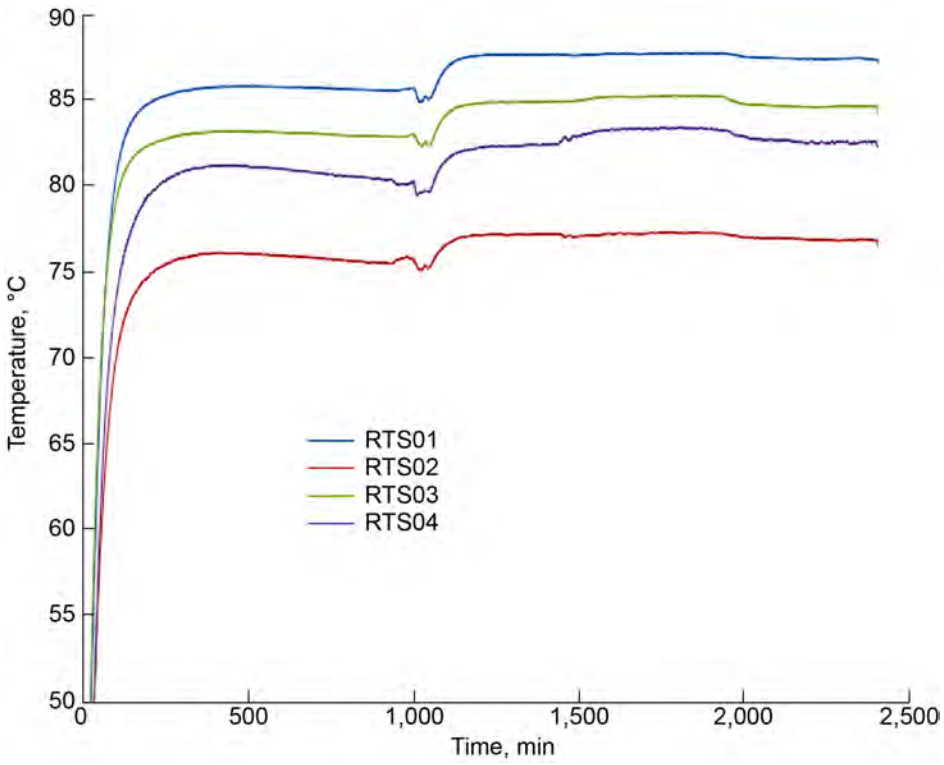

Figure 15.—Reactor end flange temperatures and corresponding locations: RTS01: forward face top, RTS02: forward face bottom, RTS03: aft face top, RTS04: aft face bottom.

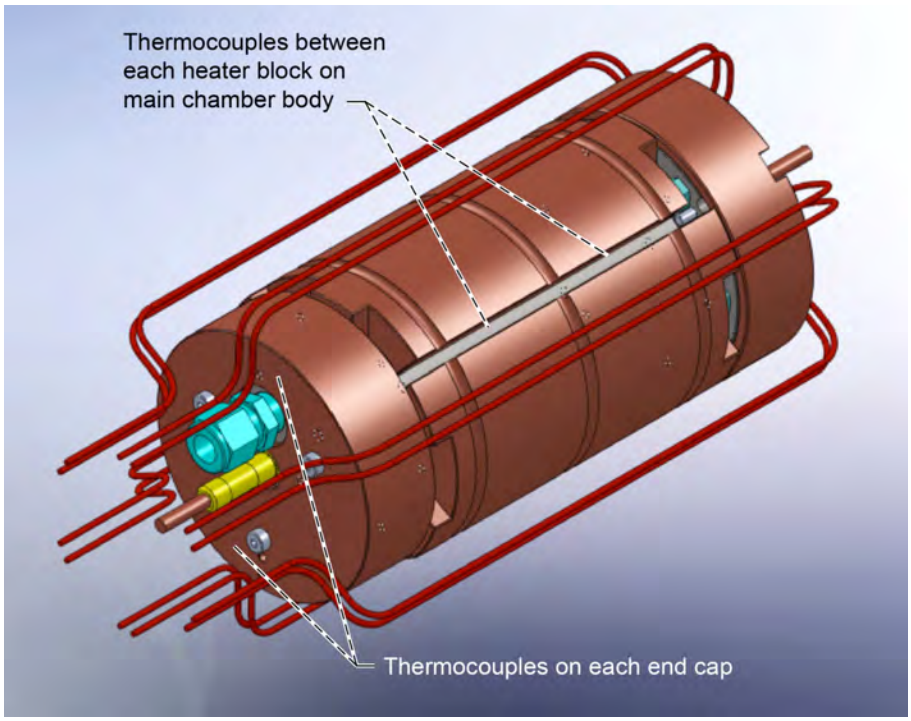

Figure 16.—Reactor body temperature measurement using type-K thermocouples.

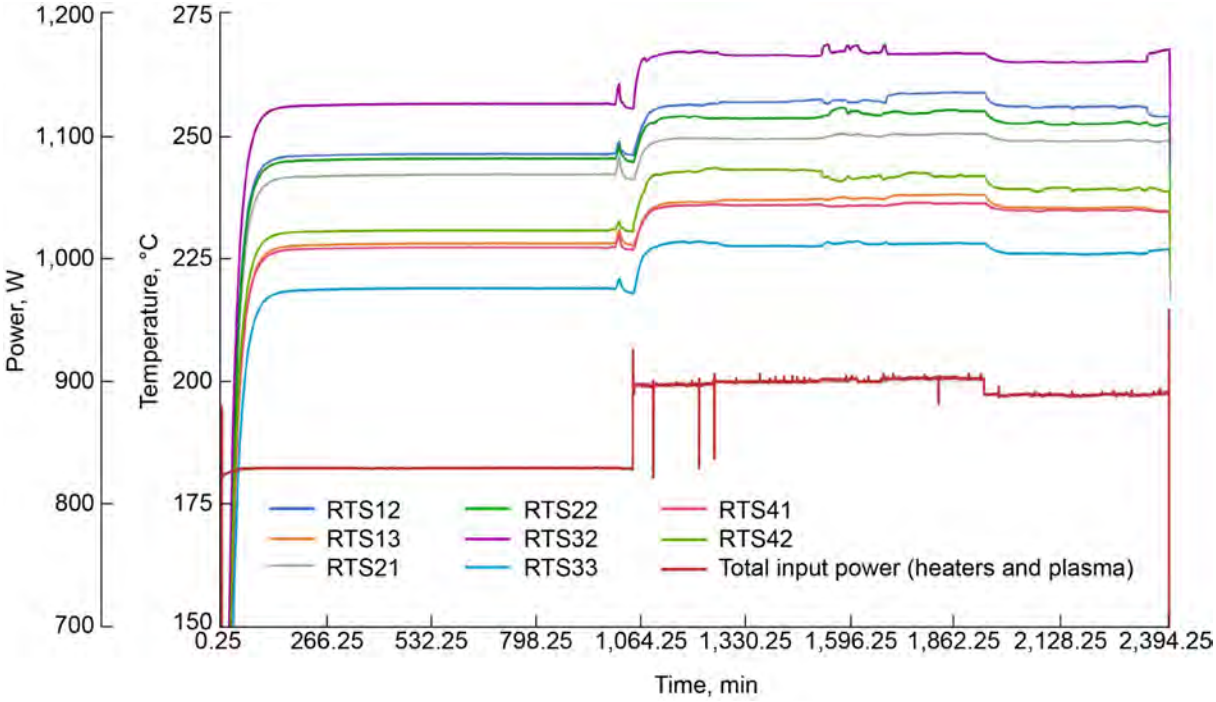

Figure 17.—Reactor body temperatures.

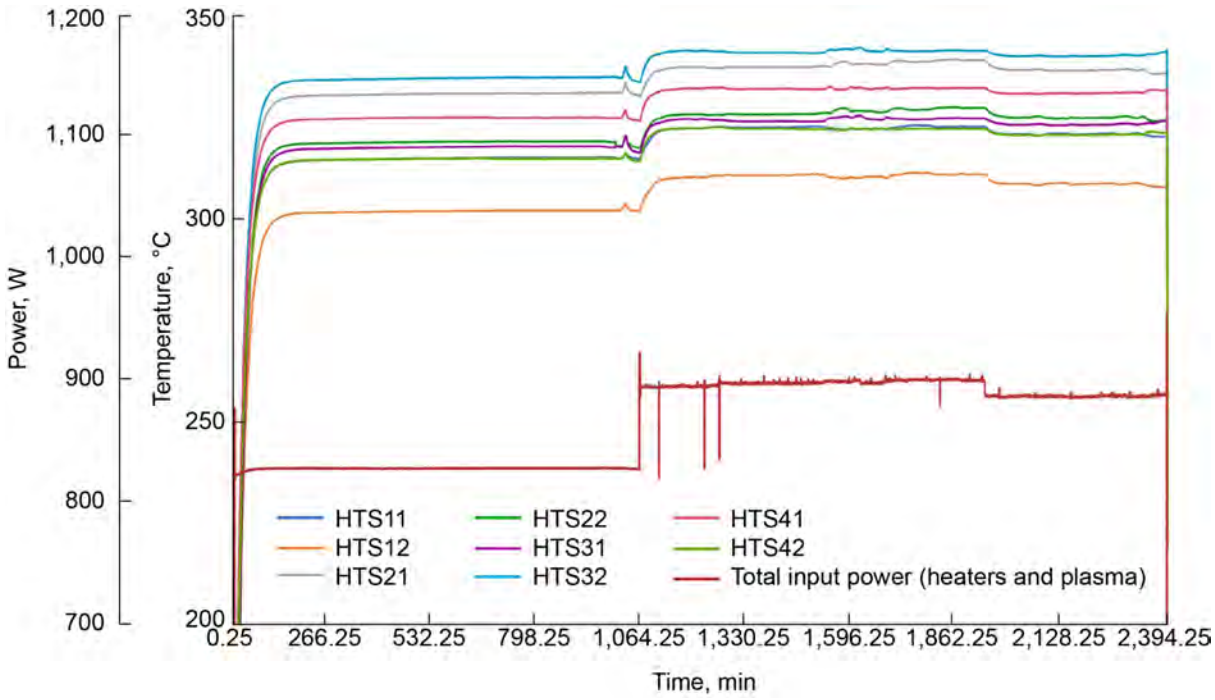

Figure 18.—Heater block temperatures.

The remaining thermocouples measure temperature of the components in contact with the reactor and cooling jacket exterior. These components consisted of the support frame and the insulation, and were measured using type-T thermocouples. The insulation measurements, using type-K thermocouples, are distributed over the surface of the insulation, three along each side (six total) and two on each end (four total) as illustrated in Figure 19. The insulation and ambient room temperature measurements are given in Section 8.0 for the example test results. The support structure thermocouple readings are given in Figure 20, where companion measurements are made for both support structure legs. These readings show a clear gradient in temperature down the support structure from near the reactor to the test stand cart top surface where the reactor is mounted. The support structure was constructed of 304 stainless steel, with a thermal conductivity of 19 W/mK, to help minimize the heat losses through the structure. The placement of the thermocouples on the support stand is illustrated in Figure 21.

The heat loss through the insulation was estimated to be 6.6 W based on the data from the heat loss through the insulation and the surface area of the insulation (2.3 m^2). This heat loss assumes natural convection from the insulation surface and a room air temperature of 22 °C. This analysis and the insulation temperature data is discussed further in Section 8.0.

A list of the temperature sensors utilized in the test stand is summarized in Table 1. This table shows the type of temperature sensor, the manufacturer's listed accuracy of the temperature measurement, and the general location of the temperature sensor.

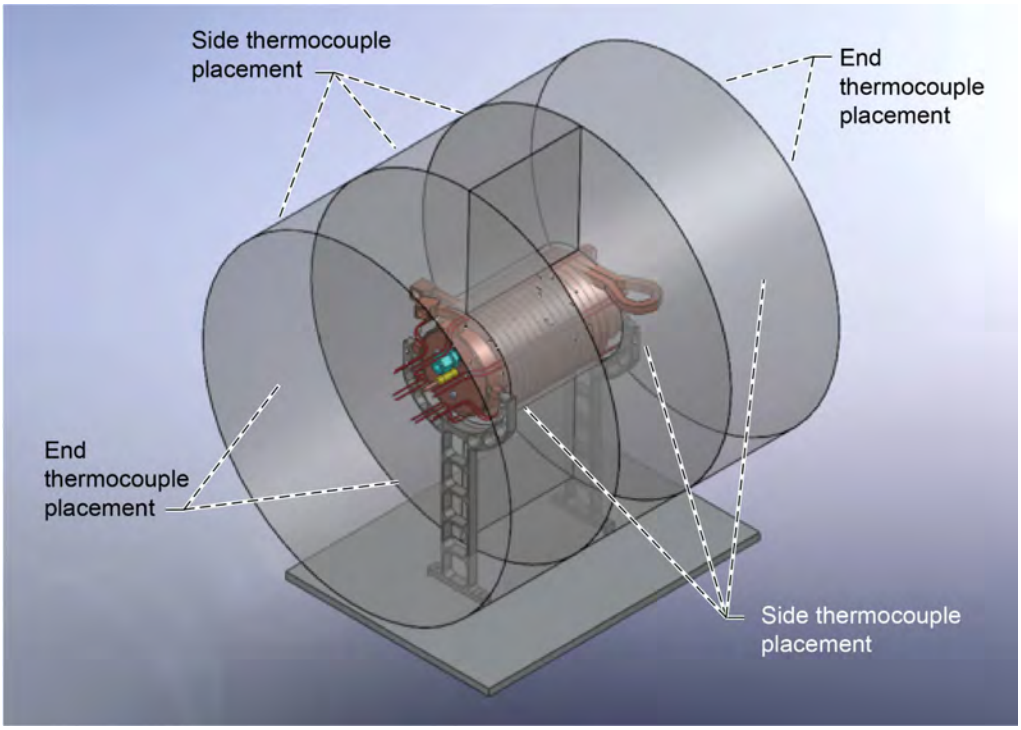

Figure 19.—Insulation type-K thermocouple placement.

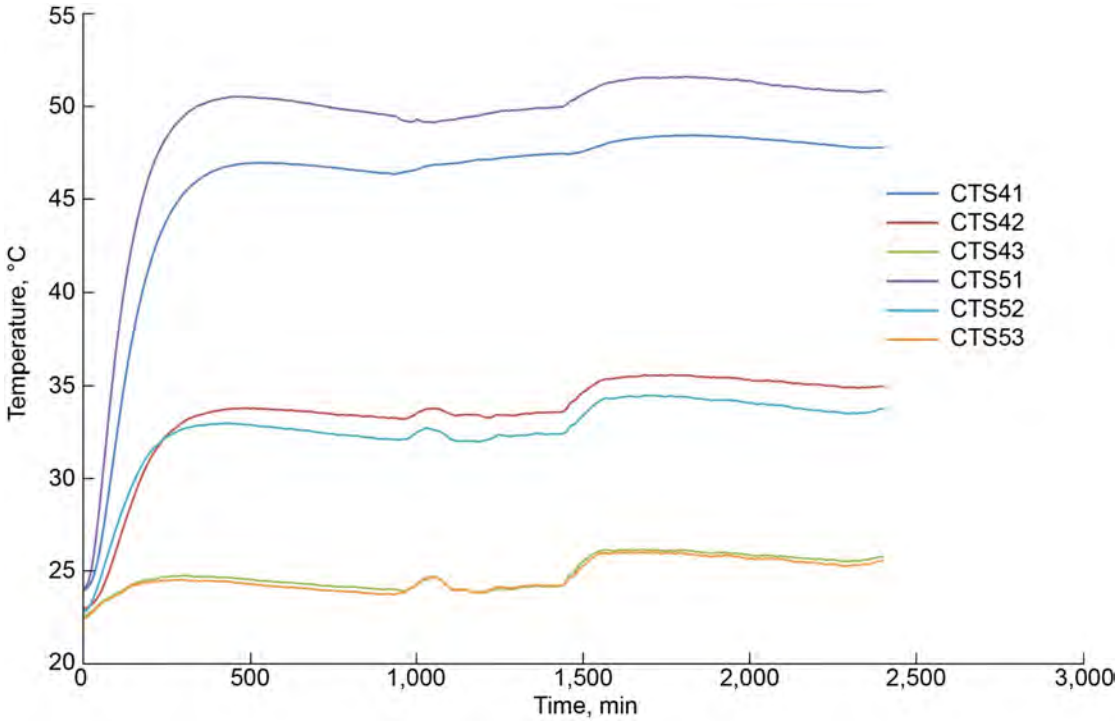

Figure 20.—Support structure thermocouple measurements.

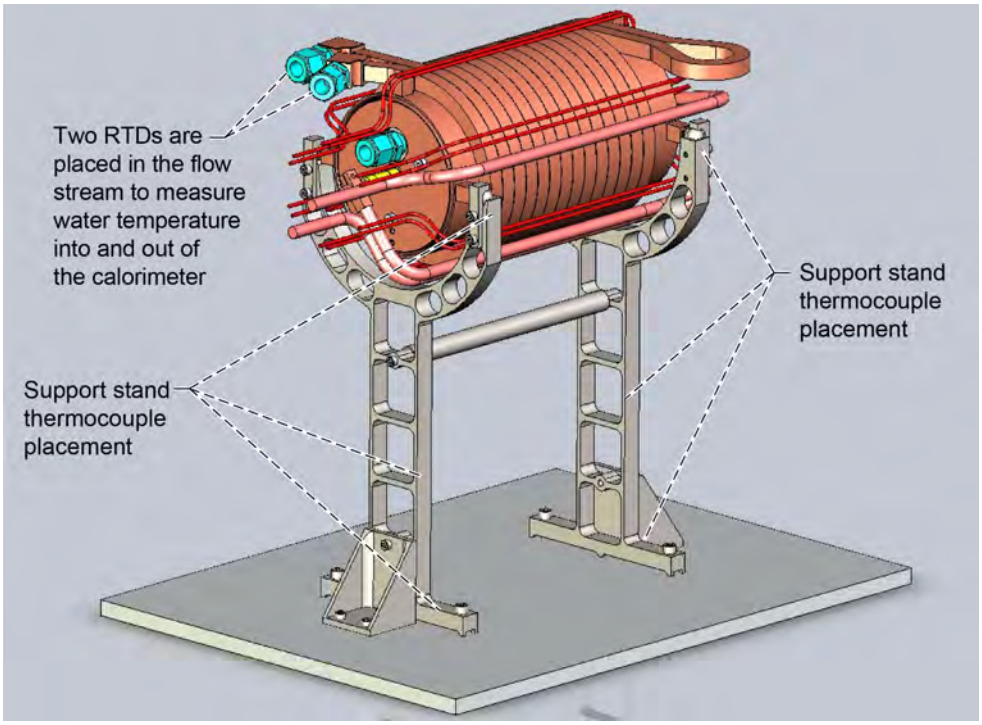

Figure 21.—Support stand type-K thermocouple placement. Resistance temperature detector (RTD).

TABLE 1.—TEMPERATURE SENSOR LIST

Sensor	Thermocouple type[a]	Accuracy, ±°C	Location
CTS21	T	1.0	Cooling jacket surface
CTS22	T	1.0	Cooling jacket surface
CTS23	T	1.0	Cooling jacket surface
CTS31	T	1.0	Cooling jacket surface
CTS32	T	1.0	Cooling jacket surface
CTS33	T	1.0	Cooling jacket surface
CTS41	T	1.0	Support structure
CTS42	T	1.0	Support structure
CTS43	T	1.0	Support structure
CTS51	T	1.0	Support structure
CTS52	T	1.0	Support structure
CTS53	T	1.0	Support structure
CTS61	T	1.0	Insulation surface
CTS62	T	1.0	Insulation surface
CTS63	T	1.0	Insulation surface
CTS71	T	1.0	Insulation surface
CTS72	T	1.0	Insulation surface
CTS73	T	1.0	Insulation surface
CTS81	T	1.0	Insulation surface
CTS82	T	1.0	Insulation surface
CTS91	T	1.0	Insulation surface
CTS92	T	1.0	Insulation surface
RTS12	K	1.2	Reactor surface
RTS13	K	1.2	Reactor surface
RTS21	K	1.2	Reactor surface
RTS22	K	1.2	Reactor surface
RTS32	K	1.2	Reactor surface
RTS33	K	1.2	Reactor surface
RTS41	K	1.2	Reactor surface
RTS42	K	1.2	Reactor surface
RTS01	K	1.2	Reactor end flange
RTS02	K	1.2	Reactor end flange
RTS03	K	1.2	Reactor end flange
RTS04	K	1.2	Reactor end flange
HTS11	K	1.2	Heater cartridge
HTS12	K	1.2	Heater cartridge
HTS21	K	1.2	Heater cartridge
HTS22	K	1.2	Heater cartridge
HTS32	K	1.2	Heater cartridge
HTS33	K	1.2	Heater cartridge
HTS41	K	1.2	Heater cartridge
HTS42	K	1.2	Heater cartridge
CTS01	RTD	.1	Inlet coolant flow
CTS02	RTD	.1	Inlet coolant flow
CTS03	RTD	.1	Exit coolant flow
CTS04	RTD	.1	Exit coolant flow
AT01	T	1.0	Ambient

[a]Resistance temperature detector (RTD).

3.2 Coolant Flow

A chiller is used to provide temperature-controlled cooling water to the calorimeter. The chiller utilized is a Thermo Scientific NESLAB ThermoFlex™ 7500 Deluxe recirculating chiller, shown in Figure 22. It has a cooling capacity of up to 8 kW with a coolant flow pumping rate of 4.0 gal/min at 60 psig. The chiller's cooling water temperature control is ±0.1 °C.

The coolant flow from the chiller is monitored and controlled by two FTI Flow Technologies™ FTO turbine high-precision flowmeters and an Alicat Scientific flow control valve. The coolant return flowmeter (CFM02) was utilized in calculating the net output power of the calorimeter. The output of this flowmeter is shown in Figure 23. The flowmeter output is stable throughout the operating time. Slight changes in the output are due to fluctuations in the chiller and are within the flow rate specifications of the chiller.

Figure 22.—Thermo Scientific NESLAB ThermoFlex™ 7500 recirculating chiller.

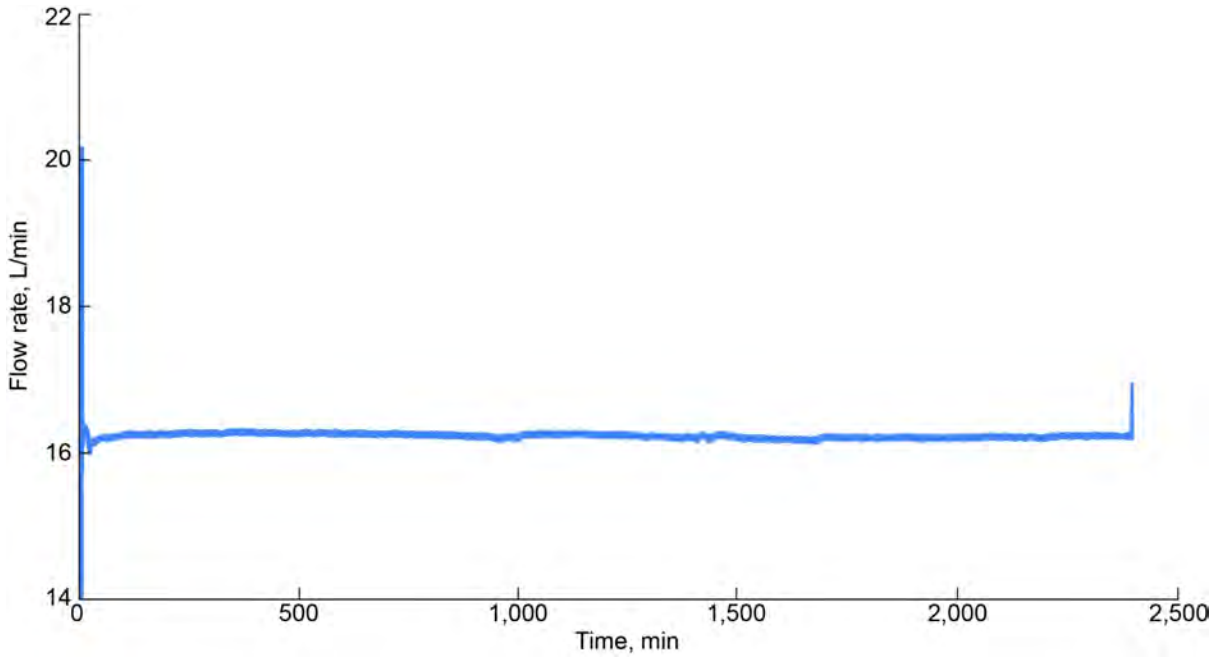

Figure 23.—Coolant return flowmeter (CFM02) output.

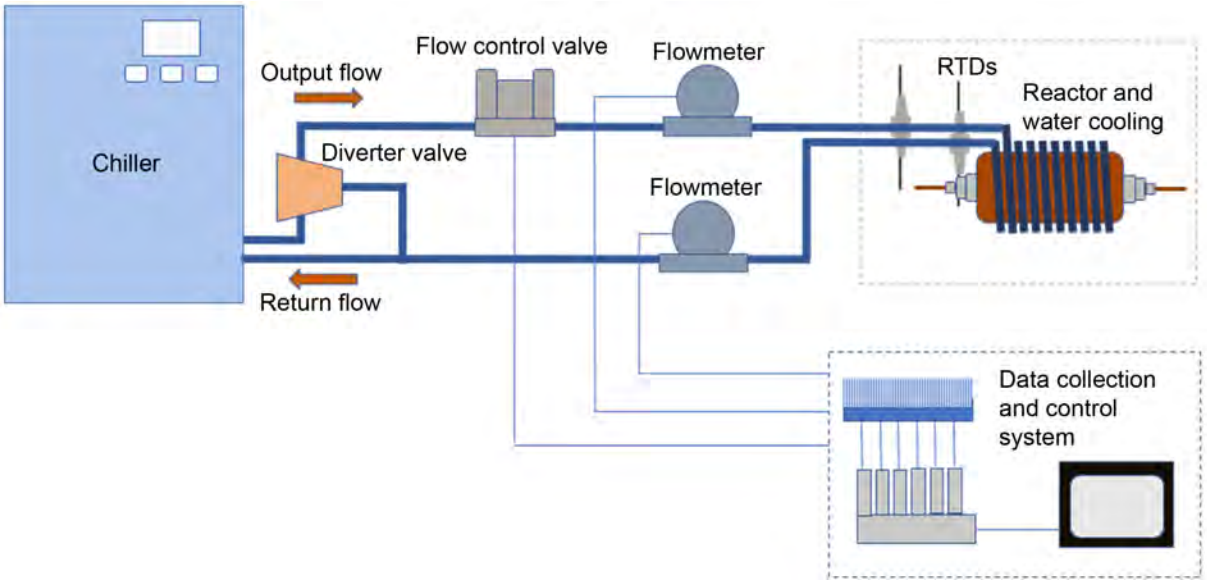

Figure 24.—Coolant system layout. Resistance temperature detectors (RTDs).

The layout of the coolant flow system is illustrated in Figure 24. The chiller has a constant flow output based on the pressure drop in the fluid line. This flow rate is too high for the coolant system so a diverter valve is used to bleed off only a small portion of the chiller output to flow through the calorimeter. The remainder is redirected back into the chiller. In addition, a flow control valve is in line with the chiller output after the diverter valve. This flow control valve is used to maintain a near constant flow rate through the calorimeter and to compensate for fluctuations in the chiller output flow rate. The

flowmeters, reading mass flow on both the inlet and outlet to the cooling jacket, are used as redundant measurements for the calorimeter output power calculation. Data from the flowmeters and flow control valve are collected by the data system.

3.3 Heater Power

The power supplied to the heaters is monitored and recorded in the data file during the testing. The heater power is set through the control system by selecting the current level for the combined four heater blocks on the control panel. The heater blocks are wired in parallel from the heater power supply. Whereas, the individual heater cartridges in each heater block are wired in series. This arrangement is illustrated in Figure 25. Once the current level is selected, the heater power supply voltage rises to meet the specified current level based on the resistance of the heater cartridges. The voltage and current measurements are made near the heater blocks to reduce the effects of line losses on the input heater power measurements. The voltage of the heaters is based on the ground reference from the power supply. For normal baseline operation, a current level of 1.3 A is selected. This current level will provide about 825 W of combined heater power from all four heater blocks. The current input to the four heater blocks for the baseline operation is shown in Section 7.0 along with the average voltage input to the heaters. The individual heater block voltage is shown in Figure 26. From these figures, it can be seen that the current and voltage to the heaters is fairly stable throughout a test. There is a variation of approximately 1.5 V or 2 W between the highest and lowest heater block values. This is due to slight differences in the resistances of the heaters. The accuracy of the heater power input measurement is discussed in Section 3.2.

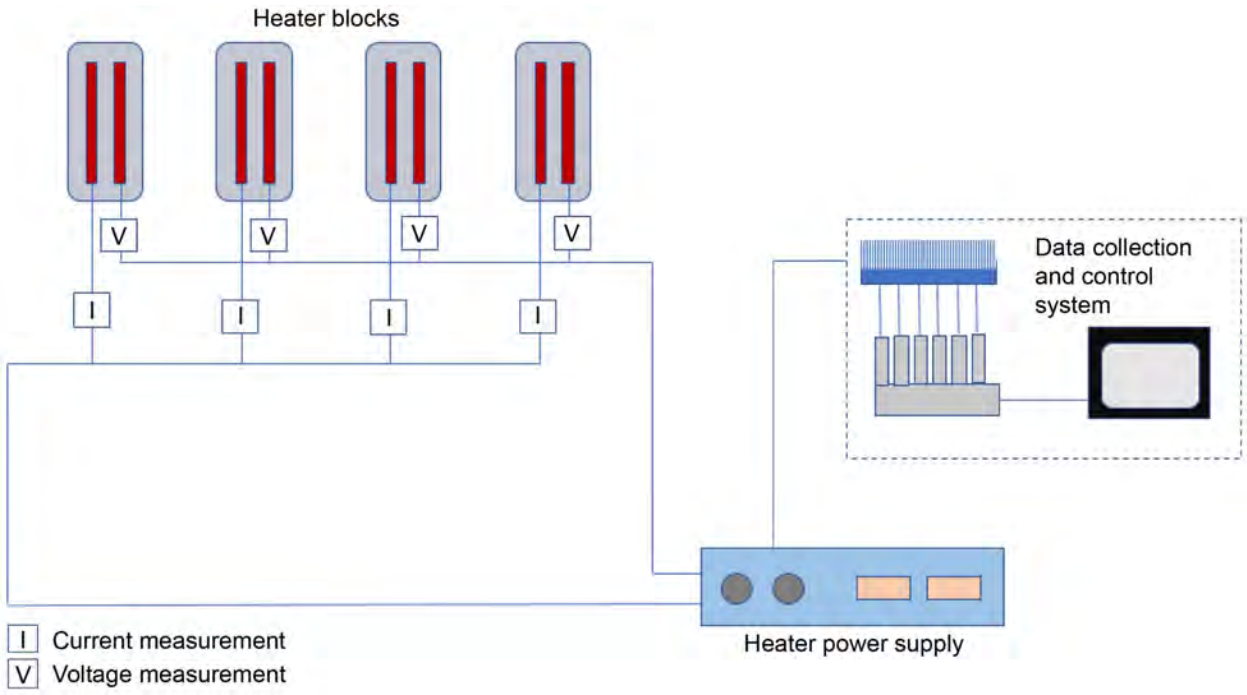

Figure 25.—Heater block power measurement layout.

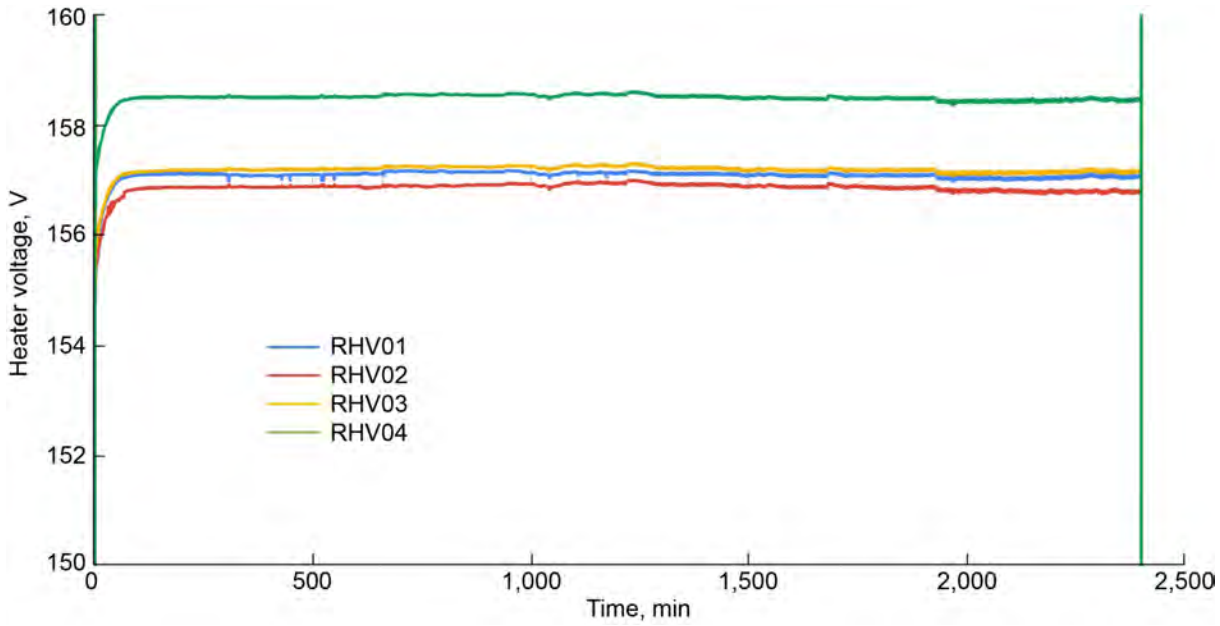

Figure 26.—Heater block voltage.

3.4 Plasma Power

The plasma is initiated with a high-voltage power supply, XP Power Glassman 20-kV, 400-mAdc power supply, model PS/SH020P400, and custom switch box. The power supply provides an electrical potential across the interior of the chamber, between the electrodes, sufficient to ionize the gas and generate the plasma. The switch, shown in Figure 27, is used to make and break the connection between the power supply and the chamber. This establishes a pulsed plasma environment within the chamber. The pulse rate and duration are controllable through the switch box.

The input power to the reactor from the high-voltage power supply is determined from current and voltage sensors on both the anode and cathode side of the reactor. The anode measurements use two Pearson Electronics model 110 current probes and two Tektronix® P6015A high-voltage probes. Both current probes and one of the high-voltage probes are directly connected to the anode data collection oscilloscope. The other high-voltage probe is connected to the high-resolution oscilloscope. The sensors are packaged into an electronics box as illustrated in Figure 28.

Voltage and current are also measured at the cathode with the same types of probes used for the anode measurements. For the cathode current measurement, four of the current and one of the high-voltage probes are used. The output of two of the current probes go to the cathode data-collection oscilloscope and the other two go to the high-resolution oscilloscope. The voltage probe is also connected to the cathode data-collection oscilloscope. The cathode probe arrangement is illustrated in Figure 29.

The data from the current and voltage probes are processed by two Tektronix® MDO3024 oscilloscopes, one for the anode data and one for the cathode data, and then transferred to the data collection system. A separate set of data is collected by a Keysight Technologies Infiniium S-Series MSO804A high-resolution oscilloscope and transferred to the data system. The high-resolution data is collected periodically during the test to examine the plasma power at a resolution not achievable with the continuous data oscilloscopes. The high-voltage switch and power supply are also monitored and controlled by the data and control system. An illustration of the arrangement for collecting the plasma power is given in Figure 30.

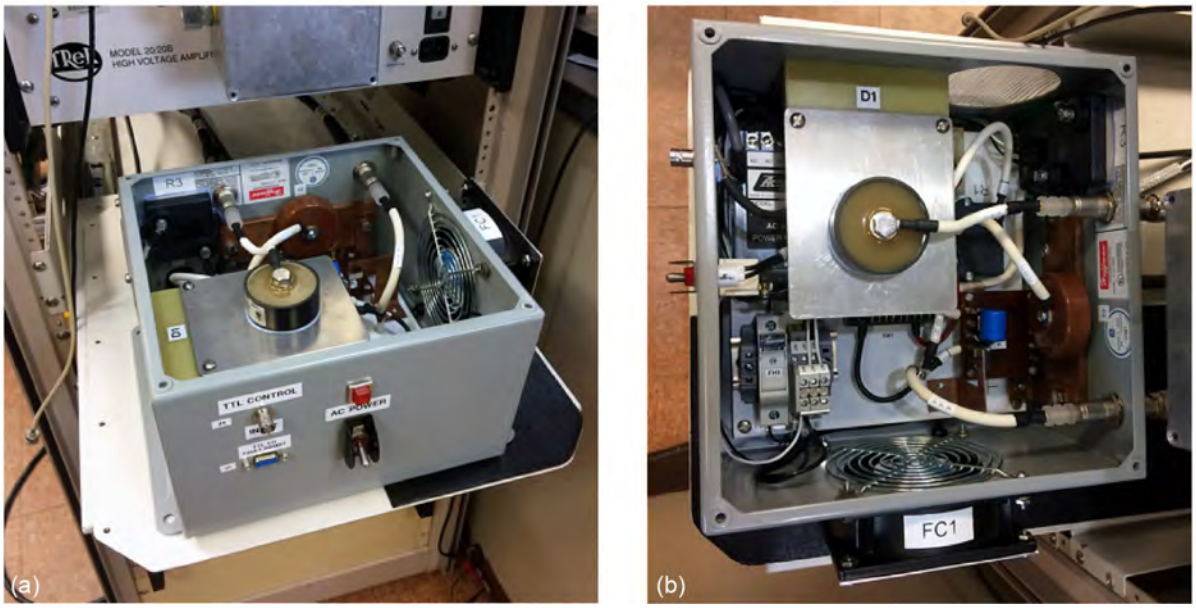

Figure 27.—Plasma power switch. (a) Side view. (b) Top view.

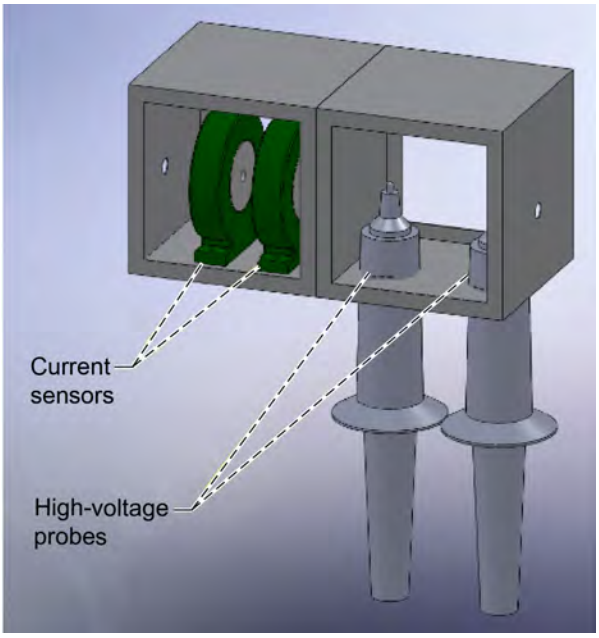

Figure 28.—Anode voltage and current probe arrangement.

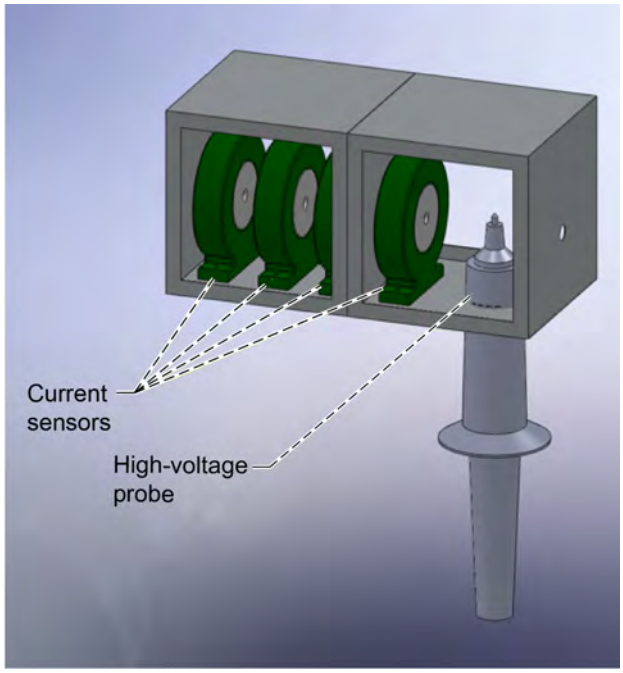

Figure 29.—Cathode voltage and current probe arrangement.

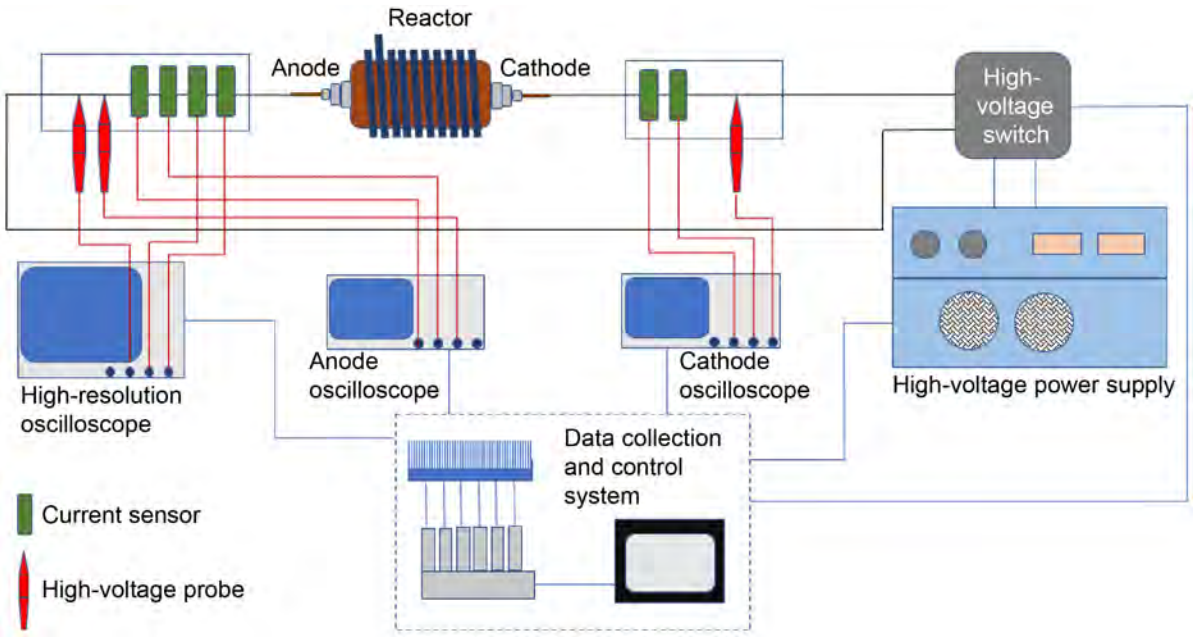

Figure 30.—Plasma power data collection layout.

3.5 Gas Pressure

Pressure measurements are made throughout the system to monitor the chamber pressure as well as to ensure that there are no air leaks into the reactor. Pressure measurements from the chamber and associated gas and vacuum lines are taken at hard vacuum levels up to 200 psi. In addition to monitoring the pressure within the reaction chamber, the vacuum lines are monitored to ensure that sufficient vacuum levels are achieved to provide reliable RGA measurements, and to monitor the test gas collection process.

A number of different types of gauges are used to measure the pressure depending on the desired range. For high-vacuum measurements, the Pfeiffer Vacuum PKR 251 FullRange™ Pirani/Cold Cathode Gauge is utilized from the hard vacuum (10^{-8} torr) to 1 torr range. For pressure measurements in the 10s of torr to above atmospheric, a Setra® 225 diaphragm and strain gauge pressure sensor is utilized. For accurately measuring the pressure in the 10s of torr to single-digit torr range, an MKS Instruments Baratron® Type 122A variable capacitance pressure transducer is used.

To control the pressure within the reactor, an Alicat Scientific PCD pressure controller is used. This controller also provides an output pressure measurement to the data system. The pressure gauge, controller, and different types of sensors are shown in Figure 31 with a diagram showing their layout in Figure 32.

Figure 31.—Pressures sensors, gauge, and controller. (a) Setra® 225 pressure sensor. (b) Alicat Scientific PCD pressure controller. (c) Pfeiffer Vacuum PKR 251 FullRange™ Pirani/Cold Cathode Gauge. (d) MKS Instruments Baratron® Type 122A pressure transducer.

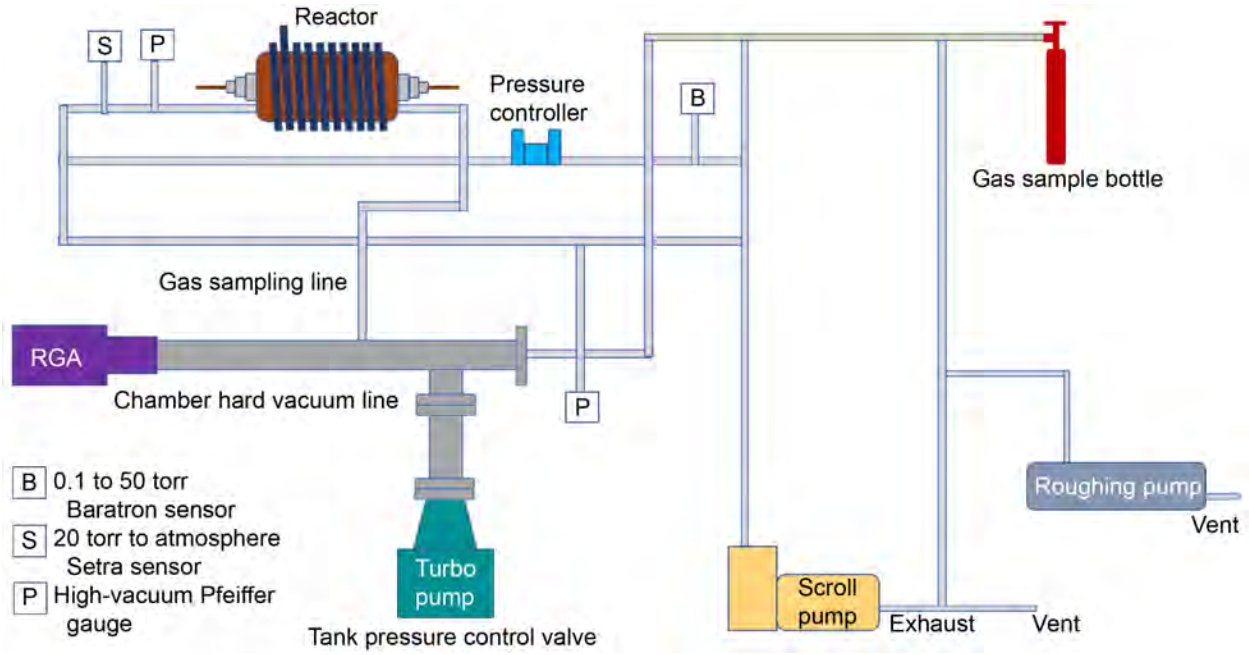

Figure 32.—Pressure sensors, gauge, and controller layout. Residual gas analyzer (RGA).

4.0 Calculation of Heat Output

The net heat or power (P) out of the reactor is calculated from the difference of the calorimeter output power (P_c) and the sum of all of the input power sources, plasma power (P_p) and heater power (P_h). This is given in Equation (1)

$$P = P_c - P_p - P_h \tag{1}$$

The accurate calculation of each of these powers is critical in determining the net output power of the reactor system. The calculation of these powers is accomplished through the use of various types of sensors, such as flowmeters and RTDs for the calorimeter power, and current and voltage probes for the plasma and heater powers. All of these measurements have errors associated with them that must be considered when determining the maximum resolution that can be achieved in the net power measurements. The process of a pulsed plasma generation is very dynamic, and the power input to the plasma fluctuates considerably during the pulses as well as throughout the operational test period. Because of this, accurate input power measurements are challenging and understanding the limitations on the power measurements is critical to providing an accurate net power measurement.

4.1 Calorimeter Output Calculation

The reactor system is designed so that almost all of the heat inputted into the reactor is removed through the calorimeter. To accomplish this a cooling jacket surrounds the reactor. Coolant flows through this jacket and its temperature rises as it acquires heat. The coolant then flows to a chiller where the added heat is removed, its temperature is reduced back to the initial input temperature, and then it is recirculated back through the calorimeter.

To determine the heat absorbed by the coolant water, the mass flow rate through the cooling jacket $\dot{m}$, the inlet T_i and exit T_o temperatures, and the cooling fluid properties must be determined. The power output of the calorimeter is given by Equation (2), where c_p is the specific heat of the cooling fluid.

$$P_c = \dot{m} c_p (T_o - T_i) \tag{2}$$

The uncertainty of the calorimeter output power can be determined by the Taylor series error propagation method given by Equation (3).

$$\Delta P_c = \left[\left(\frac{\partial P_c}{\partial c_p} \Delta c_p \right)^2 + \left(\frac{\partial P_c}{\partial \dot{m}} \Delta \dot{m} \right)^2 + \left(\frac{\partial P_c}{\partial dT} \Delta dT \right)^2 \right]^{1/2} \tag{3}$$

$$\dot{m} = \rho_w v \tag{4}$$

where, $\partial P_c / \partial c_p = \dot{m} dT$, $\partial P_c / \partial \dot{m} = c_p dT$, and $\partial P_c / \partial dT = c_p \dot{m}$ are the sensitivity coefficients, ρ_w is the density of water in g/cm^3, and v is volumetric flow rate in cm^3/s.

The uncertainty coefficients are derived from physical properties of water and the instrumentation specifications. Separate platinum resistance thermometers (PRTs) measure each the inlet and exit water temperatures. Two PRTs are located at the water inlet of the calorimeter, and two PRTs are located at the water outlet of the calorimeter. An average of the two PRTs on the inlet and the exit are used to determine the water temperature. Averaging the two measurements at each location reduces the overall temperature measurement error.

The temperature difference between the exit and inlet average temperature will then be calculated and used in the calorimeter output power calculation. Statistically, averaging the two PRT measurements for the inlet and the two PRT exit temperature measurements and calculating the temperature difference (*dT*) results in a temperature difference uncertainty equivalent to the uncertainty of a single temperature measurement. Note that this assumes the uncertainty of each PRT measurement to be the same.

Class 1/10 DIN PRTs are utilized with National Instruments™ NI–9217 signal conditioning modules. The NI–9217 module provides four, 4-wire 100 Ω PRT and 24-bit measurement channels with 1 mA per channel excitation current. The maximum accuracy is obtained at an acquisition rate of 3.3 Hz. Table 2 lists the uncertainties of the temperature sensors and measurements.

The inlet and exit temperature measurement uncertainty was calculated as ±0.36 °C at a 70 °C operating temperature. The uncertainty of the *dT* measurement was calculated as ±0.25 °C. Note that this should be the worst case since unknown but identical bias errors of the measurement circuits are eliminated by the subtraction process. Therefore, the actual error measurement in the differential temperature will be less than ±0.25 °C.

A high-accuracy alternative to measuring the output of the PRTs is a Tektronix® Keithley Model 2010 7-1/2-digit multimeter. This meter can take voltage or resistance measurements of the PRT resistance and the temperature calculated from the Class 1/10 B generalized curve. The accuracy of the measurement is ± (0.03 + 0.0005T) °C. Thermistor probes specifically calibrated over the 20 to 100 °C temperature range are available with conformal curve fit accuracies of 0.01 °C. The use of the thermistor probes with the Keithley 2010 or with a National Instruments™ PXI–4351 (±0.03 °C) can reduce the measurement error to <±0.05 °C.

The change in ρ_w as a function of temperature over the temperature range of 20 to 100 °C is shown in Figure 33. The second-order polynomial curve fit describes this relationship as indicated on the figure and given in Equation (5), where T_w is the water temperature. The characterization equation was differentiated to provide the sensitivity curve of density to temperature change, given by Equation (6).

$$\rho = 1002.2 - 0.123325T_w - 0.0031937T_w^2 \tag{5}$$

$$\Delta\rho = (-0.123325 - 0.006387T_w)\Delta T_w \tag{6}$$

TABLE 2.–PLATINUM RESISTANCE THERMOMETER (PRT) MEASUREMENT UNCERTAINTY

Temperature, °C	PRT class 1/10 B calibration random error, ±°C	NI–9217[a] temperature error, ±°C	RSS[b] temperature accuracy, ±°C	Temperature difference uncertainty, ±°C
25	0.05	0.15 (typical)	0.16	0.11
70	.05	.35 (max)	.36	.25

[a]National Instruments™.

[b]Root sum square.

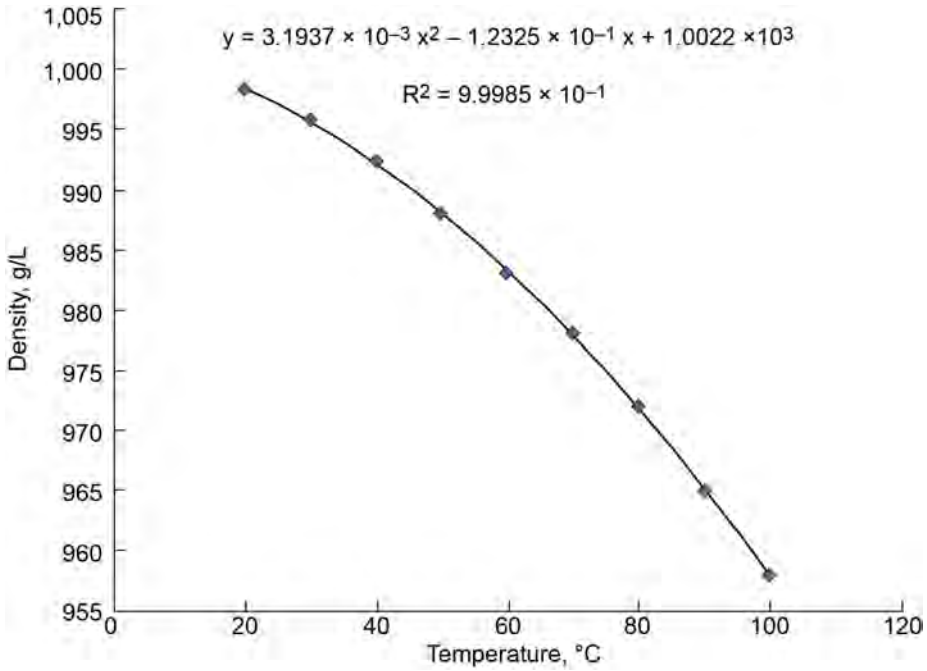

Figure 33.—Water density from 20 to 100 °C. $u\,|\,\text{density}\,| = (-6.387\times10^{3}\text{T} - 0.12325)\,uT$ where T = °C and uT = ±°C.

Table 3 lists the ρ_w as a function of temperature. The ρ_w based on temperature measurement utilizing the second-order characterization curve is listed along with the (g/L) error (calculated and actual) in the calculated density value from the actual table value indicating the curve fit error. The derivative of the second-order characterization equation evaluated at each specific temperature was calculated and is also listed in Table 3. The results approximate the density versus temperature sensitivity coefficient at each specific temperature.

The product of the ρ_w sensitivity coefficient and the temperature measurement uncertainty yields the density measurement uncertainty at that estimated temperature, which corresponds to the ρ_w random error.

The root-sum-square (RSS) result of the curve fit error and the random error is calculated and listed as a function of temperature in Table 3. Based on this analysis, the uncertainty in ρ_w over the 20 to 90 °C range is <±0.74 g/L or ±0.074 percent.

The uncertainty of the water specific heat, c_p, as a function of temperature was estimated from the listed properties of water as a function of temperature. The characteristic curve and sensitivity equations were determined.

The c_p at 20 °C is 4.1813 J/g. This, however, does change slightly with temperature. The change in c_p as a function of temperature over the temperature range of 5 to 100 °C is shown in Figure 34. The fourth-order polynomial curve fit describes this relationship as indicated on the figure and given in Equation (7). The characterization equation was differentiated to provide the sensitivity curve of specific heat to temperature change, given by Equation (8).

$$c_p = 4.215 - 2.6772\times10^{-3}T_w + 6.5894\times10^{-5}T_w^2 - 6.4397\times10^{-7}T_w^3 + 2.5717\times10^{-9}T_w^4 \tag{7}$$

$$\Delta c_p = \left(1.029\times10^{-8}T_w^3 - 1.932\times10^{-6}T_w^2 + 1.318\times10^{-4}T_w - 2.6772\times10^{-3}\right)\Delta T_w \tag{8}$$

TABLE 3.—WATER DENSITY CALCULATION ERROR

Density, g/L	Water temperature, °C	Curve fit		Sensitivity, dg/dT	RSS[a] of curve fit and temperature	
		Calculated	Error, g/L		±g/L	Percent read error
1,000.0	5	1,001.50	1.504	–0.155	1.512	0.15
999.8	10	1,000.65	.848	–.187	.868	.09
998.3	20	998.46	.156	–.251	.296	.03
995.7	30	995.63	–.074	–.315	.323	.03
992.3	40	992.16	–.142	–.379	.405	.04
988.0	50	988.05	.050	–.443	.445	.05
983.0	60	983.30	.304	–.506	.590	.06
978.0	70	977.92	–.082	–.570	.576	.06
972.0	80	971.89	–.106	–.634	.643	.07
965.0	90	965.23	.232	–.698	.735	.08
958.0	100	957.93	–.070	–.762	.765	.08

[a]Root sum square.

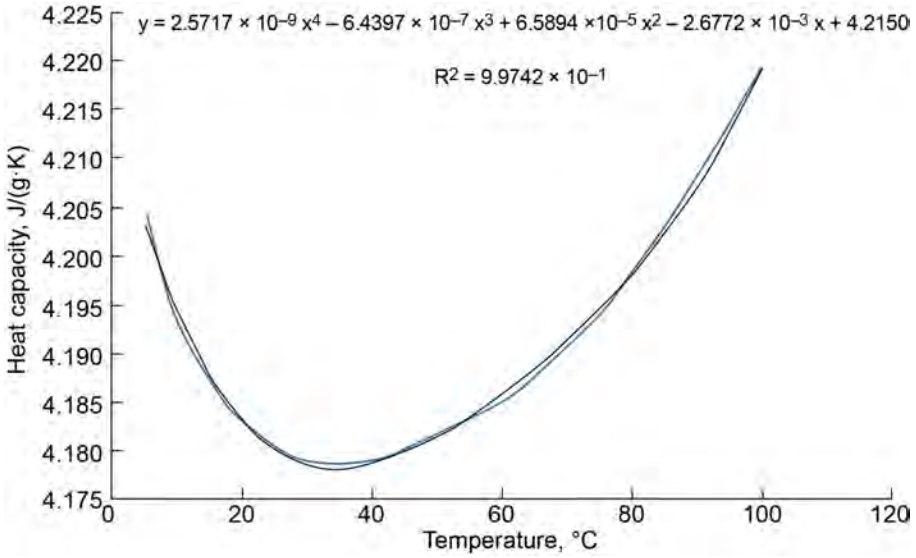

Figure 34.—Water heat capacity as a function of temperature. $uCp = (1.029\times10^{-8}T^3 + 1.932\times10^{-6}T^2 + 1.318\times10^{-4}T - 2.6772\times10^{-3})uT$ where T = °C and uT = ±°C.

Table 4 lists the water heat capacity as a function of temperature at a pressure of 100 kPa. The heat capacity of water, based on temperature utilizing the fourth-order characterization curve, is listed along with the [J/(g·K)] error (calculated and actual) in the calculated c_p value from the actual table value indicating the curve fit error. The derivative of the fourth-order characterization equation evaluated at each specific temperature was calculated and is also listed in Table 4. The result approximates the c_p versus temperature sensitivity coefficient at each specific temperature.

TABLE 4.—WATER SPECIFIC HEAT (c_p) CALCULATION ERROR

c_p, J/(g·K)	Water temperature, °C	Calculated, c_p, J/(g·K)	Error, J/(g·K)	Sensitivity, dc_p/dT	RSS[a] of curve fit	$\pm c_p$ error	Percent read error
4.204	5	4.2032	–0.0008	–0.0021	0.0021	0.002	0.053
4.193	10	4.1942	.0012	–.0015	.0015	.002	.047
4.183	20	4.1831	.0001	–.0007	.0007	.001	.018
4.179	30	4.1787	–.0003	–.0002	.0002	.000	.009
4.179	40	4.1787	–.0003	.0002	.0002	.000	.008
4.182	50	4.1815	–.0005	.0004	.0004	.001	.016
4.185	60	4.1858	.0008	.0005	.0005	.001	.023
4.191	70	4.1913	.0003	.0006	.0006	.001	.017
4.198	80	4.1982	.0002	.0008	.0008	.001	.019
4.208	90	4.2071	–.0009	.0010	.0010	.001	.033
4.219	100	4.2194	.0004	.0015	.0015	.002	.036
4.193	Average	----------	----------	---------	----------	--------	--------

[a]Root sum square.

The uncertainty of the c_p over the water temperature range from 20 to 80 °C varies from 4.178 to 4.198 J/(g·K). A nominal value of 4.188 is used in the power calculations, which bounds the uncertainty within <±0.01 J/(g·K).

The uncertainty of the $\dot{m}$ is a function of the uncertainties of volumetric flow rate and ρ_w over the temperature range of operation and is calculated from Equation (9) where V is the cooling fluid volumetric flow rate in cm^3/s.

$$\Delta\dot{m} = \left[\left(\frac{\partial \dot{m}}{\partial \rho_w} \Delta\rho_w \right)^2 + \left(\frac{\partial \dot{m}}{\partial V} \Delta V \right)^2 \right]^{1/2} \tag{9}$$

The uncertainty in ρ_w over the 20 to 90 °C range was estimated at <±0.00074 (g/cm^3). The RSS uncertainty of the turbine volumetric flow rate based on the manufacturers specification of flowmeter inaccuracy of ±0.25 percent reading and signal conditioner inaccuracy of ±0.1 percent of range is $\Delta V = \pm[(0.0025V)^2 + (0.033\ cm^3/s)^2]^{0.5}$.

The flow rate is measured using a FTI Flow Technologies™ Model FTO–4AIYWBLHCT5 turbine flowmeter used with an LAT–3–CO–V2B6 temperature compensated link transmitter. This flowmeter has a tangential rotor design with sapphire bearing that permit low flow measurements. Also, radiofrequency (RF) pickup eliminates magnetic drag of the rotor.

The sensitivity of the turbine meter is known as the K factor. The K factor equals (ppm/(gal/min)) = turbine cycles per second (Hz) × 60 / (gal/min). The turbine meter K factor is a function calibrated over a range of viscosity and temperature. The volumetric flow rate (gal/min = F × turbine meter volumetric flow rate K factor) is a function of turbine rotational rate frequency and kinematic viscosity v. The v is a function of dynamic viscosity μ and density ρ.

Figure 35 shows v as a function of temperature over the temperature range of 5 to 100 °C. The third-order polynomial curve fit describes this relationship as indicated on the figure and given in Equation (10). The characterization equation was differentiated to provide the sensitivity curve of v to temperature change, given by Equation (11).

$$v = 1.7026 - 4.3123\times10^{-2}T_w + 5.05\times10^{-4}T_w^2 - 2.1617\times10^{-6}T_w^3 \quad (10)$$

$$\Delta v = \left(-6.485\times10^{-6}T_w^2 + 1.01\times10^{-3}T_w - 0.0431\right)\Delta T_w \quad (11)$$

Table 5 lists the cooling water kinematic viscosity as a function of temperature. The kinematic viscosity of water, based on temperature, is listed. Also included is the calculated value from the third-order characterization curve along with the error between the calculated and actual value. This difference indicates the curve fit error. The derivative of the characterization equation evaluated at each specific temperature is also listed in Table 5. The result approximates the *v* versus temperature sensitivity coefficient at each specific temperature.

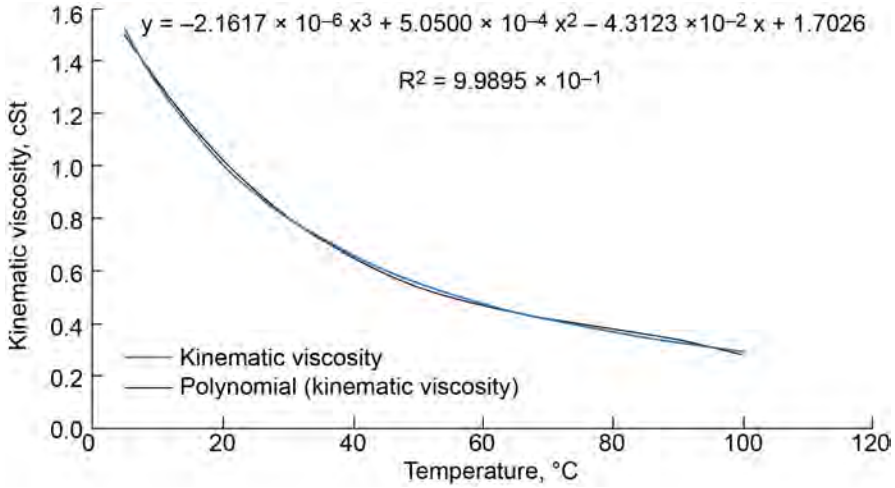

Figure 35.—Kinematic viscosity of water as a function of temperature. $u(cps) = (-6.485\times10^{-6}T^2 + 1.010\times10^{-3}T - 0.0431)uT$ where T = °C and uT = ±°C.

TABLE 5.—KINEMATIC VISCOSITY (*v*) CALCULATION ERROR

v, m^2/s	Temperature, °C	Calculated, *v*	Error	*d*(*v*)/*dT*	RSS[a] of curve fit, ±*v*	Percent *v* error
1.519	5	1.499	–0.020	–0.038	0.043	2.83
1.307	10	1.320	.013	–.034	.036	2.75
1.004	20	1.025	.021	–.025	.033	3.28
0.801	30	.805	.004	–.019	.019	2.38
0.658	40	.647	–.011	–.013	.017	2.56
0.553	50	.539	–.014	–.009	.017	3.03
0.475	60	.466	–.009	–.006	.010	2.21
0.413	70	.417	.004	–.004	.006	1.40
0.365	80	.378	.013	–.004	.014	3.70
0.326	90	.336	.010	–.005	.011	3.43
0.290	100	.279	–.011	–.007	.013	4.60

[a]Root sum square.

TABLE 6.—FLOWMETER OUTPUT ERROR

Flow rate, L/min	Calibration error 0.05% read L/min bias	Repeatability 0.1% read L/min random	Nonlinearity 0.1% read L/min random	Linear link 0.1% range L/min random	RSS[a] error, ±L/min
0.075	0.0000375	0.000075	0.000075	0.002	0.002003162
0.250	.0001250	.000250	.000250	.002	.002034853
0.50	.0002500	.000500	.000500	.002	.002136001
0.750	.0003750	.000750	.000750	.002	.002294695
1.000	.0005000	.001000	.001000	.002	.002500000
1.250	.0006250	.001250	.001250	.002	.002741464
1.500	.0007500	.001500	.001500	.002	.003010399
1.750	.0008750	.001750	.001750	.002	.003300095

[a]Root sum square.

The flowmeter output is based on a 10-point calibration within the range of 0 to 2 L/min volume flow rate. The error associated with the flowmeter output over the full operating range of the flowmeter is given in Table 6.

Solving Equation (9) with the measurement error of 0.00074 g/cm^3 in density and a measurement error of 0.09 cm^3/s in the volumetric flow rate, which is based on the full range of 33.33 cm^3/s, yields a mass flow error of <±0.09 g/s.

From the uncertainties given for the c_p, $\dot{m}$, and ΔT measurement, an estimate of the overall uncertainty in the calorimeter output power measurement can be made from Equation (3) for the measured conditions of c_p = 4.167, $\dot{m}$ = 9.83 g/s, and $T_o - T_i$ = 20 °C.

Using these conditions and their uncertainties in each of the measurements of Δc_p = 0.01, $\Delta\dot{m}$ = 0.09, and ΔT_w = 0.25, yields a total calorimeter power measurement uncertainty of ±1.57 percent. This translates into a power measurement error of ±12.56 W for a total measured power of 800 W.

4.2 Heater Power Input

A Sorensen DLM 300-10E 300Vdc, 10 A, 3 kW power supply is utilized to supply electrical power to the arc reactor heaters. The uncertainty in the power calculated using the power supply voltage and current output gauges was estimated based on manufacturer reported accuracies. The Sorensen voltage and current measurement accuracy was listed at 1 percent of full scale. The full-scale voltage is 300 Vdc and current is 10 A. The inaccuracies are ±1.6 Vdc and ±0.09 A. The error in power is given by Equation (12). Using this equation provides an error in the heater measurement of ±31.4 W.

$$\Delta P = \left[(I\,\Delta V)^2 + (V\,\Delta I)^2 \right]^{0.5} \tag{12}$$

To improve the power measurement uncertainty realized by measuring the power supply voltage and current, DC and voltage measurements were taken using the National Instruments™ NI–9225 for voltage measurement and their NI–9227 for current measurement. The power measurement uncertainty was calculated based on the manufacturer supplied measurement uncertainties of the modules. The analysis results are derived over the expected current range based on the operation of the Watlow® cartridge heaters. A total of eight cartridge heaters are utilized in the reactor. They are each rated at 240 Vdc with a maximum power of 250 W. This represents a maximum current of 1.0432 A and a resistance of 230.3 Ω per heater cartridge. The heaters are configured in four blocks with two heaters in each block. The heaters

in each block are connected in series and the blocks are connected in parallel to the power supply. This produces an effective resistance of the heater network of 115 Ω.

The NI–9225 module is used for voltage measurement and has an accuracy of ±0.05 percent of the reading plus 0.008 percent of the range. The range for this module is 425 Vdc. The NI–9227 module is used for current measurement and has an accuracy of ±0.1 percent of the reading plus 0.05 percent of the range. The range for this module is 3.5 A. These accuracy values are quoted by the manufacturer for operation at 25 °C.

The measurement error for the heater power output is summarized in Table 7 for a range of operating voltages and corresponding heater output powers. The use of the NI–9225 and 9227 modules reduce the power uncertainty from over 30 W to under 1.5 W.

Another method for calculating the heater output power is to measure the current and voltage into each of the four heater blocks. This requires an additional three current and voltage measurements. The measurements would use the same NI–9225 and 9227 modules as the single measurement case for voltage and current, respectively. The voltage range stays the same since the four heater blocks are in parallel. The current through each block will be approximately 1/4 the total current therefore limiting the maximum current read by each sensor to 1/4 of the single measurement case. The error results for the four-heater block measurement case are shown in Table 8.

TABLE 7.—HEATER POWER MEASUREMENT ERROR

Voltage, V	Voltage error, ±V	Current, A	Current error, ±A	Total heater power, W	Power measurement error, ±W	Percent reading
10	0.034	0.087	0.002	0.870	0.018	2.04
50	.042	.435	.002	21.740	.092	.42
100	.060	.870	.002	86.960	.202	.23
150	.082	1.300	.002	195.700	.345	.18
200	.106	1.740	.002	347.800	.527	.15
250	.130	2.170	.003	543.500	.752	.14
300	.154	2.610	.003	782.600	1.024	.13

TABLE 8.—HEATER POWER ERROR FOR FOUR BLOCK MEASUREMENT

Voltage, V	Voltage error, ±V	Current, A	Current error, ±A	Block heater power, W	Block power error, ±W	Percent reading	Total power error, ±W
10	0.034	0.022	0.002	0.217	0.018	8.06	0.070
50	.042	.109	.002	5.430	.088	1.62	.351
100	.060	.217	.002	21.740	.177	.81	.707
150	.082	.326	.002	48.900	.268	.55	1.070
200	.106	.435	.002	87.000	.364	.42	1.450
250	.130	.543	.002	135.900	.463	.34	1.850
300	.154	.652	.002	195.700	.569	.29	2.280
350	.178	.761	.002	266.300	.682	.26	2.730

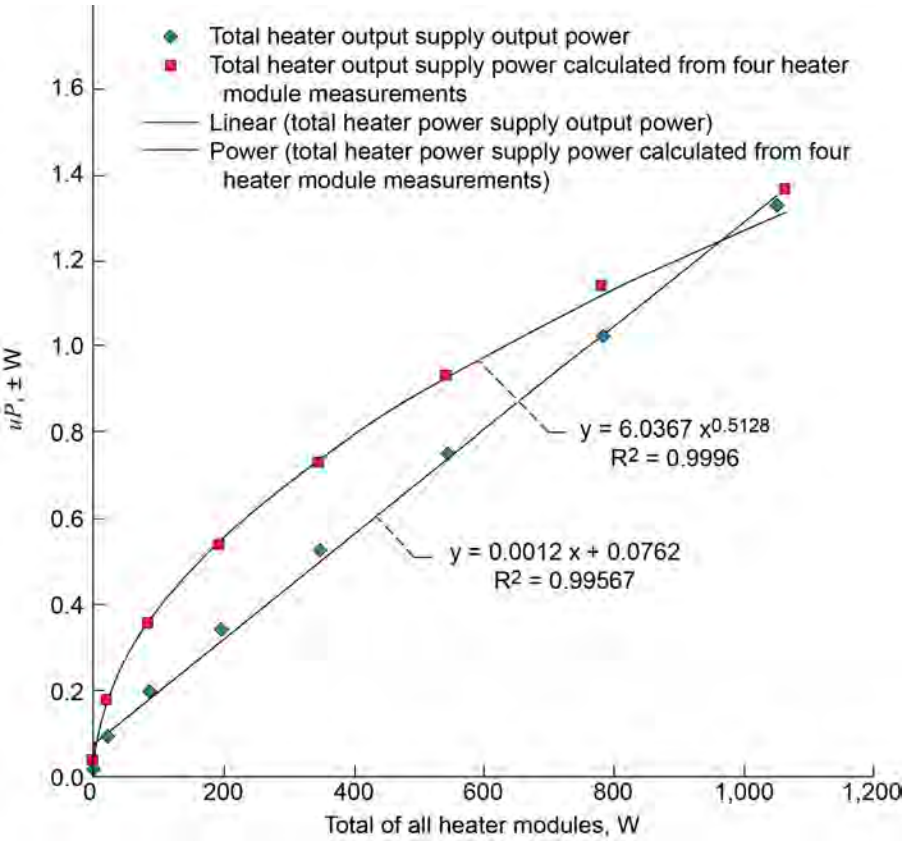

Figure 36.—Heater power supply total power measurement error. Note the uncertainty of power measurement based on power supply is ±15 W.

The output power uncertainty is summarized in Figure 36. This figure shows the difference in output power measurement error between monitoring the total power output from the heater power supply or monitoring the power supply total power into each of the heater blocks.

4.3 Plasma Input Power

To generate the plasma power a high voltage is supplied to the electrodes within the chamber through a power supply. This voltage will cause a breakdown of the gas within the chamber creating a current that flows between the electrodes. This process of ionizing the gas causing breakdown and current flow is repeated with each pulse of the power supply connected to the electrodes. To determine the input power supplied to the reactor to generate the plasma, the input current and voltage across the electrodes is measured. Since the plasma is pulsed, the input current is not constant and varies considerably during each pulse. Accurately measuring this current is a key aspect to determining the power input to the reactor needed to generate the plasma. To accomplish this, current measurement was taken at both the anode and cathode of the reactor. Although technically both of these measurements should be the same in practice, they can differ considerably. This is due to the erratic nature of the plasma formation within the test chamber, which can cause differences in magnitude and frequency of the output current compared to that of the input. Since the current pulses occur at high frequencies, oscilloscopes were used to measure this current at both the anode and cathode of the chamber. Even with the oscilloscopes collecting the current data, only a small fraction of the current pulses were actually captured and averaged to provide input and

output current levels to the data system. This small sampling was then used to provide an average anode and cathode current that in turn was used to calculate the input power.

To evaluate how accurately the current was being calculated a high-precision oscilloscope was used to capture a larger time period of data, on the order of a few seconds, at very high resolution. This data was then analyzed in greater detail to determine the average current for both the anode and cathode that occurred over that time period. This is then compared to the current determined by the test oscilloscopes for that same time period. This process is done to ensure that the test oscilloscopes that are taking current and voltage data continuously throughout the test are accurately representing the input power to the reactor.

4.3.1 Power Comparisons

This section compares power calculations from the National Instruments™ LabVIEW and Tektronix® scope setup (LabVIEW system) with that of the Keysight Technologies 'high-resolution' setup (Keysight) to determine the power used to generate the plasma within the reactor. Test data was taken on 2 days, April 6 and 14, 2017, and used to evaluate the plasma input power to the reactor. The run configuration was the same for both days with the exception of heater power. The first day was run at room temperature, while the second day was with 800 W of heaters. Note, the hotter gas temperature lowers the required breakdown voltage for the plasma. The other relevant run parameters were the pressure (500 torr) and repetition frequency (230 Hz). Plasma current was targeted at 120 mA.

4.3.2 Data Acquisition Summary

The LabVIEW system captures four consecutive pulses approximately once every 2.5 s. Instantaneous power is then calculated from these waveforms, and the power is averaged over the four cycles. Excess data is discarded. These average powers are accumulated in an array over a specified length of time (either 5 or 15 s), at which point they are averaged together and written to the data file. Also written to the data file are the number of data points in the accumulated power array and their standard deviation. Of note, the April 6, 2017 data was accumulated and written to the file every 5 s, while the April 14, 2017 data was averaged over a 15-s period.

Each Keysight data point represents 512 consecutive pulses. This represents 2.2 s of data, and two of these data points were taken consecutively, totaling 1,024 pulses, to investigate extended capabilities. Due to the nature of the capture mechanism of the scope, only 1.5 ms of data is captured each pulse. The other 2.8 ms of inter-pulse data is not captured. This is deemed acceptable since the control pulse is off during this time, hence the high-voltage switch is open and there is no current flowing in the plasma. In other words, the power contribution during this time is zero. Instantaneous power is calculated for each pulse and is essentially zero-padded to the full period length before being averaged to arrive at a per-pulse average power. Each scope capture generates 512 averaged pulse powers.

4.3.3 Anode Versus Cathode Current

Differences in anode and cathode current were observed. There is an initial step in the anode current before the gas breaks down, corresponding to the capacitance of the system charging up. The observed current spike on the cathode is typically higher than the anode current spike. In addition to these differences, observed power from the LabVIEW system is slightly higher when using the anode current for power calculations, on the order of 1 to 2 W. This is not always true for the Keysight system; on April 6, 2017, the cathode power was higher than the anode, while on April 14, 2017, it was lower than the anode power.

The specifics of this were not fully explored, though it is assumed that the Keysight is more accurate. The Keysight has a 10-bit front end and is run using high-resolution mode, enabling data capture at an effective bit depth of 13 bits. The Tektronix® scopes have an 8-bit front end and are not currently run using high-resolution mode, leading to a lower effective bit depth. Since the cathode current peaks at a higher value, the channel gain on the cathode current on both scopes is turned to a lower amount, reducing resolution and sensitivity relative to the anode current measurements. This could contribute to the differences between the two data acquisition systems in regards to the power calculated from the cathode current. The following sections will focus on the anode current and power derived from it.

4.3.4 Average Power Distribution

Since the LabVIEW system only captures four consecutive pulses approximately once every 2 to 3 s, there is a chance that it is not sampling the 500 to 600 pulses in a statistically correct manner. A histogram of individual pulse power calculated from the currents of the anode and cathode is shown in Figure 37. From this figure, it can be seen that the average anode power is consistently higher than the average cathode power. This is likely due to current leakage from the system through the structure as well as through RF losses. The plasma formation can produce significant RF emissions. The power from these emissions is lost from the system and result in a lower cathode power reading. This data illustrates the distribution of power from a single high-resolution capture of the Keysight scope.

To further simulate the LabVIEW system's acquisition method, the pulse power calculated from the Keysight data was processed with a rolling mean of four pulses, shown in Figure 38. Nominally, one of these data points (out of 512) is representative of what the LabVIEW system captures and records as the power. The distribution of these potential data points has a smaller spread than that of the histogram, as the process of recording and averaging four sequential pulses reduces the uncertainty.

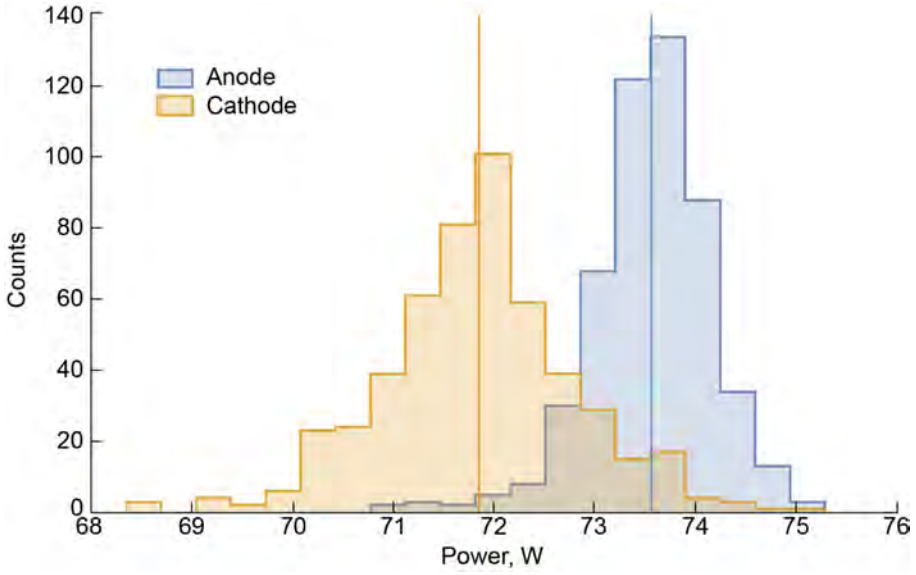

Figure 37.—Power from anode and cathode on April 14, 2017. Mean power from 512 pulses. Anode = 73.6 W. Cathode = 71.9 W.

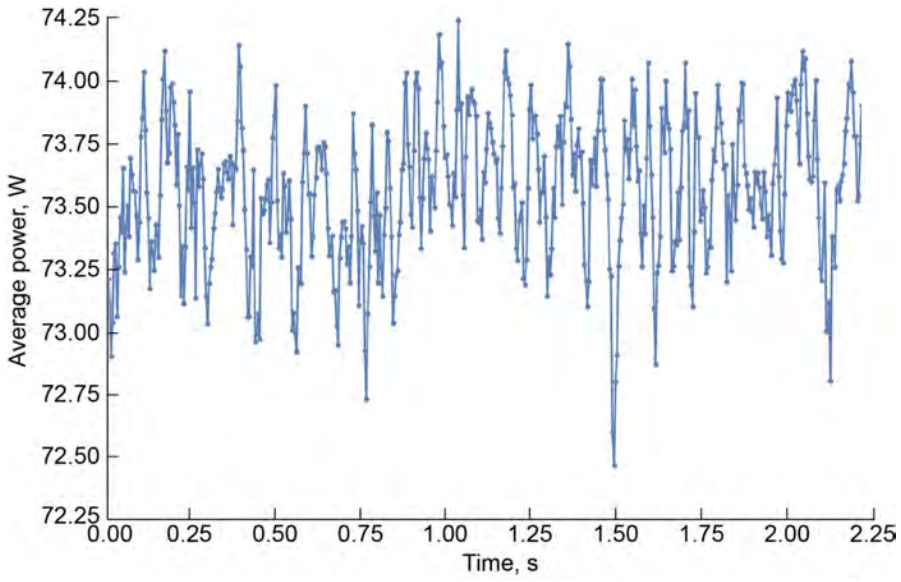

Figure 38.—Rolling mean of anode power of four sequential pulses from April 14, 2017.

4.3.5 Comparison Between Systems

Synchronization of the clocks between the Keysight and the LabVIEW system is necessary to compare the results obtained from the two systems. During the two days of testing referenced here, the LabVIEW system time was off by 9 to 10 min. An attempt to adjust for this discrepancy has been made; however, data from the two sources may still be out-of-sync by 1 or 2 min.

In Figure 39 and Figure 40, the LabVIEW system's anode power data is represented by the dark blue trace. The light blue bands around this trace represent two standard deviations of spread in either direction. The standard deviation is calculated in LabVIEW from the *N* power numbers accumulated every 5 to 15 s.

The red data points are the median power calculated from the rolling four-pulse mean of the 512 pulse high-resolution data captures. The error bars in Figure 40 illustrate the range of the minimum and maximum power observed in the rolling four-pulse mean (shown in Figure 38). The median power of the rolling four-pulse mean was chosen because it is more representative of the most likely four-pulse mean sampled by the LabVIEW system.

The LabVIEW system has consistently higher power averages than the Keysight. More data would help verify this consistency. One possible explanation is the lower bit depth of the Tektronix® scopes in the LabVIEW system could be exaggerating low-level signals. This has the potential to magnify low-level signals during the 'off' times of the discharge. If low-level current and voltage measurements during the off portion of the cycle (75 to 90 percent of the time) are registering as small positive values, it could be quite easy to get a bias of a 0.5 to 1 W in the averaged instantaneous power calculations. Not only does Keysight have better resolution for small signals, but the power calculation used for its data forces the power to be zero during a large portion of the off time. If this is the cause of the discrepancy between the two systems, it could potentially be addressed in the LabVIEW system by using the high-resolution acquisition mode on the Tektronix® scopes, and/or setting the instantaneous power to zero during the off times of the cycle before averaging it.

As can be seen from the April 14, 2017 data (and from the data in Figure 38), there is a real spread in average power calculated from four pulses. The spread is approximately ± 1 W. The April 6, 2017 data shows a larger spread, at times approaching ± 3 W. The reactor chamber was heated on April 14, 2017 and not on April 6, 2017, leading to a higher breakdown voltage on April 6, 2017. The higher

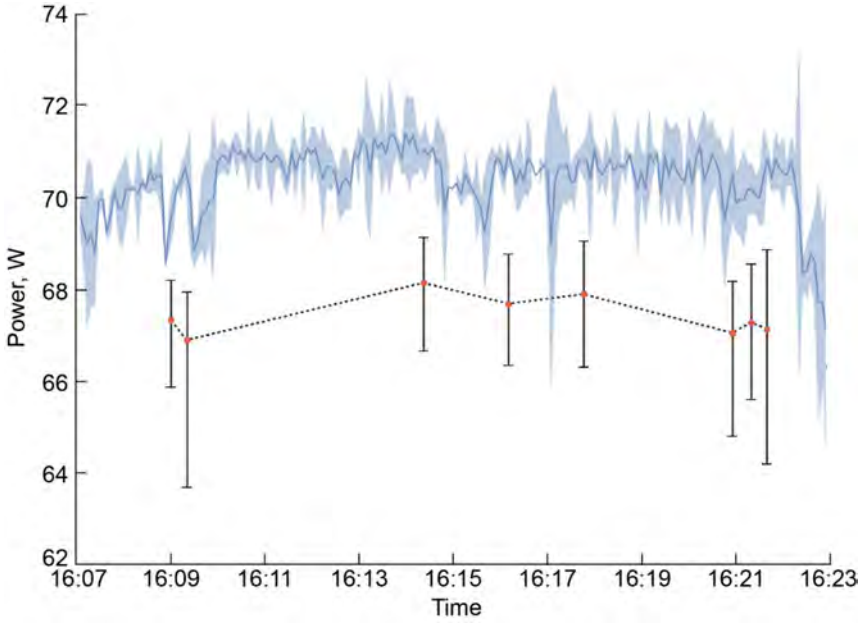

Figure 39.—April 6, 2017 anode power data. LabVIEW anode power data is represented by the dark blue trace. The light blue bands represent ± 2σ. Red data points are the median power calculated from the rolling four-pulse mean of the 512 pulse high-resolution data captures. The error bars illustrate the range of the minimum and maximum power observed in the rolling four-pulse mean.

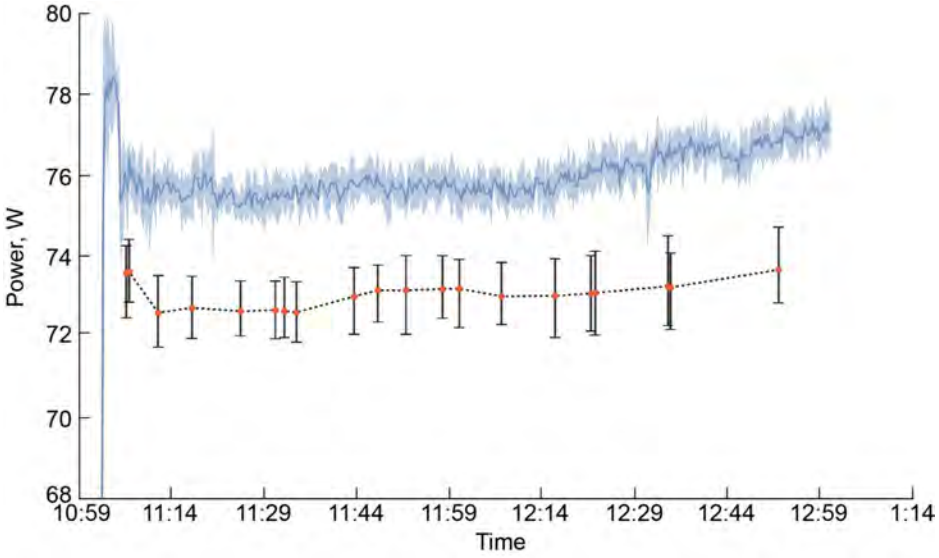

Figure 40.—April 14, 2017 anode power data LabVIEW. Anode power data is represented by the dark blue trace. The light blue bands represent ± 2σ. Red data points are the median power calculated from the rolling four-pulse mean of the 512 pulse high-resolution data captures. The error bars illustrate the range of the minimum and maximum power observed in the rolling four-pulse mean.

temperature is equivalent to an effective halving of operating pressure with respect to gas breakdown. This can be seen in the statistical breakdown lag shown in Figure 41 and Figure 42. The lag is defined in this case as the length of time from the closing of the high-voltage switch ($t = 0$) to the formation of the spark, approximated by the peak in the measured power. This is illustrated in these figures where

“counts” represents the number of pulses from the total amount collected that began breakdown at a specific time increment from when the voltage was applied. The power peaks because of the high voltage right before the instant of breakdown and the ensuing current peak at the time of breakdown.

On April 14, 2017, shown in Figure 41, the distribution of breakdown lag times is roughly Gaussian and has a narrow full width at half maximum (FWHM) of a little over 1 μs. In comparison, the April 6, 2017 data (Figure 42) shows much more variation in the statistical lag time. Not only is the peak of the distribution shifted to a longer lag time, the FWHM is roughly 20 μs, and it exhibits an extended tail and skew towards longer lag times. Since the fixed duration of the control pulse determines the end time of the high-voltage waveform, longer lag times lead to shorter plasma pulses, reducing the time that the system is able to dissipate power. As a result, there is a correlation between these slightly shorter pulses and lower pulse power.

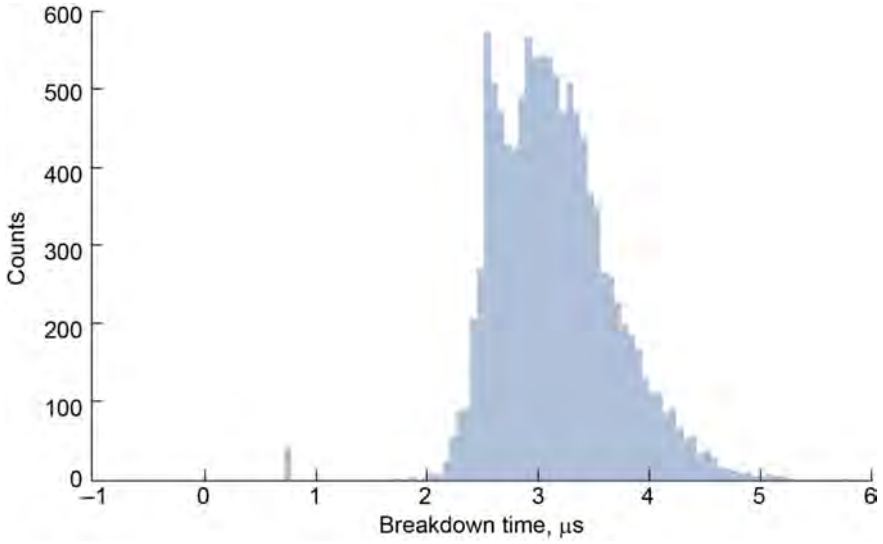

Figure 41.—April 14, 2017 statistical breakdown lag.

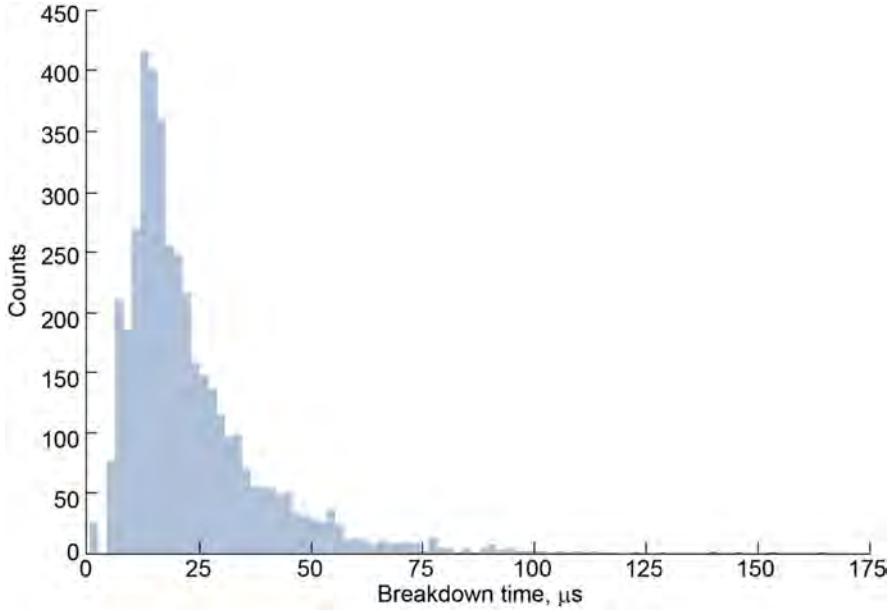

Figure 42.—April 6, 2017 statistical breakdown lag.

Plotting the average pulse power versus the breakdown lag for the recorded pulses on the two days illustrates this correlation between longer breakdown lags and lower powers on April 6, 2017 (Figure 43 and Figure 44). However, in both data sets, there is still variation in the average pulse power that is not correlated to breakdown lag. While there is strong correlation between peak voltage (at the moment of breakdown), peak current (at the spark during breakdown), and peak power (at breakdown) for a pulse, there is little correlation between any of these quantities and average pulse power.

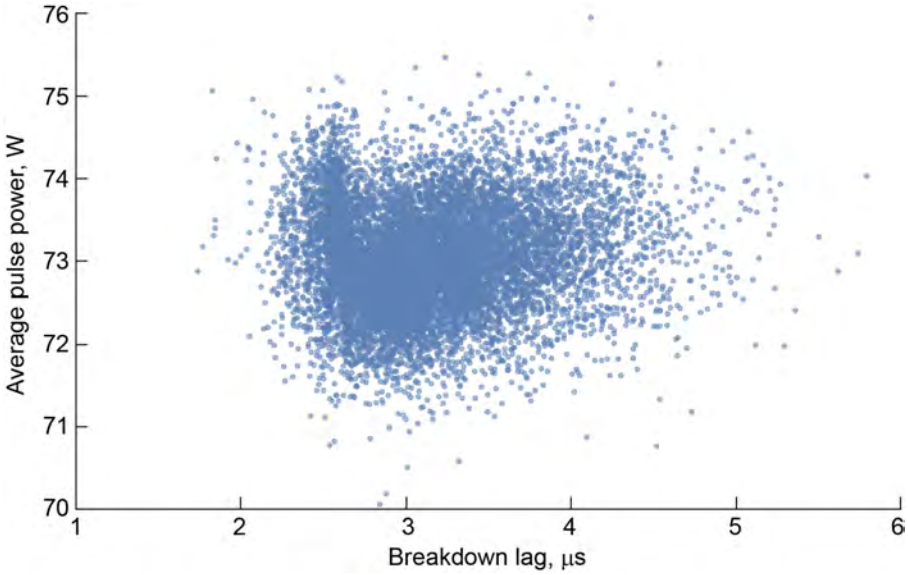

Figure 43.—April 14, 2017 pulse anode power versus statistical breakdown lag.

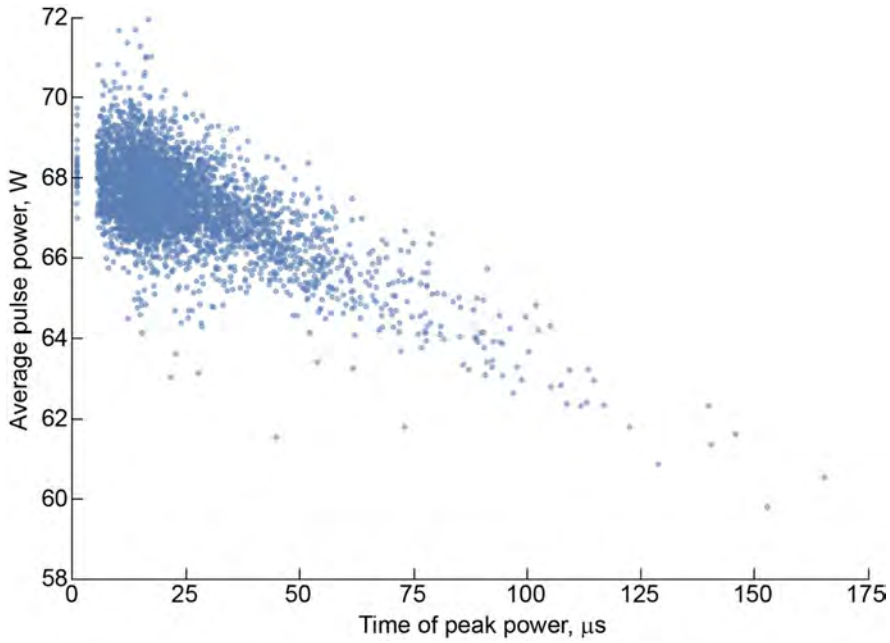

Figure 44.—April 6, 2017 pulse anode power versus statistical breakdown lag.

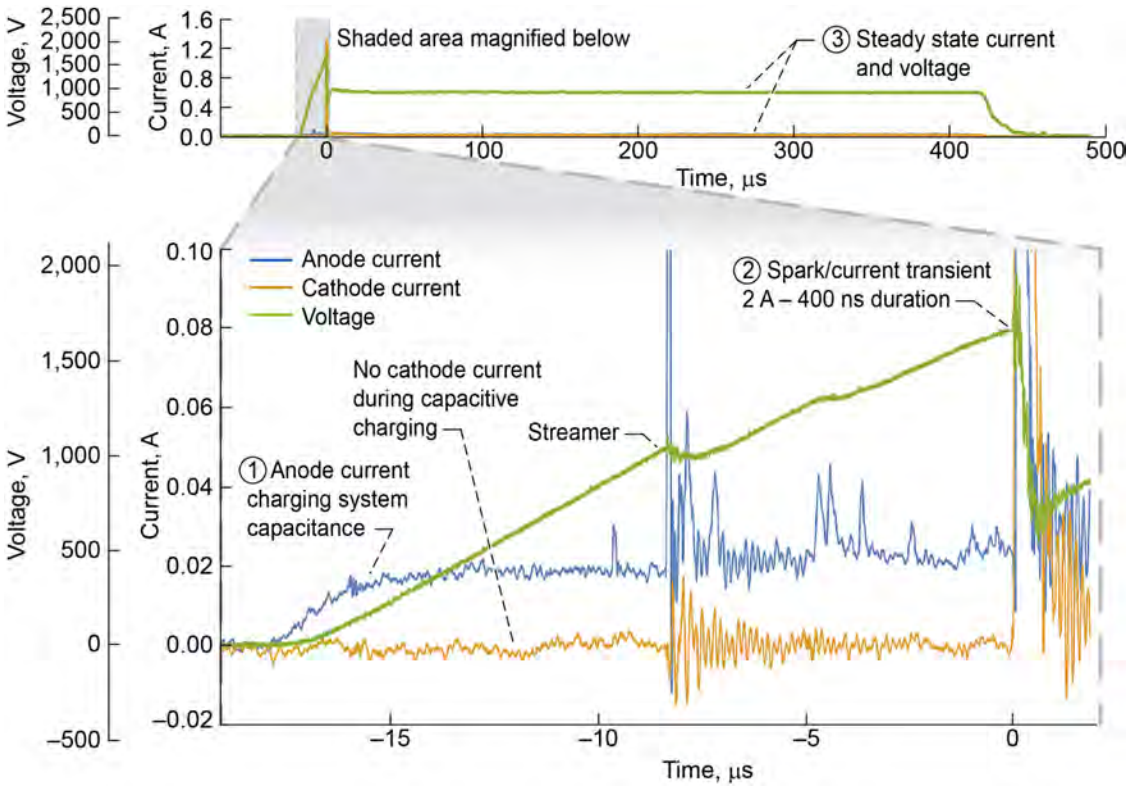

Figure 45.—Trek® Inc. power amplifier breakdown process.

4.3.6 Breakdown Process

The breakdown process has similar characteristics to the process observed while operating with the Trek® Inc. 20/20 amplifier. Salient features are illustrated in Figure 45, which is representative of the general amplifier output during the breakdown process and described as follows.

1. An immediate flow of current on the anode side of the device as soon as the voltage is applied, prior to breakdown. The current stays at the steady level of the amplifier maximum output while the voltage linearly ramps until the system breaks down.
2. At breakdown, a brief spark occurs, evident as a transient in both the anode and cathode current, until
3. The discharge current returns to the level controlled by the power supply, and the voltage reaches the corresponding value determined by the discharge.

The charge stored in the system capacitance prior to the breakdown is equivalent to the charge contained in the current transient. This has been confirmed with analysis of measurements obtained during operation.

Of note, with the new high-voltage switch and DC power supply arrangement, the system ramps voltage much faster than before (2,000 V/µs compared to 75 V/µs). The equivalent process for the new high-voltage system is shown in Figure 42.[1] The system capacitance is estimated to be 30 to 40 pF. Previously, this value ranged anywhere from 30 to 350 pF; in the configuration illustrated in Figure 46, it is estimated to be 230 pF.

[1] Due to the shorter time scales, resonances in the current traces appear more prominent and the number of data points captured during the voltage ramp is reduced. This makes the data look not as clean.

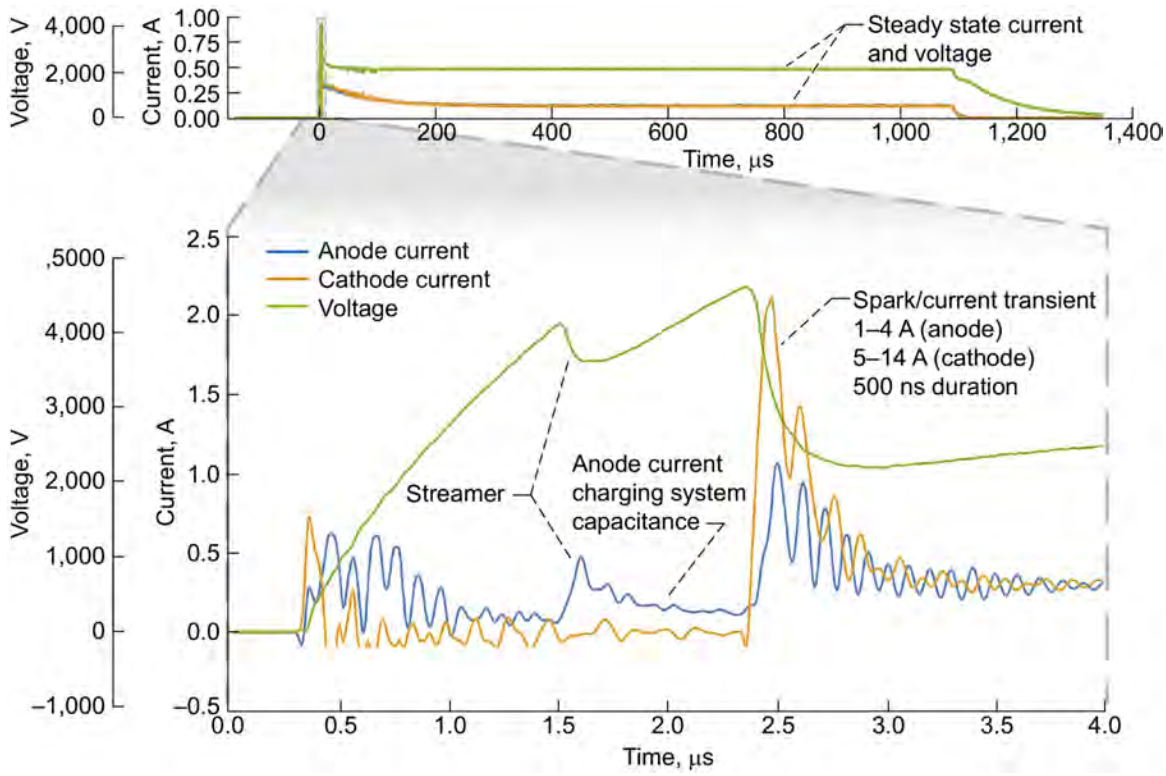

Figure 46.—New high-voltage system breakdown process.

TABLE 9.—INSTANTANEOUS PLASMA POWER MEASUREMENT UNCERTAINTY

Measurement probe or instrument	Measurement error, ± percent	Droop error, percent/ms	RSS[a] error ± percent reading uncertainty
Pearson Model 110 current probes	1.0	0.8	Est: 1.3
Tektronix® MDO3024 oscilloscope	2.4	----	2.4
Current measurement uncertainty: $[(1.3^2) + (2.4^2)]^{1/2} = \pm 2.73$ percent reading			
Tektronix® P6015A HV probe	3.0	----	Est: 3.0
Tektronix® MDO3024 oscilloscope	2.4	----	Est: 2.4
Voltage measurement uncertainty: $[(3.0^2) + (2.4^2)]^{1/2} = \pm 3.84$ percent reading			
Power measurement uncertainty: $[(2.73^2) + (3.84^2)]^{1/2} = \pm 4.7$ percent reading			

[a]Root sum square.

4.3.7 Instantaneous Power Measurement Uncertainty

The overall uncertainty in measuring the instantaneous plasma power is based on the measurement error of the voltage and current probes and the oscilloscope used to collect the data. These measurement uncertainties are given in Table 9 with the overall power measurement uncertainty ±4.7 percent of the power input or ±1.88 W for 40 W plasma input power level.

4.3.8 Final Checkout Run

A final 24-h checkout run was performed, starting on April 25, 2017. Most of the previous information holds true for the data collected during the final checkout run. Of note, the LabVIEW system data still has the positive offset in the anode power compared to the high-resolution Keysight data. The comparison data is displayed in Figure 47.

The high-resolution Keysight data showed relatively good agreement between anode and cathode measurements through the run. The cathode data showed slightly higher spread than the anode data, but the distributions had similar means and medians. This data is shown in Figure 48. As in previous figures, the data points are the medians of the four-pulse rolling average, while the error bars represent the minimum and maximum four-pulse average for each data capture of 512 pulses.

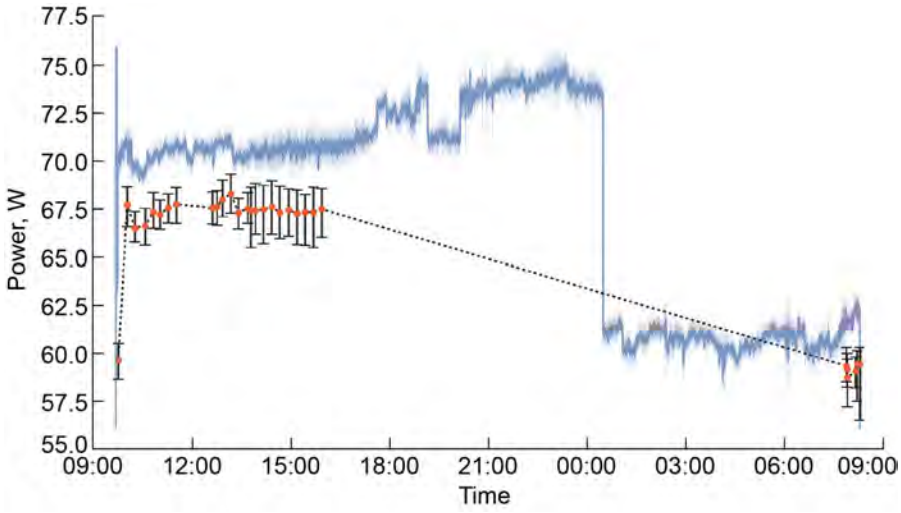

Figure 47.—April 25, 2017 anode power data for the 24-h test run.

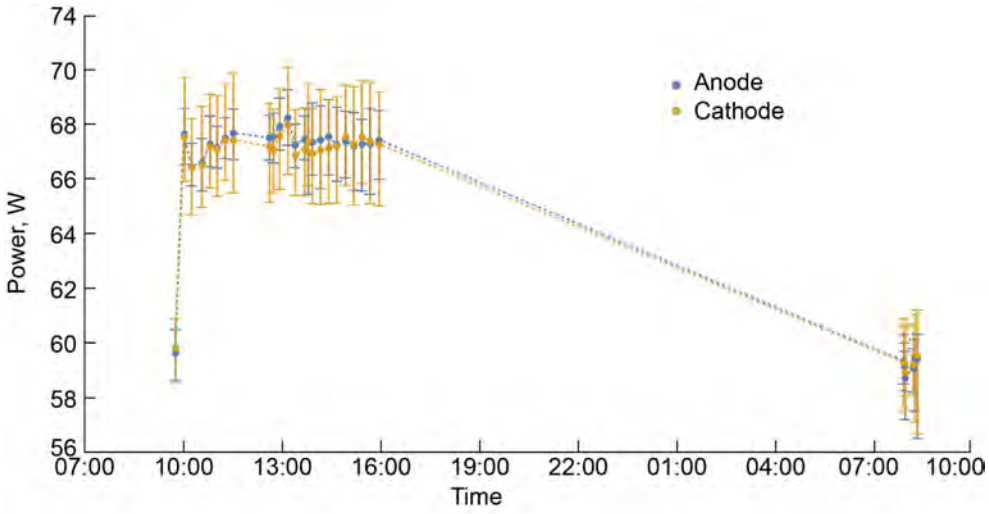

Figure 48.—April 25, 2017 anode and cathode power comparison.

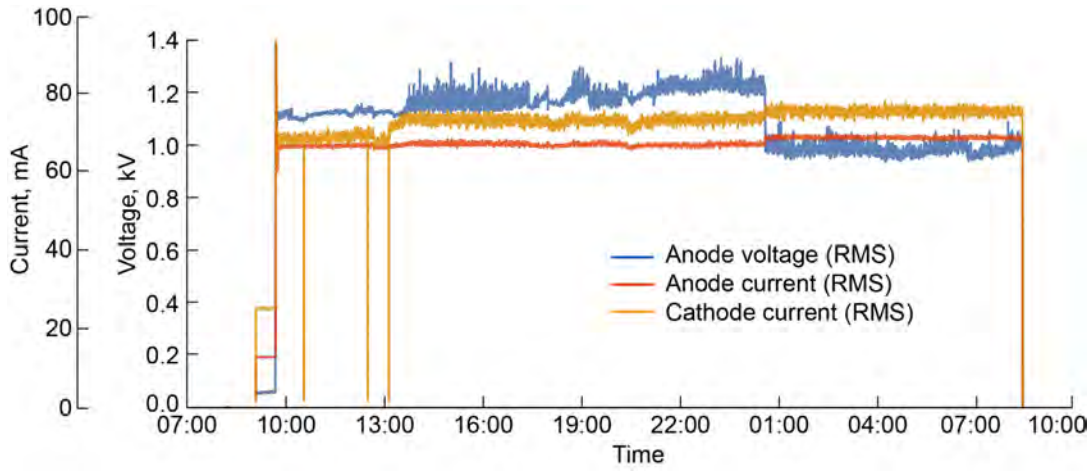

Figure 49.—Current and voltages over 24-h test showing sudden drop in voltage. When cathode current value drops to zero, root-mean-square (RMS) value is not accurate.

Two features to note during the run were the increase in recorded root-mean-square (RMS) voltage around 14:00 on April 25, and the sudden drop in voltage and power at 01:00 on April 26 (see Figure 49).[2] The increase in RMS voltage is due to the discharge entering a phase where breakdown became delayed. A delayed breakdown results in the voltage rising to its peak and holding for 10 to 40 μs. This leads to an increased RMS voltage. Since the breakdown lag distribution widens (representing more variation) as its mean grows larger (like that in Figure 42), the measured RMS voltage at any given point in time has more variance.

The sudden drop in power at 01:00 on April 26 is consistent with operating the discharge in a less "resistive" regime. The main part of the discharge voltage dropped approximately 300 V and the current increased slightly, resulting in a 10 W power drop. Posttest inspection of the disks revealed severe melting of several disks, and lots of activity on the outer diameter of some of the SiO_2 gaps. Similar behavior in the voltage would be expected if discharge needed to form across one fewer SiO_2 gap. This changed operating mode happened in an abrupt fashion.

4.4 Total Output Power Error

The total output power error is the RSS of all of the measurement errors associated with determining the output power of the system. The uncertainty power were found utilizing the following equations and conditions the results for an 820 W system.

[2] The RMS values are representative, but no longer accurate. The voltage decays after the switch opens, governed by the resistance of the bleeder resistor in the switch box. At this point in time, there is real current flowing through the resistor that is not measured by the Pearson Electronics current monitors. While the power dissipated is real, it is not recorded. Neither does it enter the calorimeter. This effect leads to higher RMS voltage values than those that contribute to the power measured by the calorimeter. In addition to this effect, when the breakdown is delayed, the high pre-breakdown voltage can lead to higher RMS voltage values. It is for reasons like these that the measurement system was moved away from RMS values for power calculation. Nonetheless, the RMS values are recorded as they can be useful for diagnostic purposes.

$P_E = P_{Out} - P_{In}$ where P_E is the excess power, P_{Out} is the output power, and P_{In} is the input power.

$P_E = (c_p \cdot \dot{m} \cdot \Delta T) - (P_H + P_A)$ where P_H is the heater input power and P_A is the amplifier input power.

The uncertainty powers are listed as follows for an estimated 820 W power measurement with input power from the plasma power amplifier and heaters and the output power determined by the calorimeter.

- Uncertainty due to excess power baseline variation (μP_{Offset}) over 24 h was estimated as ±8 W = ±0.98% of the total power.p
- Uncertainty due to water calorimeter output power measurement μP_o:

$$\mu P_o = \left[\left(\frac{\pm 0.1 \ \text{g/s}}{\dot{m}} \right)^2 + \left(\frac{\pm 0.07 \ ^\circ\text{C}}{\Delta T} \right)^2 + (0.0024)^2 \right]^{1/2}$$

  - Typical levels at 820 W input power: $\dot{m}$ = 14 g/s; ΔT = 13.6 °C.
  - Results are ±7.5 W = ±0.91% of the total power.
- Uncertainty of 40 W power input from the amplifier μP_A.
  - $\pm \frac{\mu P_A}{P_I}$ where the typical level of P_I is 820 W.
  - The amplifier power (P_a) RMS measurement error due to 4.6 cycle measurements within the 20 ms record length is ±1.9 W = ±0.23% of the total power.
  - Duty cycle variability of 25 ± 3.3% = ±13% pulsed power amplifier error.
- Uncertainty of input power due to heater power supply power measurements μP_H.
  - $\pm \frac{\mu P_H}{P_I}$ where P_I is 780 W.
  - ±1 W = ±0.12% of the total power.
- Total excess power measurement RSS uncertainty.

$$\mu P_E = \left[(\mu P_O)^2 + (\mu P_I)^2 + (\mu P_{\text{Offset}})^2 \right]^{1/2}$$

$$\mu P_I = \left[\left(\pm \frac{\mu P_H}{P_I} \right)^2 + \left(\pm \frac{\mu P_A}{P_I} \right)^2 \right]^{1/2}$$

$$\left[(0.98\%)^2 + (0.91\%)^2 + (0.23\%)^2 + (0.12\%)^2 \right]^{1/2}$$

  - Results are ±1.36% reading. (820 W ± 11.15 W).

A graphical representation of the overall error analysis flow chart for the reactor system is shown in Figure 50.

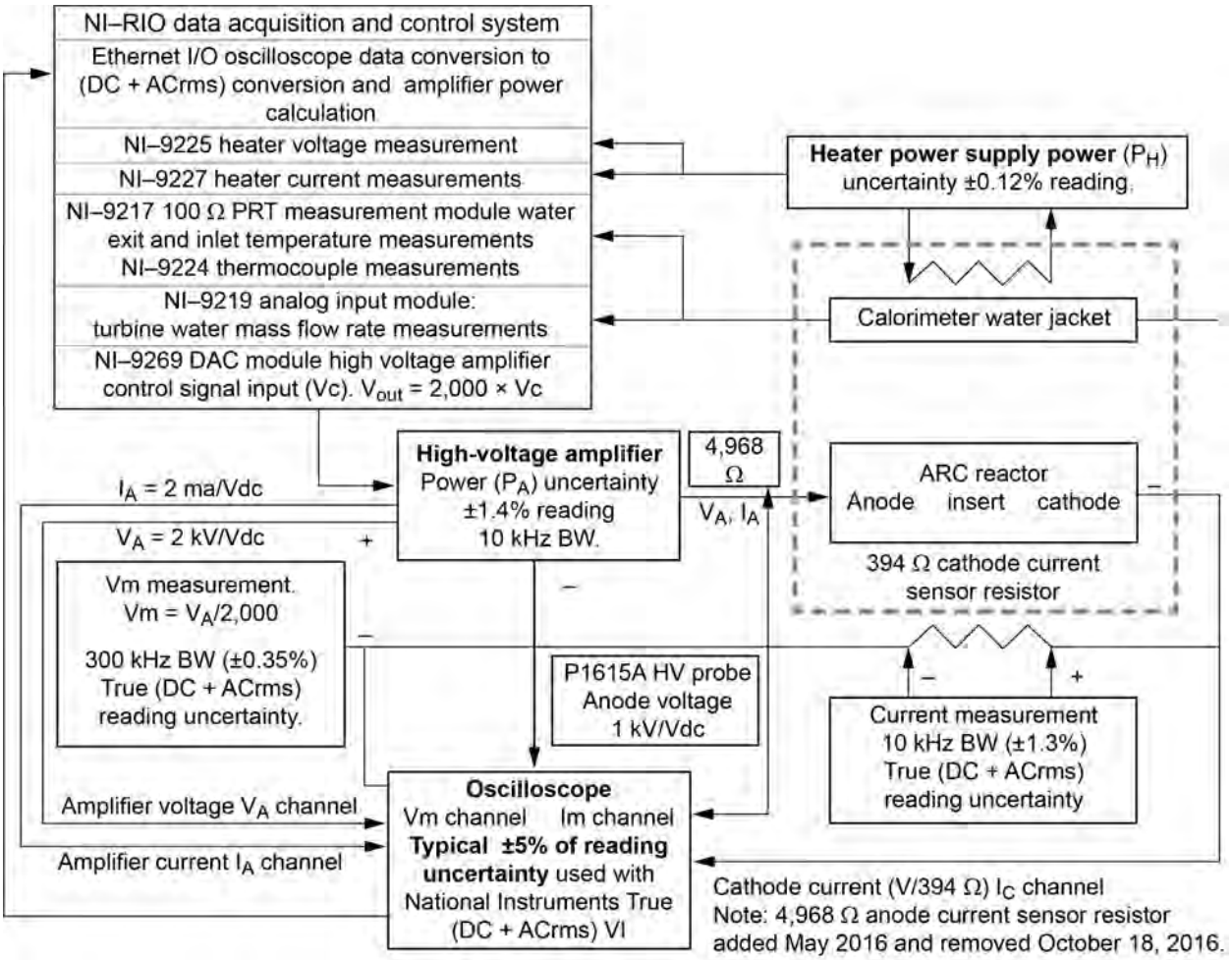

Figure 50.—Error analysis for an 820 W plasma reactor excess power at 10 Hz bandwidth. Radiofrequency (RF). Note: Some tests developed high noise resulting in large oscilloscope input power measurements. This power level is indicated on National Instruments™ (NI) True root mean square (RMS) meter measurements with their lower bandwidths. High-frequency RF component did not increase calorimeter water temperature and is believed to be radiated from power wiring outside reactor. Antenna pickup coupled to spectrum analyzer verify presence of broadband RF field. Band width (BW). Direct current (DC). Alternating current root-mean-square (ACrms). Platinum resistance thermometer (PRT).

5.0 Test Sample Material and Preparation Summary

For this initial testing, the base test sample material originates from a nickel metal foam roll, as shown in Figure 51. The nickel metal foam has the following properties:

- Pore size of 450 μm
- Thickness of 1.6 mm
- Aerial density of 420 g/m^2

The test sample disks are punched from the nickel metal foam to fit within the test sample holder for the reactor. Once cut to size, all of the nickel disks are cleaned following an oxygen cleaning process (Refs. 2 and 3). This process is used to remove all contaminants on the metal and is typically utilized for materials that will be used in an oxygen-rich environment. After cleaning, a test sample was examined

using a scanning electron microscope (SEM) to image the surface and an energy dispersive spectrum (EDS) analysis to determine the material composition.

Baseline images of the nickel metal foam from the SEM analysis are shown in Figure 52. From these images, it can be seen that the foam pore distribution is uniform with no fused or previously molten regions.

To evaluate the composition of the nickel metal foam, a piece of foam was selected at random. Five areas of the sample were examined using secondary electron (SE) and backscattered electron (BSE) imaging and EDS analysis. The EDS will detect chemical difference in the excited volume. The lower detectability limit is about 1,000 ppm. High-resolution images of an area of the material being scanned is given in Figure 53. This image shows considerable detail of the metal surface and its construction.

Figure 51.—Nickel metal foam roll.

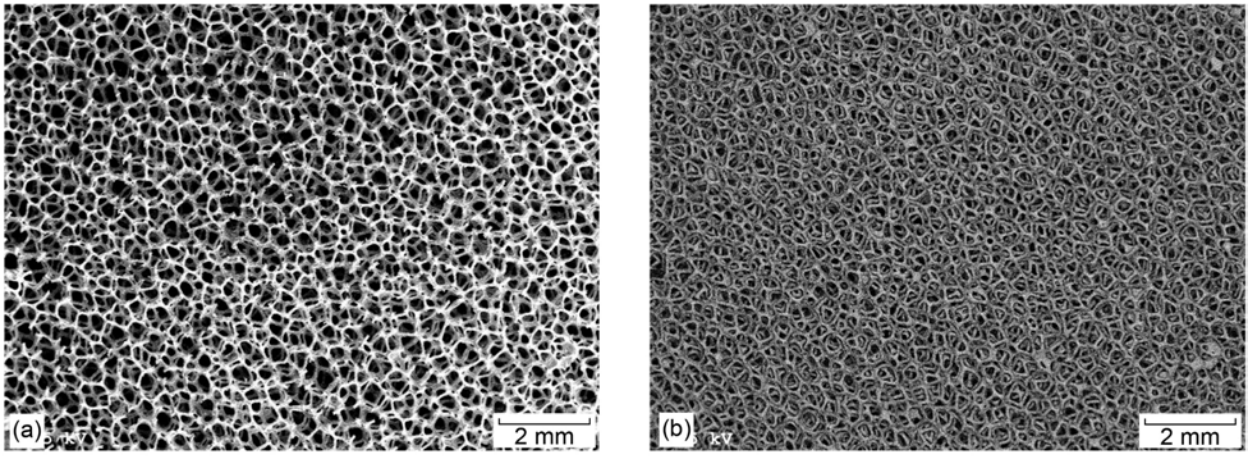

Figure 52.—Scanning electron microscope (SEM) imagery of the nickel metal foam. (a) Secondary electron (SE). (b) Backscattered electron (BSE).

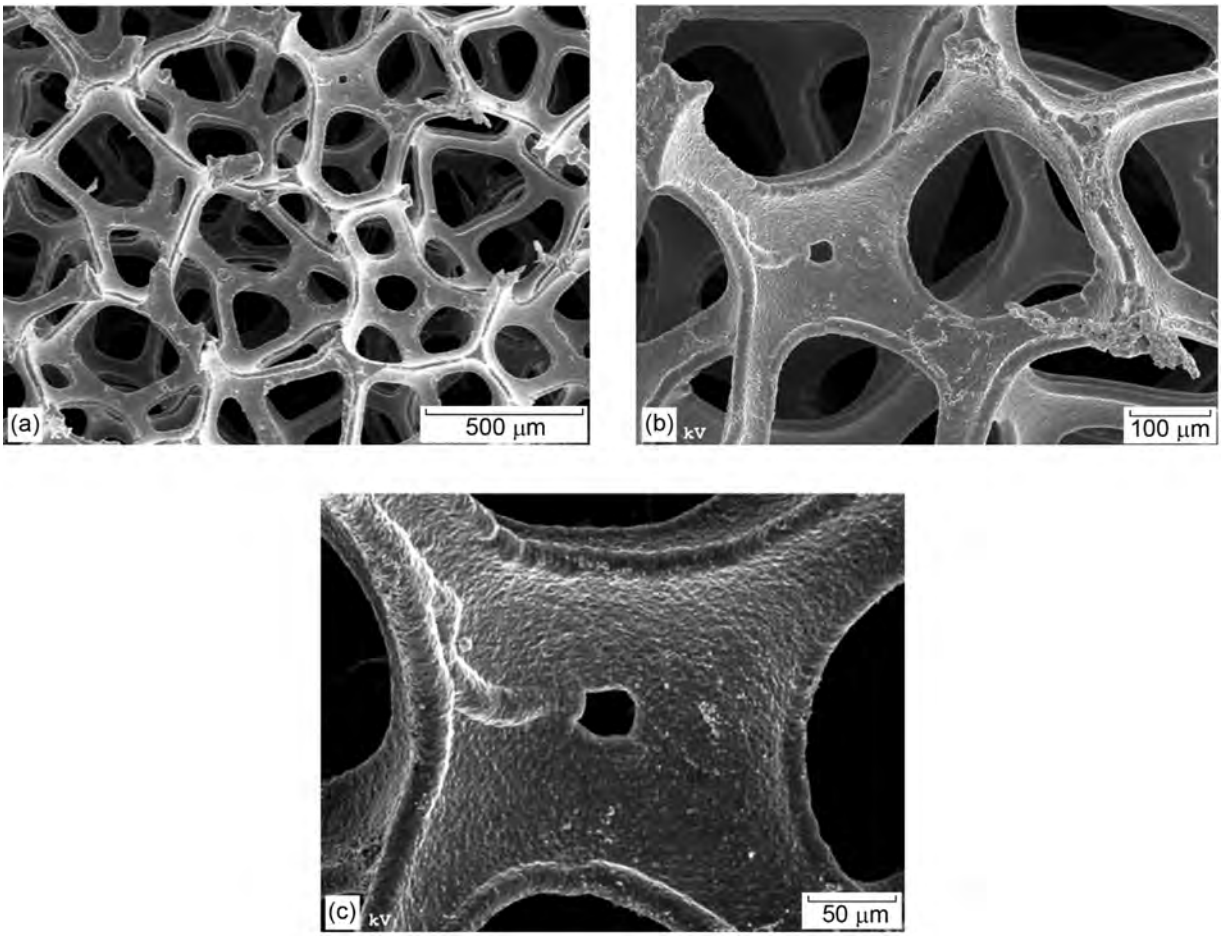

Figure 53.—High magnification of the nickel metal foam at 20 kV. (a) 500 μm. (b) 100 μm. (c) 50 μm.

The EDS spectra of four of the test areas scanned, Figure 54, show that the oxygen-cleaned nickel metal foam shows no appreciable contamination or other elements present within the metal matrix. This verifies that the nickel foam test samples are pure nickel.

For use within the reactor, the nickel foam was cut into disks that are stacked in an alumina-ceramic holder that positions them between the electrodes. For the testing, both plain nickel foam disks and powder-filled nickel foam disks are utilized, depending on the test being conducted.

To fill the disks with metal powder, a slurry of the metal powder and ethyl alcohol or acetone is used. The slurry is then pressed into the metal foam. After they are filled, the disks are stored within a vented hood where the carrier liquid is allowed to evaporate. The disks are weighed before and after filling to determine the amount of metal powder present in each disk. Figure 55 shows a piece of filled nickel foam and a filled nickel foam disk. From the figure, it can be seen that the powder fully fills the voids within the nickel foam. High powder densities within the foam can be achieved through this filling method.

Various types of metal powders were utilized in the testing. These included

- Vale nickel powder T123™, 99.8 percent pure, 3.5 to 4.0 μm particle size
- Titanium powder, 99.55 percent pure, 325 mesh (44 μm)
- Titanium deuteride powder

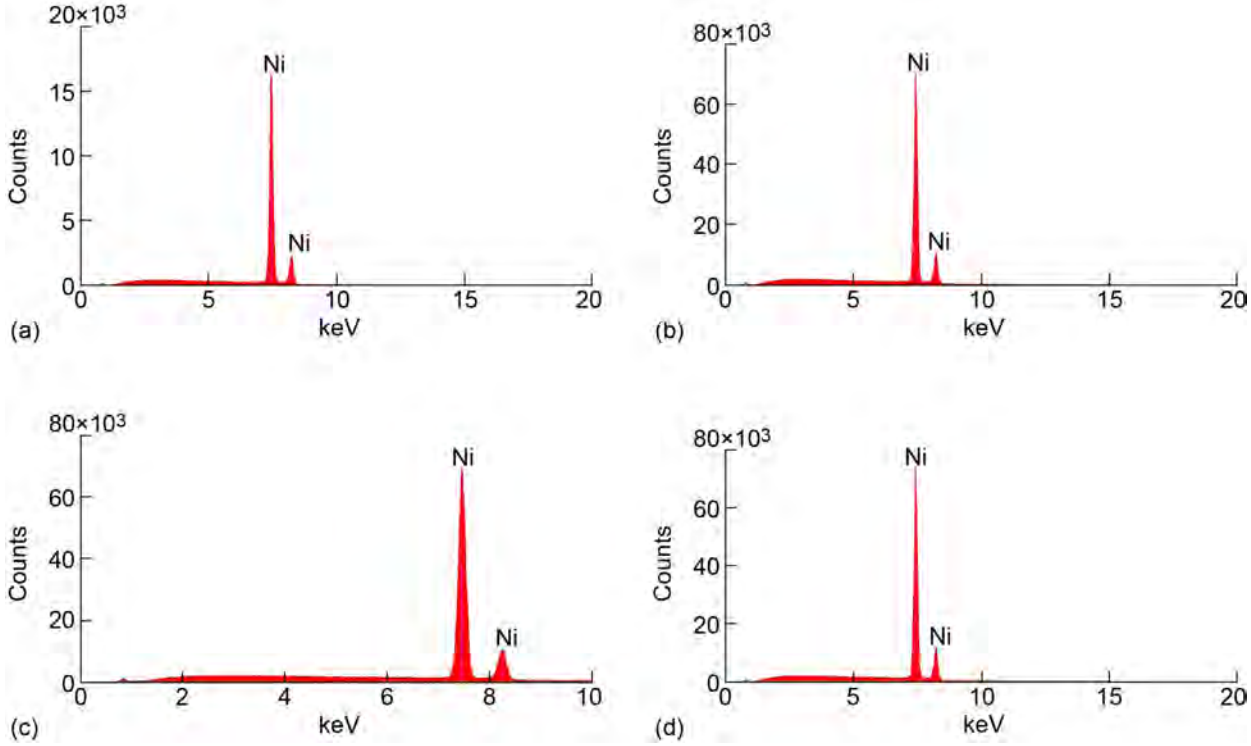

Figure 54.—Energy dispersive spectrum (EDS) analysis spectra of the nickel foam. (a) Sample 1. (b) Sample 2. (c) Sample 3. (d) Sample 4.

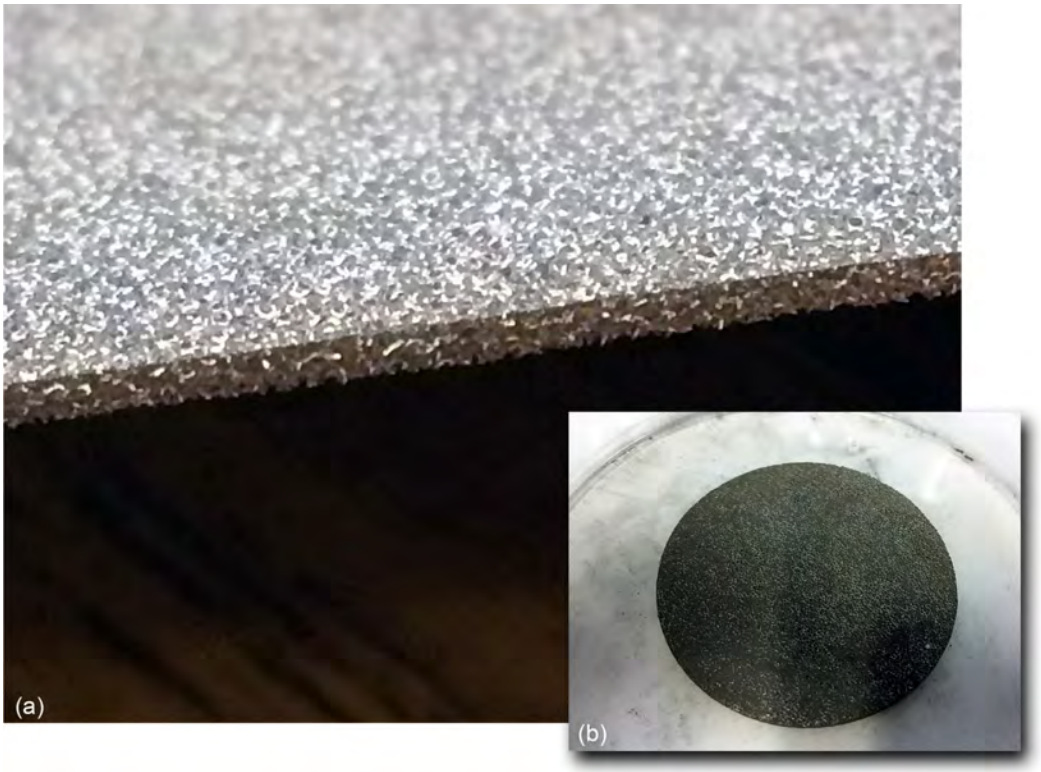

Figure 55.—Nickel foam samples filled with metal powder. Inset shows test sample disk.

The disks are stacked in an alumina-ceramic holder and placed within the reactor. The disk stacking arrangement is dependent on the specific test. For example, a test with powder-filled disks will typically utilize eight powder-filled disks, 44 unfilled nickel foam disks, and three silica spacers. The spacers are utilized to place a nonconductive gap between two adjacent disks. Because current cannot conduct through the spacer, a plasma is forced to form within the gap produced by the spacer. Therefore, in this type of disk stack arrangement, there are five locations where plasma will form during testing. These are at each end of the stack between the final disk and the electrode and across the three gaps where the spacers are located. For all the current testing, this three-spacer arrangement has been utilized, which is illustrated in Figure 56. In this figure, the darker colored disks represent the nickel metal foam disks that are filled with nickel powder if that material is being utilized.

The test disks are held within a ceramic holder that is positioned between the two electrodes. The disk stack and holder are positioned relative to the electrodes by a ceramic tube that surrounds the electrodes and extends slightly beyond them. The gap between the electrode and the first disk in the stack is approximately 3.3 mm. This arrangement is illustrated in Figure 57.

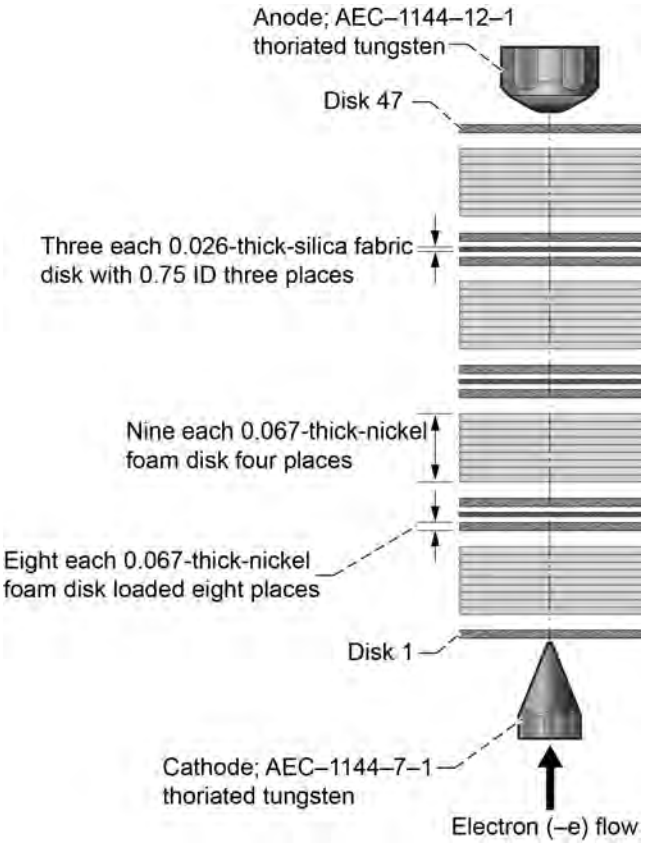

Figure 56.—Metal foam disk test arrangement. Dimensions in inches.

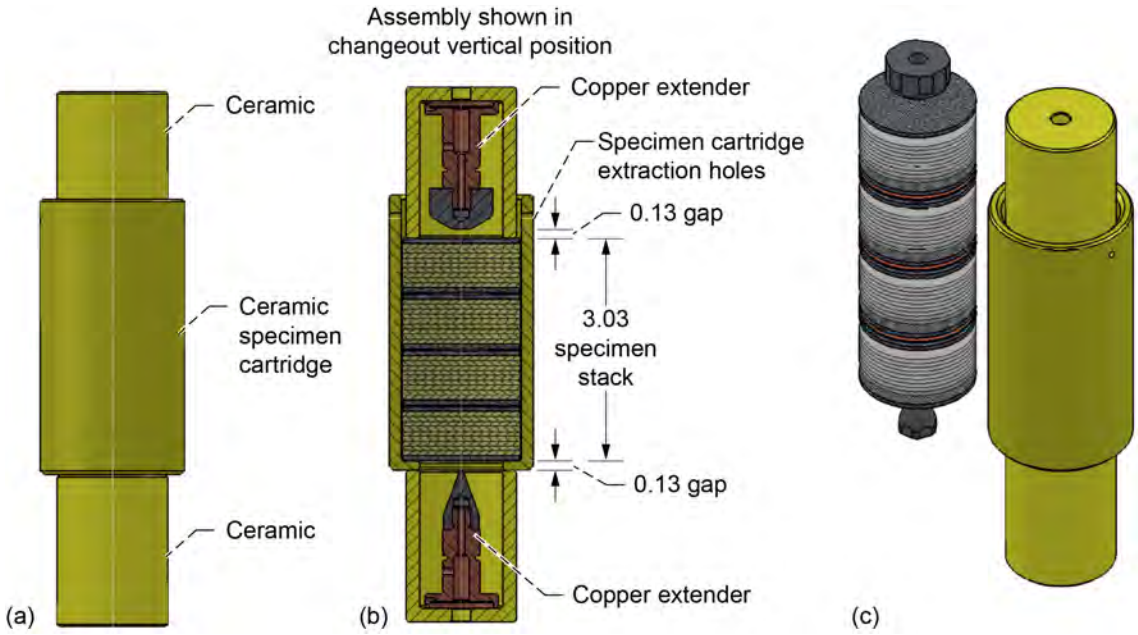

Figure 57.—Disk stack and holder arrangement. Dimensions in inches. (a) Ceramic specimen holder. (b) Cross section of ceramic specimen holder. (c) Specimen stack and ceramic holder.

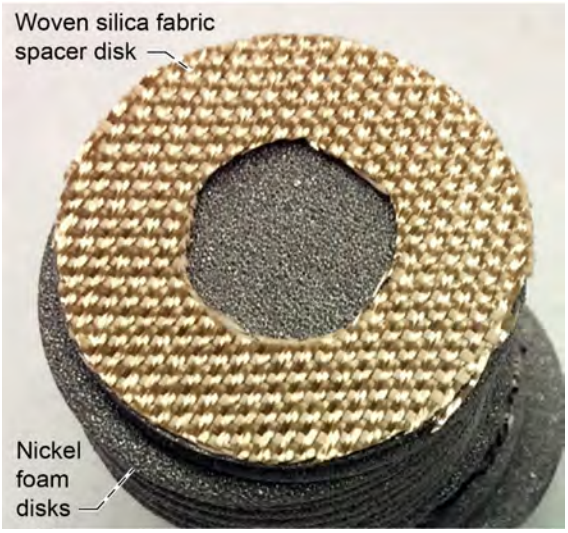

Figure 58.—Silica spacer with nickel metal disk.

The spacers are constructed of a woven silica material. They are cut into a donut-shaped ring to provide a gas space between the two adjacent disks. The silica cloth is constructed of 96 percent amorphous silica fibers and can withstand a continuous temperature of 982 °C with a melting temperature of 1,649 °C. A picture of the silica spacer is shown in Figure 58.

An analysis of the cleaned silica spacer material was also performed. This analysis showed that it was primarily composed of silicon with some additional minor trace elements present. These results are shown in Figure 59.

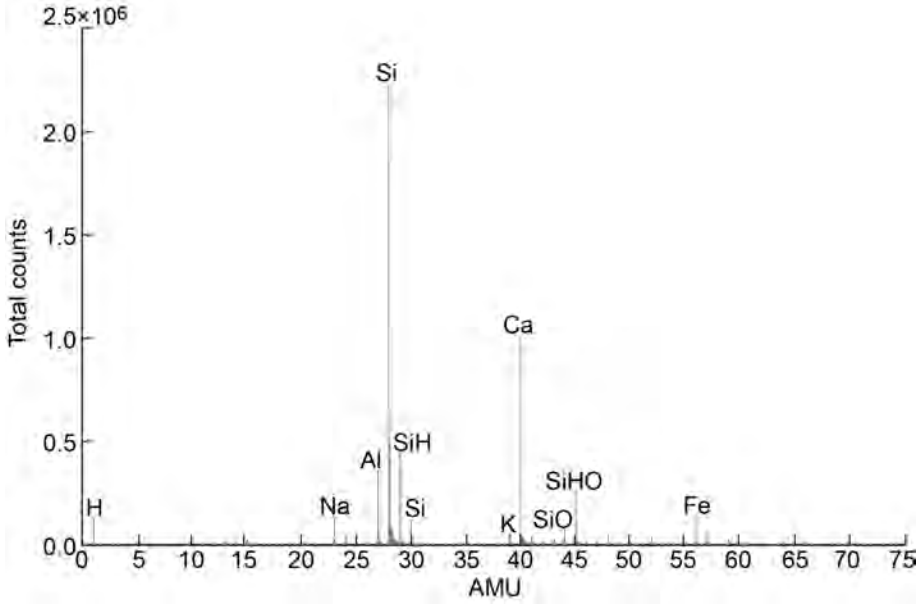

Figure 59.—Silica spacer material composition.

Figure 60.—Stanford Research Systems (SRS) residual gas analyzer (RGA) model RGA200 installed in test stand. Inset shows uninstalled SRS RGA.

6.0 Residual Gas Analyzer Sampling Summary

The gas within the reactor can be sampled during the testing. The gas sampling is performed utilizing a Stanford Research Systems (SRS) RGA model RGA200, shown in Figure 60. The SRS RGA is capable of measuring the concentration of gases up to 200 amu with a resolution of 0.5 amu.

The RGA is installed on the main high-vacuum line of the reactor system as illustrated in Figure 9. During testing, the line is pumped down to approximately 10^{-5} to 10^{-7} torr by the turbopump. A servovalve connecting the main high-vacuum line to the chamber is pulsed to allow a small amount of gas to enter the vacuum line where the RGA resides. This gas is read by the RGA to show its composition as shown in Figure 61.

The scans are taken periodically during a test to provide a record of the gas composition and changes during a test. This is shown in Figure 62. At the beginning of the test, prior to the plasma being ignited, there is initially no gas in the chamber. Then the chamber is filled with deuterium (amu of 4) gas. The predominance of deuterium gas can be seen in the 7:05 a.m. scan. After that, the plasma is ignited and the test begins. The gas composition within the chamber slowly changes throughout the test. The deuterium level gradually drops, and gases with other amu values rise.

7.0 Gas Capture System and Procedure

In addition to the RGA analysis, the gas within the chamber can be collected and stored after the test is completed for further analysis. The gas is captured in an evacuated lecture bottle and sealed. Also prior to the initiation of the test, a control gas sample is collected. This is used to establish a baseline to determine what changes in the gas occurred during the testing. The gas collection system utilizes the test stand turbopump and roughing pumps to evacuate and fill the sample bottle. A diagram of the gas collection system is given in Figure 63.

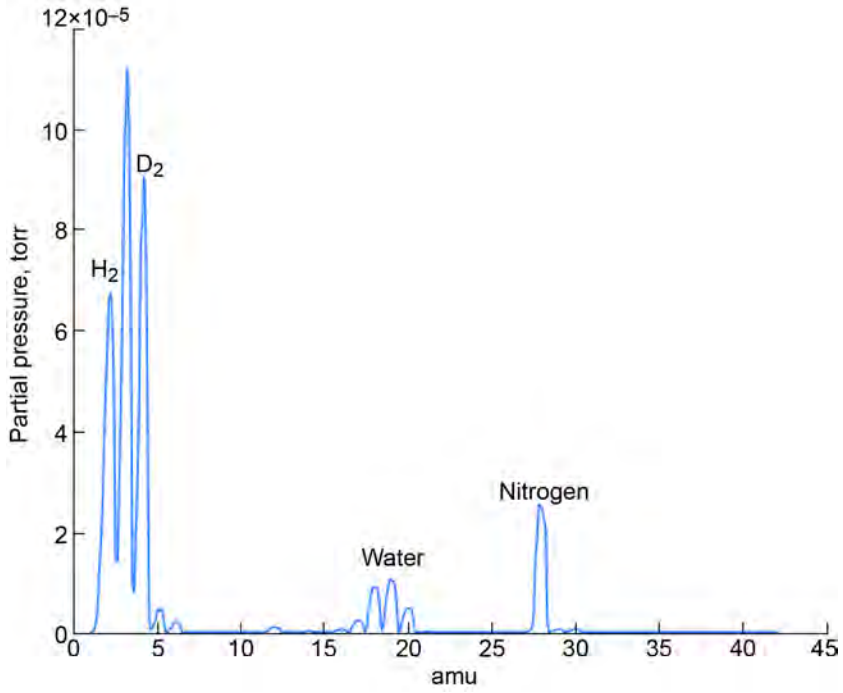

Figure 61.—Typical residual gas analyzer (RGA) scan of gas within the chamber. Scan taken during test shows presence of water and nitrogen due to air in chamber. Water forms from oxygen in air combining with deuterium and/or hydrogen in chamber thus eliminating most oxygen and leaving nitrogen as main component from air.

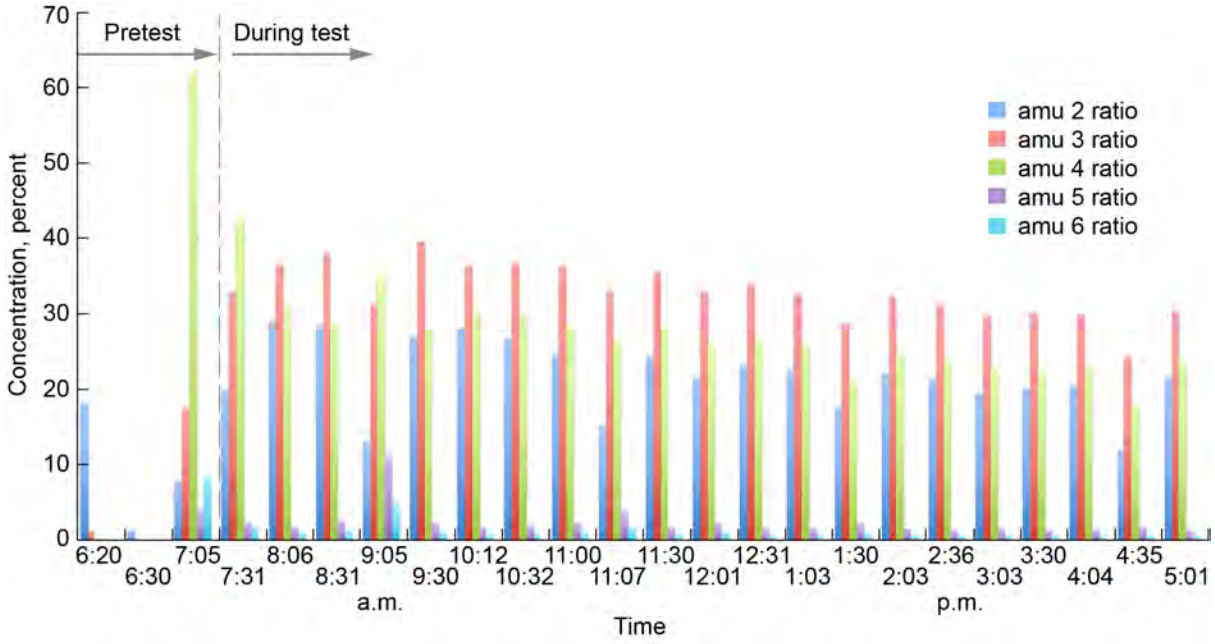

Figure 62.—Residual gas analyzer (RGA) scan results taken periodically during a test.

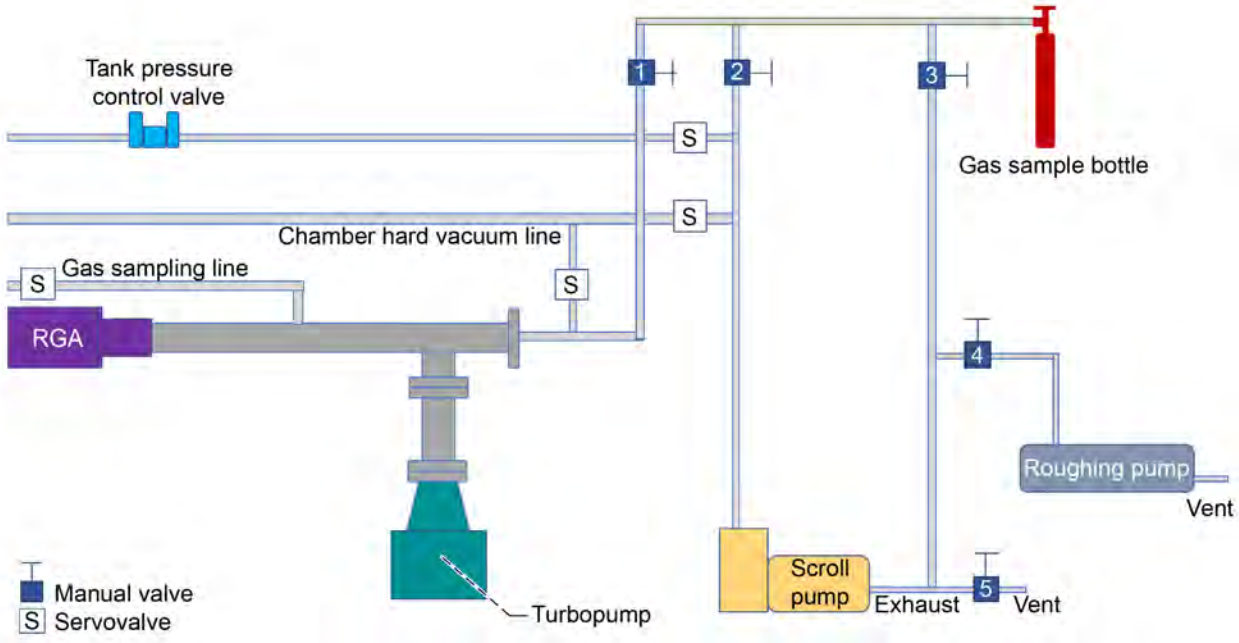

Figure 63.—Gas collection system layout with residual gas analyzer (RGA).

The control gas sample is collected at the beginning of the test before the plasma is ignited. The control gas is taken just before the test starts so that the reactor is in the same operational condition as when the gas sample is collected at the end of the test. Also, the control gas sample is acquired through the same method that the test gas sample is acquired. This provides a reliable and comparable control gas to that of the test sample gas. The gas collection process is set up to minimize the amount of air that can become mixed with the gas sample. The process for collecting the control gas and the test gas sample is outlined as follows:

1. Fill the chamber to the desired pressure with the test gas.
2. The initial state of the manual valves is MV1: Closed, MV2: Closed, MV3: Closed, MV4: Closed, MV5: Open.
3. Attach the sample bottle to the gas collection line.
4. Open the valve on the gas sample bottle and open MV2. This will pump down the gas sample bottle to approximately 10^{-2} torr.
5. Once the pressure in the bottle is within this range, open MV1 and close MV2. Let the bottle pump down for at least 15 min or until the pressure within the bottle stops dropping. It should be within the 10^{-3} to 10^{-5} torr range. Record the bottle pressure.
6. While the bottle is being pumped down, open MV4 and close MV5. This will pump down the exhaust line from the scroll pump.
7. Close MV1, Close MV4, and Open MV3.
8. Set the tank pressure controller to 0 torr. The control valve will open evacuating the chamber with the scroll pump. The exhaust from the scroll pump is sent to the evacuated bottle.
9. Once the chamber is evacuated, record the bottle pressure and close the sample bottle valve. The chamber gas is now captured in the bottle.
10. Remove the gas sample bottle.

8.0 Reactor Operation and Test Procedure

The main control and data collection system is utilized to operate the reactor and collect the test data. The control system provides the ability to regulate the gas composition and pressure within the reactor, set the coolant flow rate, set the heater power level, and set the pulsed plasma parameters. It is also used to periodically collect data from the RGA by sending a gas sample to the high-vacuum line. The process for setting up the reactor and conducting a test utilizes the outlined steps as follows. The overall operation procedure for running a test is given in Appendix C.

8.1 Install Test Sample

To install the test samples, the reactor is disconnected from the cooling water lines, the anode and cathode sensor boxes, and the gas and vacuum input lines. Once disconnected, the reactor is raised from its horizontal position to a vertical position as shown in Figure 64.

The anode electrode endcap is removed providing access to the reactor interior. With the reactor open, a test material sample is installed. The test disks are stacked along with their spacers in a predetermined order as illustrated in Figure 56 and Figure 57. Once the disks are in the ceramic holder, the holder is placed into the reactor chamber as shown in Figure 65.

After the disk stack is in the reactor, the reactor is sealed and returned to its operational orientation. The anode and cathode sensor boxes are then reconnected along with the water and gas lines.

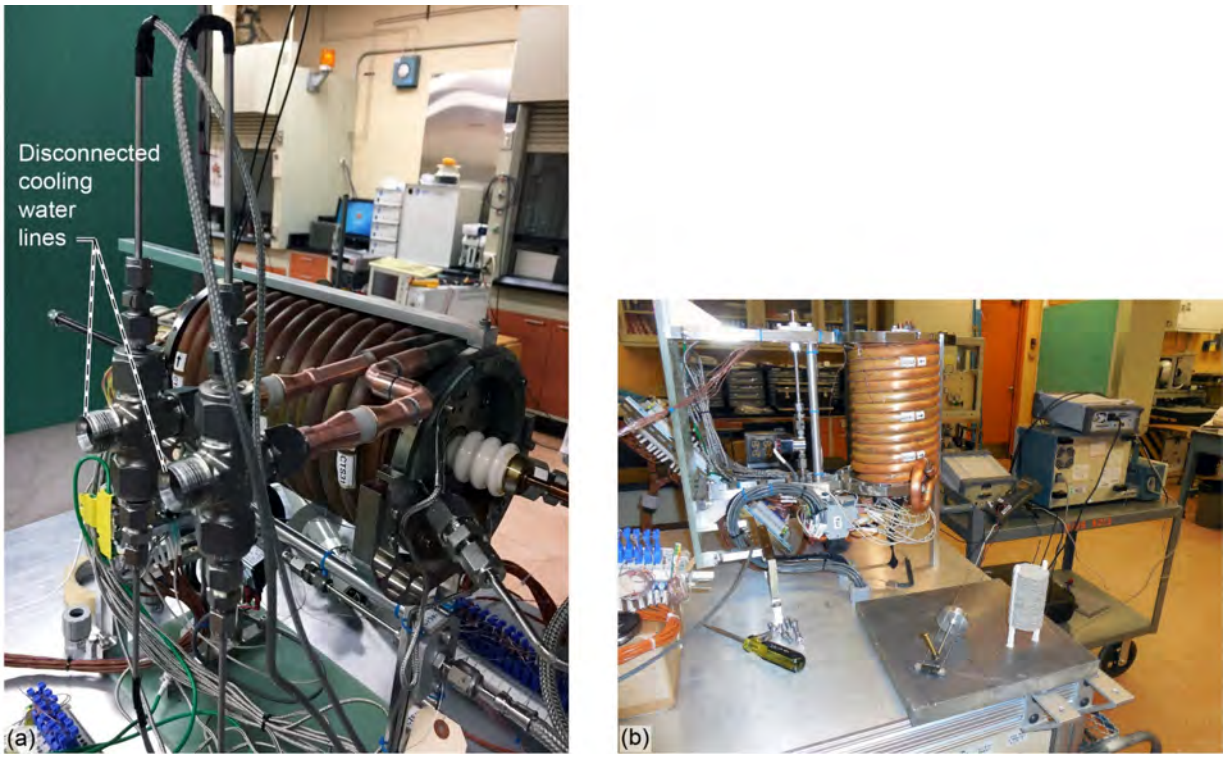

Figure 64.—Reactor orientation for testing and sample loading. (a) Horizontal operational position with disconnected cooling water lines. (b) Vertical position for sample installation.

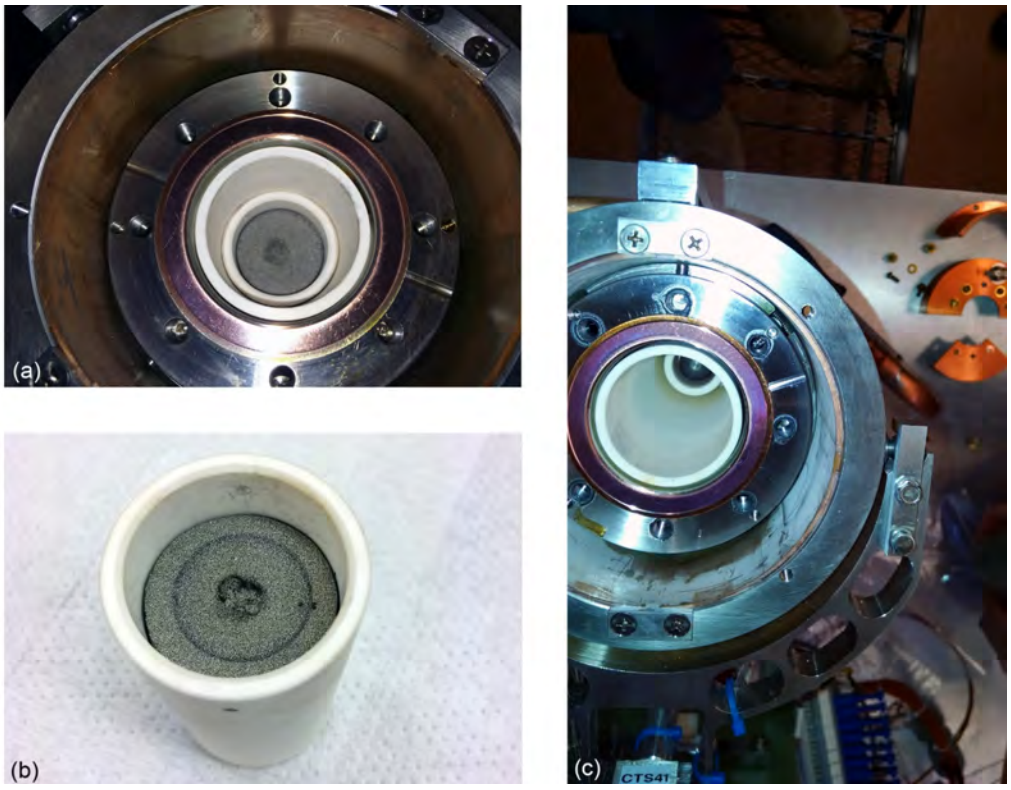

Figure 65.—Test disk stack placed within the reactor. (a) Ceramic holder with test disks in reactor. (b) Test disks in ceramic holder. (c) Test chamber.

8.2 Verify Reactor Setup

Once the reactor is in its horizontal operating position and all the operational connections have been made, the reactor system is tested for leaks. Operation of the chiller is started to verify the coolant is flowing correctly and there are no leaks in the coolant line fittings.

After the coolant system integrity is established, the chamber seals (ConFlat® flanges) are tested. A vacuum is pulled on the chamber utilizing at first the roughing pump and then the turbopump. The roughing pump is turned on and opened to the chamber. If there are no significant leaks in the vacuum line or chamber seal, the chamber should be able to be pumped down into the mtorr range within about one-half hour. If the chamber successfully reaches this vacuum level with the roughing pump operating, then the turbopump is turned on. If there are no leaks into the chamber, the turbopump should be able to pump the chamber down to a pressure on the order of 10^{-4} or 10^{-5} torr. However, to reach this level may take overnight operation depending on how much moisture was on the new disk set that was installed.

If these low vacuum levels cannot be achieved, then a leak is most likely present. To diagnose the leak, initially retighten the vacuum line fittings and the anode end flange bolts. Observe the chamber pressure, if it begins to drop, then a loose fitting or seal was most likely the source of the leak. If the problem persists, then the RGA along with a helium gas source can be used as a leak detector. The RGA has a helium-leak detector mode that can be selected after starting the RGA. Release small amounts of the helium gas around the vacuum line fittings and flange ends to see if helium is detected by the RGA. If a spike in helium is observed, then that is a leak source.

8.3 Insulation Installation

Once it has been verified that the reactor and cooling system are sealed, then the insulation can be installed on the reactor. The custom insulation wrap is composed of a number of foam pieces that are positioned around the reactor and secured together to form a sealed insulation wrap as shown in Figure 66.

1. The insulation wrap begins with a permanently installed block of insulation that fits underneath the reactor. This insulation block, shown in Figure 66(a), is secured around the reactor frame and does not need to be removed to install disks into the reactor.
2. The next piece of insulation wraps over the central body of the reactor as shown in Figure 66(b).
3. Once the centerpiece is in place, insulation pieces on ether end of the reactor are added on. These pieces cover the area where the electrodes, wiring, and gas and vacuum lines connect to the reactor. These pieces have a large circular cutout at their center to accommodate these connections to the reactor.
4. These pieces are secured to the center insulation section with Velcro® straps that run the length of the reactor as shown in Figure 66(c). Once in place, the end holes in these pieces of insulation are filled with high-temperature silica insulation. This insulates that area around the electrodes and up to the end flanges of the reactor as well as any area where voids are created to allow for wires or tubing to pass through the insulation.
5. Once those spaces have been insulated, the insulation endcaps are installed and secured with Velcro® straps as shown in Figure 66(d).
6. The last step is to compress the insulation to eliminate any gaps between the joints. This is accomplished by positioning four straps around the reactor body. Underneath the two central straps, polyester insulation is layered to help seal the joints between the insulation sections.
7. Once the straps are installed, two end supports are put in place and connected with threaded rods. The bolts on the rods are tightened to compress the insulation forming a tight seal between the insulation segments.

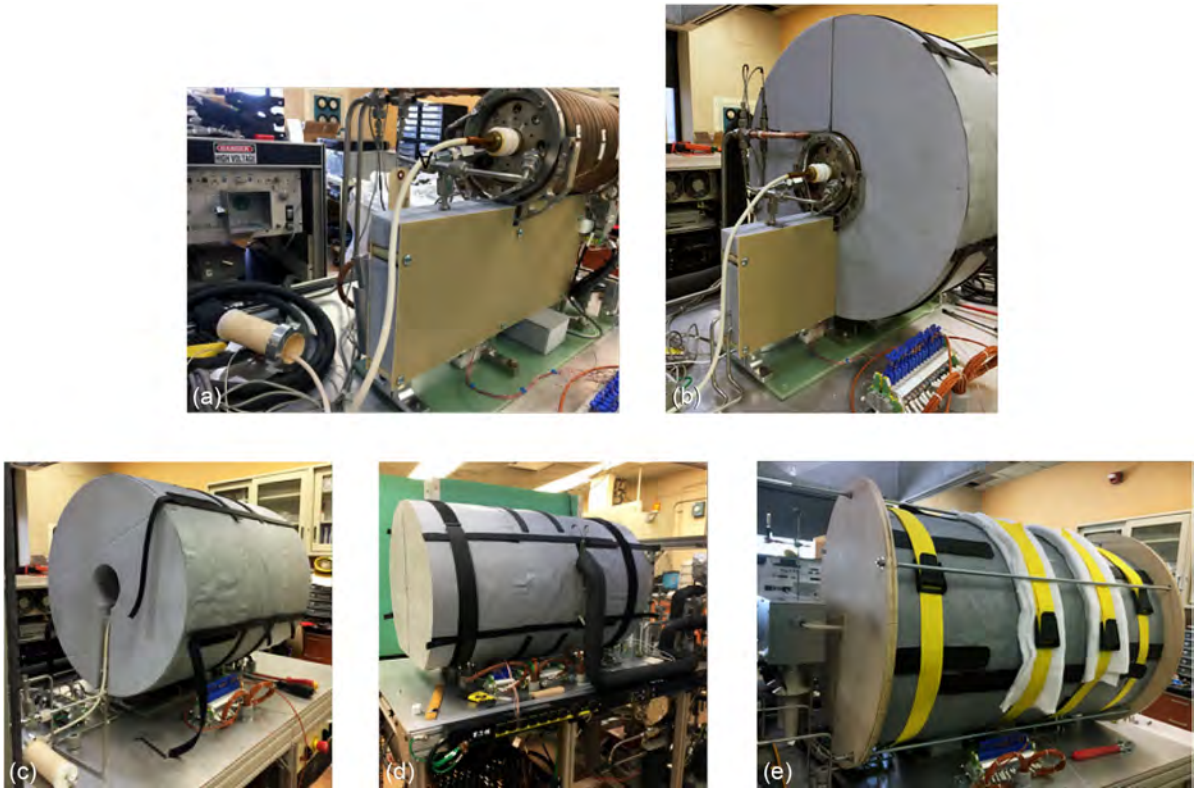

Figure 66.—Reactor insulation wrap steps. (a) Insulation wrap around frame. (b) Insulation wrap around central body of reactor. (c) Velcro® straps securing center insulation. (d) Endcap insulation and securing Velcro® straps. (e) Completed and secured insulation.

8.4 Pretest Setup

With the test disks installed in the reactor and the insulation in place around the reactor, the pretest setup is performed. These items are performed to prepare the reactor to begin testing. The pretest setup is as follows.

The first step is to start the cRIO data system and LabVIEW control software. Initiate a new data file to collect data on the pretest and test. There are a number of other parameters that can be set, such as the real-time data graphs for observing some of the data during the test. In addition, all of the other ancillary test equipment is turned on, such as the RGA, radiation detection equipment and spectrum analyzer.

To set the cooling flow parameters, start the chiller and set the flow rate through the reactor and the chiller output temperature. The flow rate is set through the LabVIEW console and the chiller output is set at the chiller.

The heaters are turned on to begin the heatup process. This process is usually performed overnight to establish a net output power baseline for the test. The heater power supply is turned on manually at the test stand and the output power is set at the control computer. The baseline operating power for the heaters is approximately 825 W. Once the heaters are turned on, the reactor system will take a few hours to equalize in temperature due to the thermal mass of the reactor itself as shown in Figure 67. This figure shows the net power out of the calorimeter after the heaters are turned on. Initially the power level is negative as the heat from the heaters goes into raising the temperature of the reactor system. The initial negative net power value is approximately –1,100 W. The reason this is more than the heater power level of 825 W is that the chiller water temperature is set to 57 °C to begin the test. The coolant water

temperature is being raised to this level by the chiller, as shown in Figure 12, providing additional heat to the system. After approximately 300 min, a steady-state equilibrium temperature is reached between the heater input power and the heat removed from the system by the calorimeter cooling water. Once the equilibrium is established, the reactor temperatures remain constant. Also shown in Figure 67 is the ΔT, the difference between the calorimeter's output and input water temperatures in °C.

The next step in the startup process is setting the pressure within the reactor. If there is a significant moisture content within the reactor, it may be desirable to perform the heatup process under vacuum overnight. This will bake out the moisture from the interior. However, operating under vacuum prevents the interior of the reactor from heating up effectively. If heated under vacuum, once gas is added, a drop in the output power to the calorimeter will be seen due to the gas providing a more effective means of heating the interior. This is shown in Figure 68. The addition of the gas will require at least an additional 90 min for the system to return to its baseline net power output.

When the gas is added, a number of purge and fill cycles are performed to ensure clean gas (e.g., deuterium) within the reactor. This is done just before the test begins whether the gas is added before the initial heatup process or afterwards. Usually five purge and fill cycles will be performed. Once these are completed, a control gas sample is taken and then the reactor is pressurized to the desired test operating pressure. The gas capture process is described in Section 7.0.

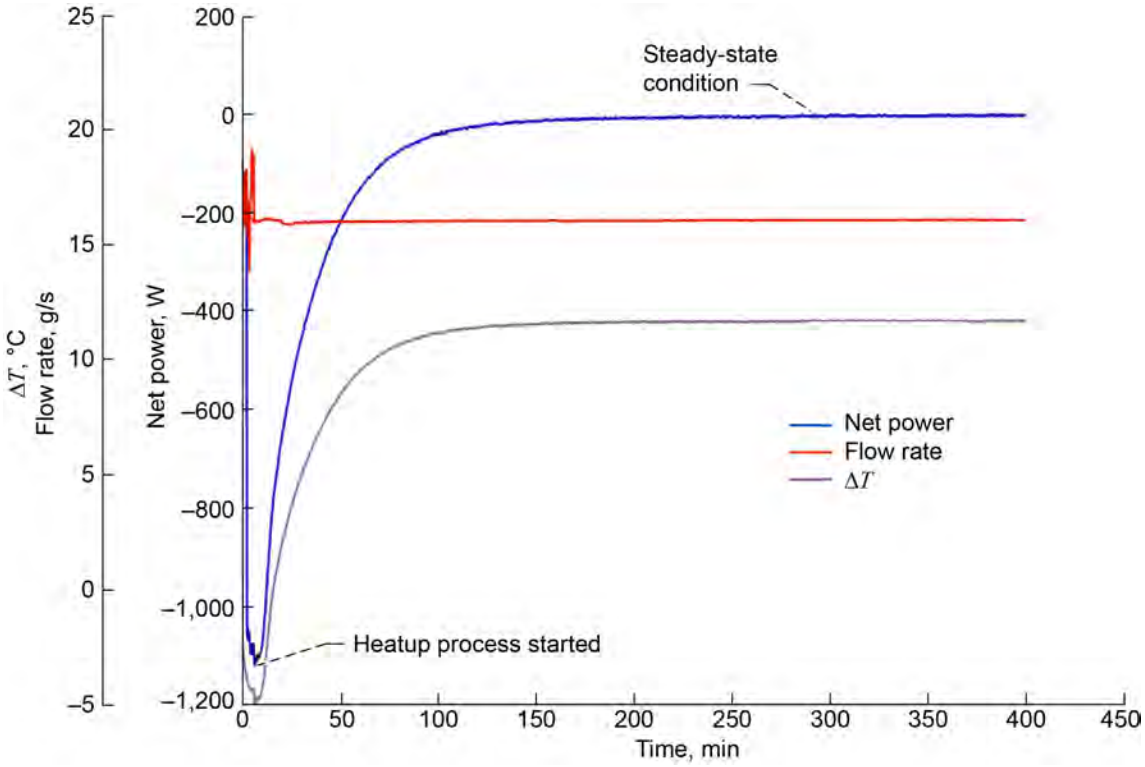

Figure 67.—Reactor initial heatup.

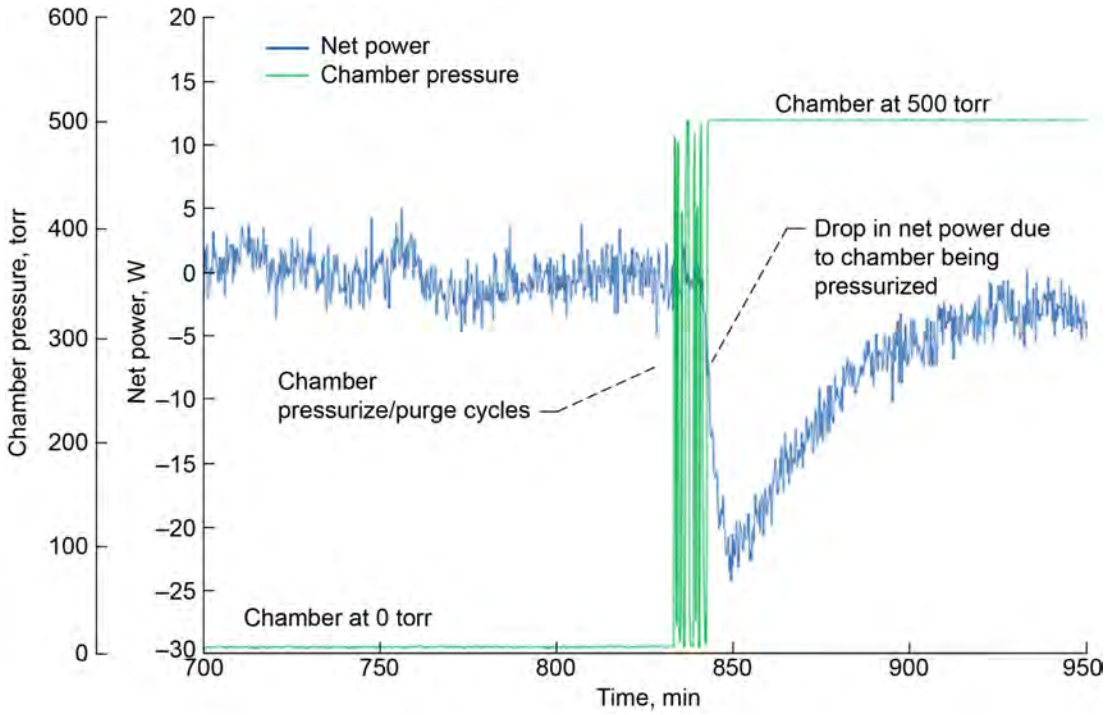

Figure 68.—Drop in net power due to reactor being pressurized by test gas. Sufficient time is provided before starting plasma to allow zero net power to be realized.

8.5 Test Startup

After the control gas is obtained, the test can begin. This is done through the control system computer by initiating the plasma by setting the power supply voltage and sending a pulse waveform to the high-voltage switch.

The test will continue as long as the pulse waveform is supplied to the high-voltage switch. For baseline test operation, the pulses are set at a 25-percent duty cycle and 230-Hz frequency. The power supply voltage is usually set to 10 kV although the actual voltage across the reactor will depend on the internal resistance within the chamber, which in turn is dependent on the following:

- The properties of the material being tested
- The number of plasma gaps within the test material stack
- The plasma gap width
- The gas within the reactor

8.6 Test Shutdown

The plasma will be pulse ignited for the duration of the test. A typical test can run from 8 to 24 h. Once the desired time is completed, the test is stopped. This is accomplished by setting the output voltage of the plasma power supply to zero, then turning the switch pulse frequency and duty cycle to zero.

With the plasma extinguished, the test gas is collected. The gas collection process is the same as that for the control gas sample taken prior to the test starting described in Section 7.0. Once the test gas is collected, the chamber is cooled down. The heater power supply is turned off by first setting its voltage to zero and then physically turning off the supply. The chiller temperature is lowered to room temperature

approximately 23 °C. The cooldown process will take approximately 1 h if the disks are going to be left within the chamber and 2 h if the disks are to be removed.

If the test disks are to remain within the chamber, the chiller is operated until all of the reactor and heater block temperatures are below 100 °C. If the disks are to be removed from the reactor, then the chiller is operated until the reactor and heater block temperatures are under 30 °C. Once these temperatures fall below the desired level the chiller is turned off and the remainder of the test system equipment turned off (RGA, radiation detectors, and spectrum analyzer). The LabVIEW control software is then stopped, and the data file is retrieved from the cRIO. After the data file is collected, the cRIO and the control computer are turned off.

9.0 Design of Experiments Testing Design

To evaluate a number of different test parameters, a design of experiments test matrix was generated. The test matrix addresses a number of factors that are thought to have an influence on the measurable output and material effects from the plasma reactor. The number of these factors is thought to be too large to complete a refinement study, as the test matrix and test duration would exceed allowable schedule. The objective is to reduce the number of controllable factors to those that have the greatest influence on the output. After reducing the number of factors to only those which are highly influential, a refinement design study would be conducted to optimize the process within those factors previously considered.

9.1 Factors

There were a number of factors discussed. Factors believed to have an influence, but the level of influence was questionable, were included. Two types of materials were chosen based upon variation in material properties. Based upon allowable schedule, the number of experiments in the screening design matrix was limited to 12. The factors considered were:

1. Material
2. Current level
3. Pulse frequency
4. Duty cycle
5. Gas pressure
6. Rig temperature
7. Gap thickness (number of silica inserts per gap)
8. Gap number (number silica gap locations)

9.2 Number of Experiments

The number of experiments in an eight-factor screen was predetermined as 12. This number has an influence on the sensitivity of identifying an influence of a factor. Using 12 experiments, the screen has an 80 percent chance of detecting effects 1.9 standard deviations from the mean, that is, a moderate influence. Alternately, the number of experiments may be set to 24. This number has an 80 percent chance of detecting affects 1.1 standard deviations from the mean, that is, a relatively small influence.

9.3 Experiment Design

The 12 experiments must be run in this random order (Table 10) to minimize any bias from unknown and uncontrolled factors.

TABLE 10.—DESIGN OF EXPERIMENTS

Run order	Material	Current	Pulse frequency	Duty cycle, percent	Pressure, torr	Temperature, °C	Gap thickness, each	Gap number, +2 electrode	Response
1	Ni foam	Low	High	25	500	300	3	6	
2	Ni foam + TiD2	High	High	8	500	450	1	6	
3	Ni foam + TiD2	High	Low	25	500	300	3	3	
4	Ni foam + TiD2	Low	Low	8	500	450	3	3	
5	Ni foam + TiD2	Low	High	8	10	300	3	6	
6	Ni foam	High	Low	8	10	450	3	6	
7	Ni foam	High	High	8	500	300	1	3	
8	Ni foam	Low	Low	25	500	450	1	6	
9	Ni foam	Low	Low	8	10	300	1	3	
10	Ni foam	High	High	25	10	450	3	3	
11	Ni foam + TiD2	Low	High	25	10	450	1	3	
12	Ni foam + TiD2	High	Low	25	10	300	1	6	

9.4 Levels

The levels to be considered, both high and low, should be those that are expected to produce a meaningful response. Those considered to produce a null value are not expected to contribute to the understanding of the system and were therefore excluded from consideration.

9.5 Expected Output

After the response for the 12 experiments is included into the screening model, the design is expected to estimate the linear main effects for each of the factors. Interaction between factors is not expected with this experiment design. The analysis is expected to determine which factors are significant and which would be excluded from the optimization experiment phase.

9.6 Parallel Study

In order to investigate the influence of a third material, a parallel study would be conducted. Each time the above test matrix calls for the second material to be tested, the third material will also be tested under the same prescribed conditions as the second material. By conducting the tests in this manner, the same statistical analysis will be completed, and the total number of experiments will be increased from 12 to 18.

10.0 Example Test Results and Discussion

A checkout test was performed on April 27, 2017, to test the functionality of the reactor, associated systems, and data collection. This checkout test consisted of an initial heatup period, which lasted 16 h, then an operational period, where the plasma was ignited, that lasted approximately 24 h. After which, the test was concluded and the reactor shut down. All of the data presented in this section were obtained during this test. The baseline operating conditions for the test are given in Table 11.

The main output of the collected data is the net power out of the reactor. As described in Section 3.0, the net power is the calculated calorimeter output power minus the sum of the heater and plasma input powers.

The different methods for calculating the plasma power-supply output were used to calculate the net power throughout the test. The net output power utilizing the RMS cathode current is shown in Figure 69, and for comparison of the same test, the net output power utilizing the RMS anode current is shown in Figure 70.

The net power shown in Figure 69 initially reaches a steady-state value prior to the plasma power supply being turned on. This steady state represents an equilibrium reached with the heated reactor. The steady-state value was adjusted to 0 W. Unadjusted, it was –37.9 W. This initial negative power level is due to thermal losses from the system that are not captured by the calorimeter output power. These losses are due to

- Heat loss through the insulation
- Heat loss down the heater wires and other instrumentation wiring
- Heat loss through the reactor support structure

TABLE 11.—TEST OPERATIONAL CONDITIONS

Variables
Chamber gas.....Deuterium
Chamber pressure, torr.....500
Pulse frequency, Hz 230
Pulse duty cycle, percent.....25

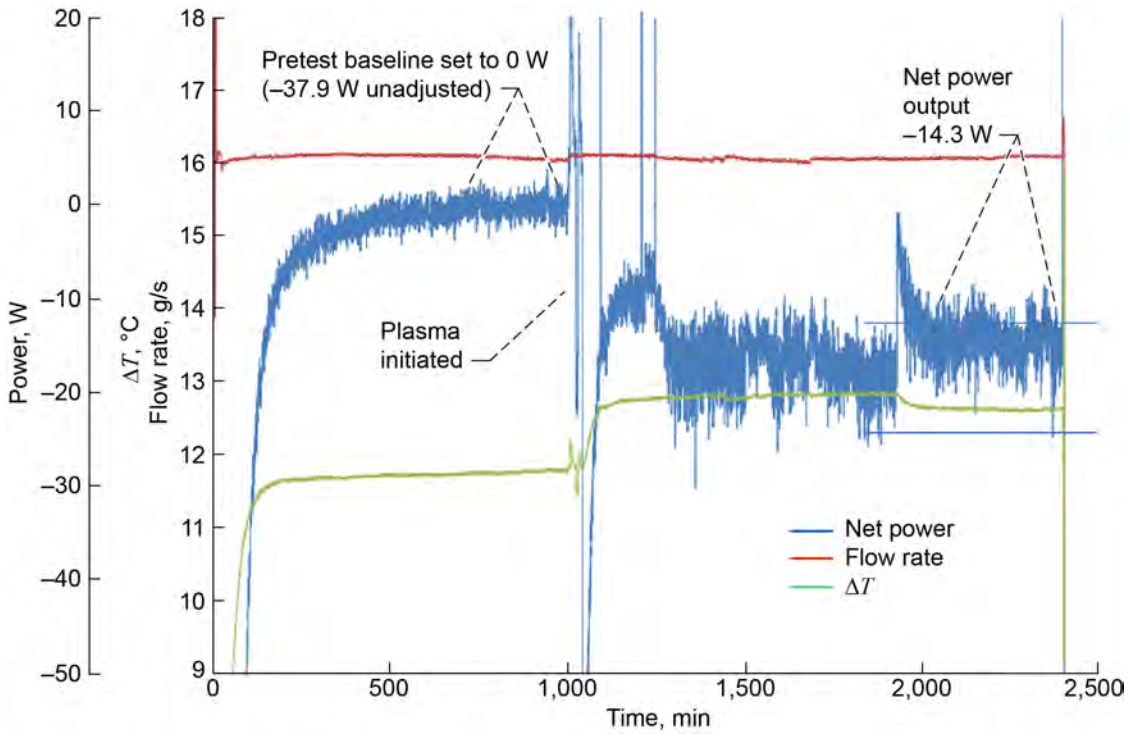

Figure 69.—Net output power based on root-mean-square (RMS) cathode current.

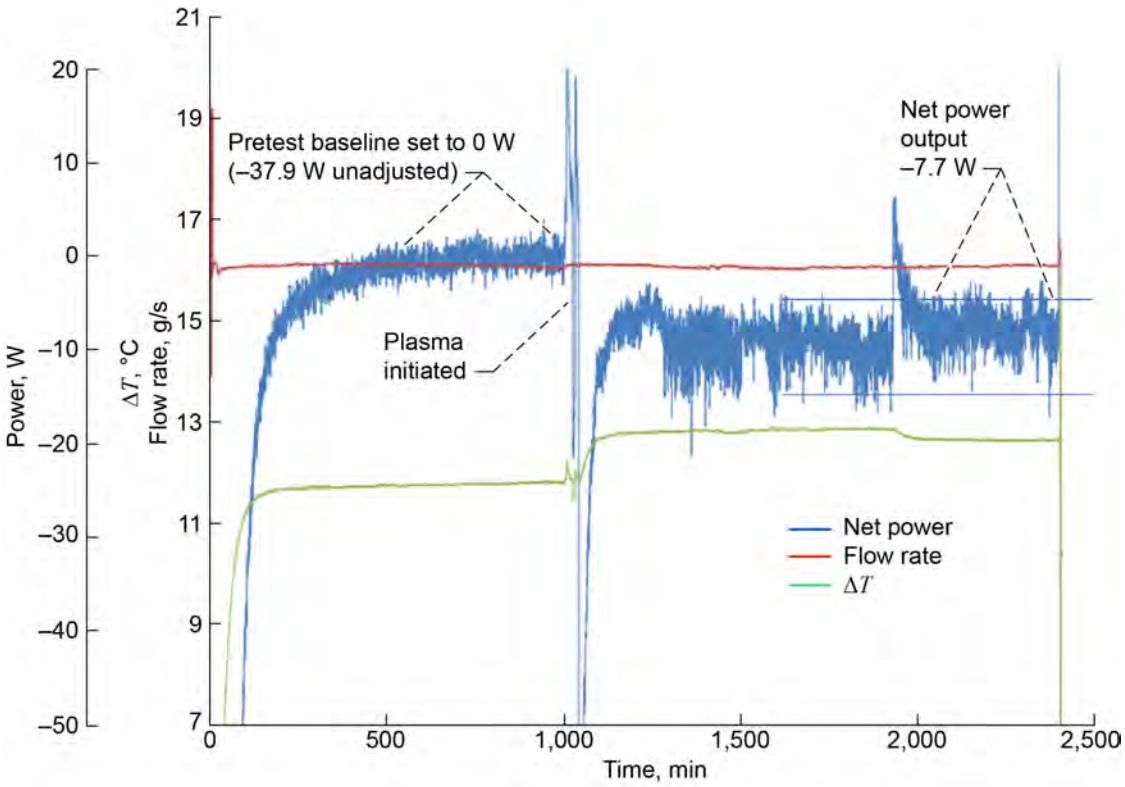

Figure 70.—Net output power based on root-mean-square (RMS) anode current.

Once the plasma is ignited, the net power level again drops. This large drop is due to the time lag between when the plasma generation power is inputted into the reactor and the heat from the plasma generation reaches the calorimeter. It has been estimated that the time lag to fully register a change in input power by the calorimeter is approximately 45 min. The net power rises back up but does not reach the initial 0 W steady-state baseline value. It remains at approximately –14.3 W. Also, the fluctuations in net power are much greater than that seen before the plasma was ignited. Both the inability to return to near the baseline power level and the larger fluctuations in net power are due to the inaccuracy in calculating the RMS value for the cathode current. This inaccuracy is caused by the significant fluctuations in cathode current output that occur during the test. A remediation is discussed in the following information.

To try to improve the net power measurement, the RMS of the anode current can be utilized to determine the net power as shown in Figure 70.

Using the anode RMS current does reduce the fluctuations in net power from approximately ±7 to ±5 W. In addition, the steady-state net power level with the plasma ignited increases to approximately –7.7 W. As with the RMS cathode current calculation, the fluctuations and drop in steady-state net power from the baseline are due to inaccuracy in calculating the RMS value for the anode current, which in turn is mainly due to the fluctuations seen in the anode input current.

To address this issue of inaccurately measuring the RMS current value, a different approach can be taken. As described in Section 3.0, the alternative is to measure the instantaneous power into the reactor by calculating the power (voltage × current) utilizing either the anode or cathode current. This instantaneous power will provide a single data point to the data system. Since the collected data points are insufficient to truly capture the output of a pulse or number of pulses, the instantaneous power data points are calculated and stored at a rate much greater than the data is stored in the data file. These instantaneous power values are held in a buffer and then averaged to provide the data point for the data file. The net power utilizing this method with the cathode current measurement is shown in Figure 71.

The net power based on the instantaneous plasma power-supply output has significantly lower fluctuations with the plasma ignited then the RMS-based net power. The net power fluctuations seen in Figure 71 after the plasma is ignited are similar to those seen prior to the test when establishing the pretest baseline. Also, the steady-state net output power during the test was just –1.06 W. This is very close to the 0 W baseline and the difference between the two is within the error of the power measurement system.

The net power was also determined using the instantaneous anode current as shown in Figure 72. These results are very similar to those seen in Figure 71 for the instantaneous cathode current. The steady-state net power utilizing the instantaneous anode current with the plasma ignited is –1.52 W, which is also within the net power measurement accuracy.

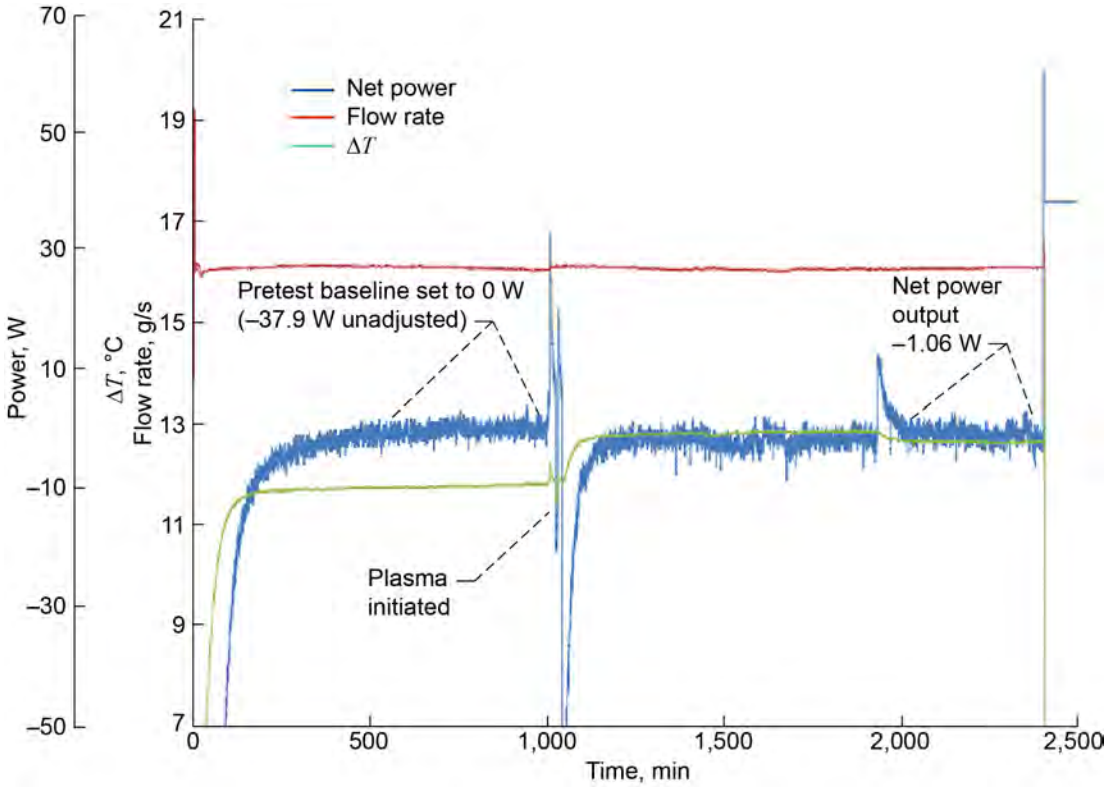

Figure 71.—Net output power based on cathode current instantaneous power.

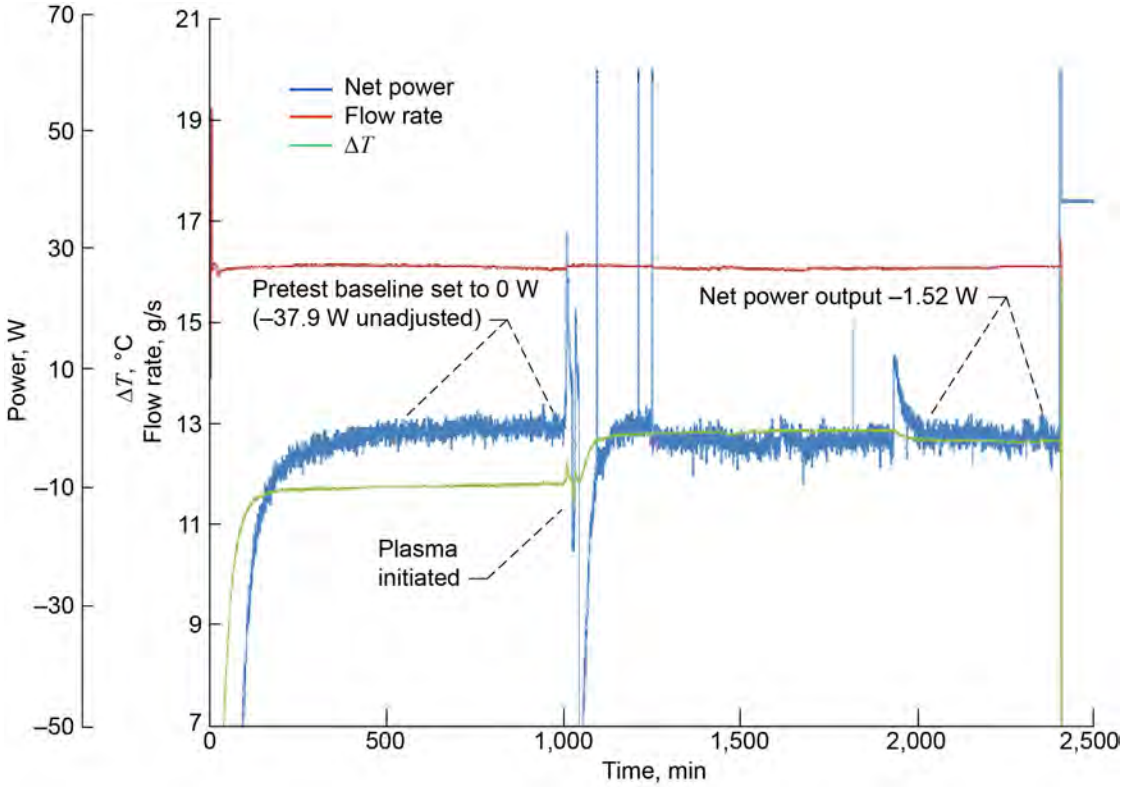

Figure 72.—Net output power based on anode current instantaneous power.

These results show that averaging the instantaneous power calculation for determining the plasma power supply input into the reactor is much more accurate then utilizing RMS current and voltage values. The instantaneous power averaging method can more accurately handle the large fluctuations in current seen during operation than the RMS power calculation method.

The net power is based on the heat output calculated from the calorimeter inlet and outlet temperatures and flow rate. Figure 73 shows the inlet and outlet temperatures of the water flowing through the water jacket surrounding the reactor and the temperature difference between these two values. The ΔT curve (outlet temperature minus inlet temperature) is a good indicator of heat input changes within the reactor. From the curve in Figure 73, it is evident when the plasma was ignited at approximately 1,000 min due to the abrupt rise in the ΔT. There was also a dropoff in ΔT at around 1,800 min. This is most likely due to a change in the plasma state within the reactor causing a decrease in the plasma power supply input power. The ΔT fluctuated approximately ±0.025 °C during the test.

Flow rate changes through the calorimeter can also affect the ΔT. If the flow rate speeds up, the ΔT will drop for a given heat input, or the opposite, if the flow rate slows down, the ΔT will increase. Therefore, looking just at the ΔT as an indicator of net power can be deceiving. Even the calculated net power output graph may not completely tell what is occurring since there is a time lag between when a parameter changes and it is fully registered by the calorimeter. Plotting the flow rate along with the ΔT, as shown in Figure 74, provides a good insight into the origin of net power changes.

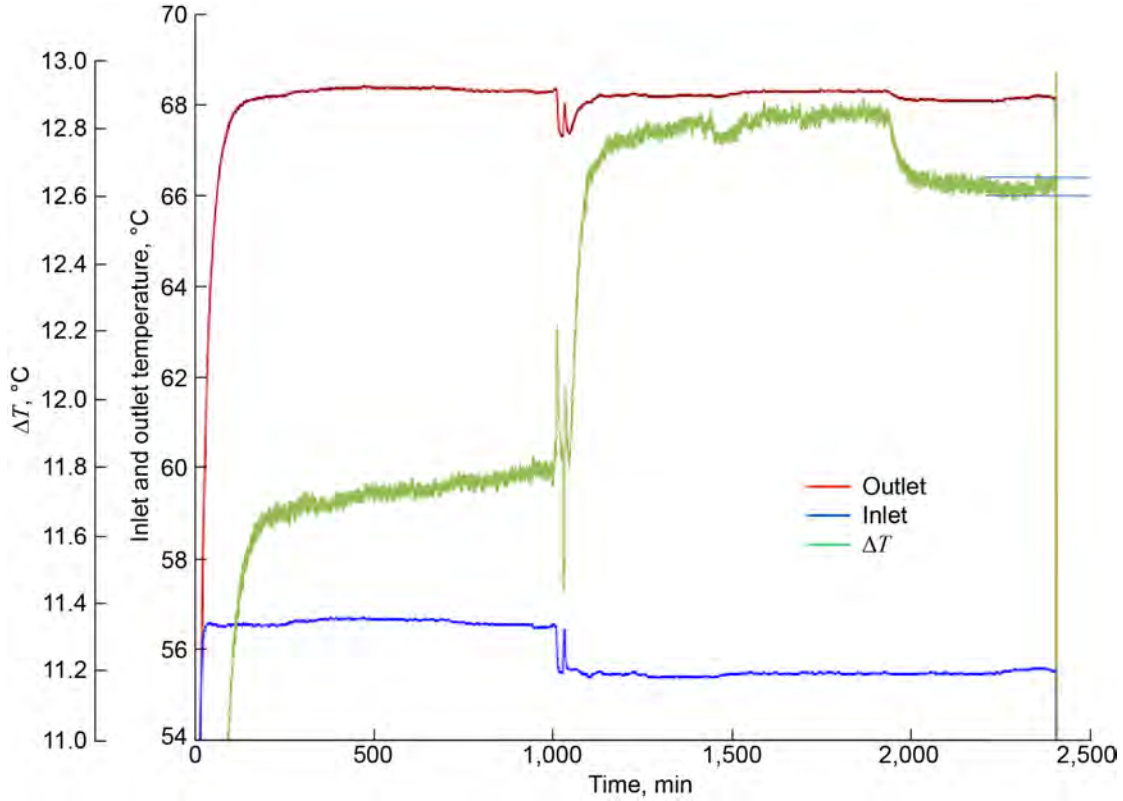

Figure 73.—Calorimeter change in temperature ΔT and inlet and outlet temperatures.

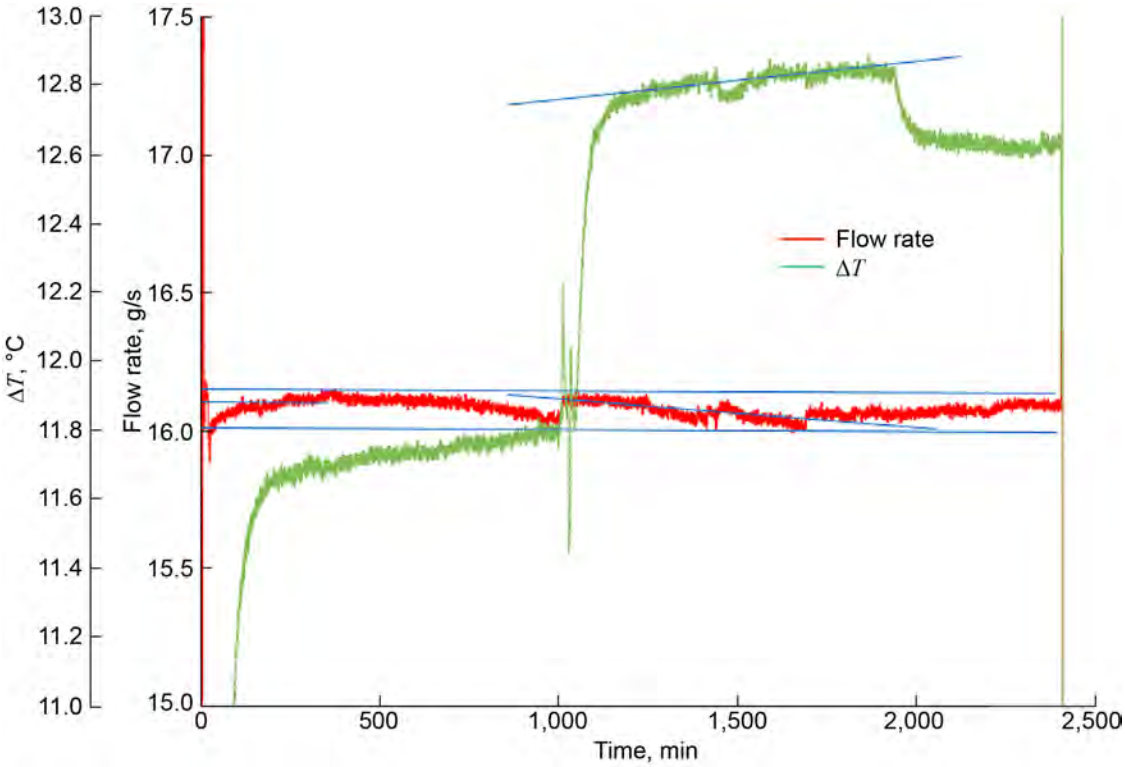

Figure 74.—The change in calorimeter temperature ΔT and flow rate.

The flow rate throughout the test was fairly stable. There were no significant jumps or changes. It varied approximately 0.2 g/s over the test period and fluctuated approximately ±0.025 g/s. In addition, it can be noted by looking at Figure 74 that there was no change in flow rate that corresponded to the drop in the ΔT that occurred around 1,800 min. This indicated that the drop in the ΔT was due to a decrease of power into the reactor from either the heaters or the plasma power source. Also, it can be noted that before this drop there was a steady slight increase in ΔT from about 1,200 to 1,800 min. However, over this time period there was also a slow decline in the flow rate. Therefore, the slow decline in flow rate was most likely the cause of the slow rise in the ΔT causing the net power to remain constant over this period of time as seen in Figure 71 and Figure 72.

The heaters and the plasma are the heat sources for the reactor. The data collected during the test can provide some insight into these sources. Figure 75 shows the RMS voltage and current throughout the test. Although, as shown in Figure 69 to Figure 72, using the RMS voltage and current does not provide as accurate of a net power output. It is still representative of the voltage and current levels seen throughout the test. The instantaneous average power based on the anode and cathode current is collected in the data file. However, only a small number of the total pulses are averaged. This is due to speed and data size limitations. The average voltage and current of a series of pulses is captured and recorded in the data file as a data point representing the instantaneous average of those values at that point in time. This process is repeated for each data point in the data file. For example, the oscilloscopes would capture and average the current and voltage for 15 pulses. The oscilloscopes were synced so that the measurements would take place at the same time. The averages of these 15 pulses would be multiplied together and the resultant instantaneous average plasma input power would be recorded in the data file. Once the data point was recorded, another 15-pulse sample would be taken and the process repeated.

The anode and cathode RMS current levels were fairly level throughout the test. The cathode RMS current fluctuated approximately ±0.025 A and the anode RMS current fluctuated approximately ±0.01 A during the test. The RMS anode voltage fluctuated approximately ±40 V during the test. The RMS cathode voltage was essentially 0 during the test, which should be expected since it was connected near ground potential.

From Figure 75, it can be seen that there was a drop in RMS voltage at the 1,800-min point of the test. This corresponds to the drop in the ΔT seen in Figure 73. This indicates that the drop in the ΔT was caused by a change in the plasma input power. The chamber voltage can drop if the internal resistance within the chamber decreases. This decrease in internal resistance can be caused by the reduction or elimination of a gap within the chamber that would normally require the formation of a plasma to bridge. If one of the spacer gaps shorted out because of deposited material or other effects, then the resistance within the chamber would drop causing a drop in the voltage across the chamber and thereby lowering the plasma power into the chamber. This reduction in internal resistance is also supported by the increase in both the anode and cathode current coincident with the anode voltage drop.

The other heat source for the reactor are the heaters. The heater blocks surround the reactor and are underneath the calorimeter water jacket. Each block contains two cartridge heaters that are operated in series. The heater blocks are wired in parallel. This arrangement provides a single current level for each heater block and a single operating voltage for all of the heater blocks combined. The heater voltage and current during the test is shown in Figure 76.

The heater voltage during the test was very stable and remained at a level near 158.5 V. The current into each of the heater blocks was also stable throughout the test with a slow drift downward. On the graph, fluctuations can be seen; however, the scale of the graph is small, 0.03 A over the full range. There were some spikes observed in the current. This is most likely due to electromagnetic (EM) noise on the signal line due to the generation of the plasma within the chamber.

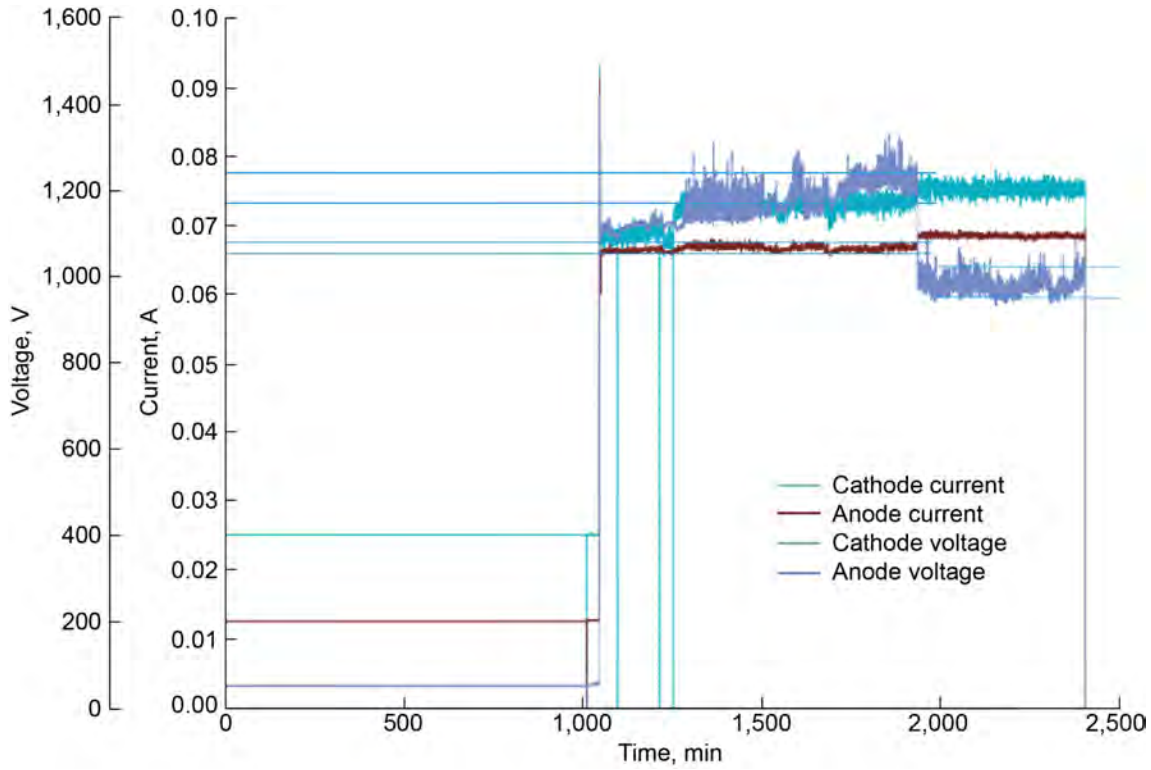

Figure 75.—Root-mean-square (RMS) voltage and current.

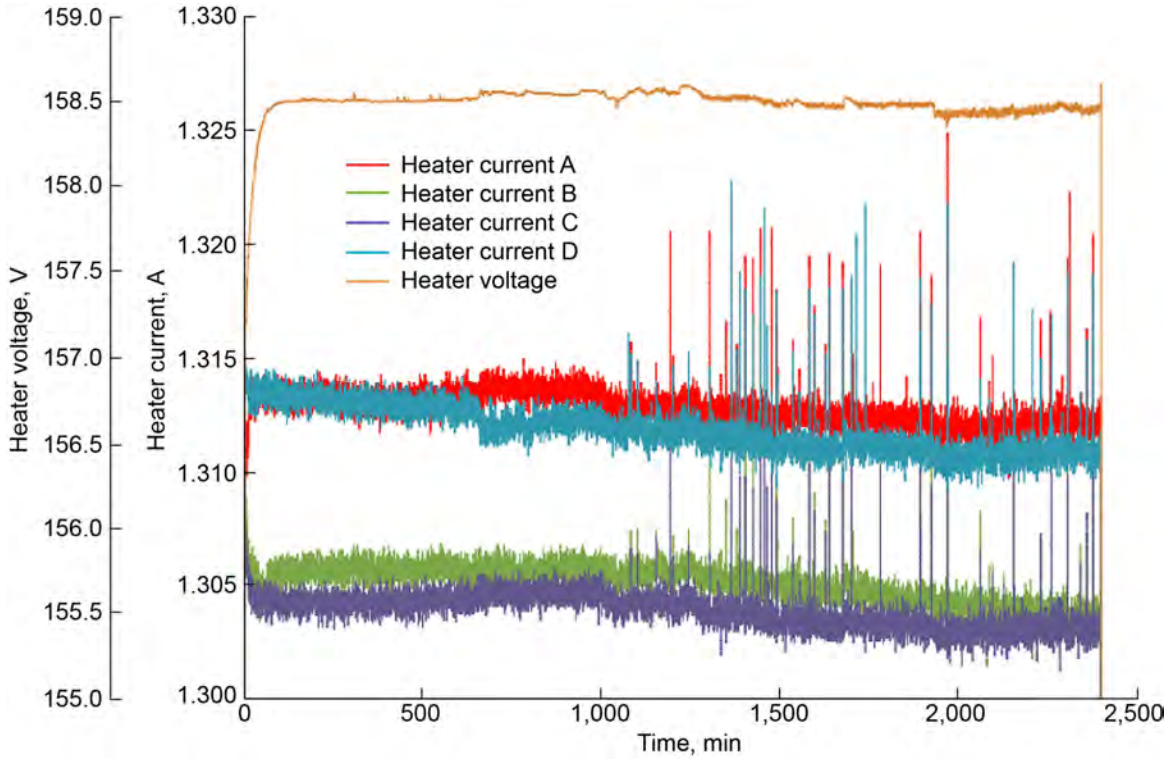

Figure 76.—Heater current and voltage.

The calorimeter output itself can also be examined to see what heat or power output it is registering during the test. If the calorimeter is showing a change in output, then heat is being added to the reactor. Figure 77 shows the calorimeter output minus the heater input power. The heater power is subtracted since it is an easily measurable known quantity. The calorimeter output shows that additional heat on the order of 5 W was being added from approximately 1,200 to 1,800 min. Then at 1,800 min there was a drop of approximately 15 W in the calorimeter output after which it was fairly stable.

These changes in the calorimeter output can be attributed to changes in the plasma power input. This can be seen on Figure 78, which shows the heater power, plasma power, and the net power over the course of the test. From this figure, it can be seen that the heater power dropped about 1.5 W over the course of the test from approximately 830 to 828.5 W.

The plasma input power can be seen to increase slightly, up to approximately 1,800 min, and then step down. This corresponds well to what was observed (Figure 77) for the calorimeter output power. The initial rise in plasma power up to 1,800 min is approximately 5 W, as observed in the calorimeter output. The stepdown in calorimeter output corresponds to the drop in the plasma power. These comparisons show that the calorimeter can accurately resolve small changes in input heat.

Heat losses to the surroundings can also play a role in measuring the reactor output power with the calorimeter. The initial steady state that is achieved, prior to the plasma being initiated, establishes a measure of the baseline heat loss to the surroundings for a test. Adjusting the net power to 0 for this baseline period effectively cancels out the environmental heat loss. However, to ensure that the heat loss to the surroundings is constant during the test, data is collected on the room temperature as well as the surface insulation temperature at a number of locations. This data is shown in Figure 79. If the difference between the room temperature and the insulation surface temperature remains constant during the test, then the heat loss to the surroundings through the insulation also remains constant.

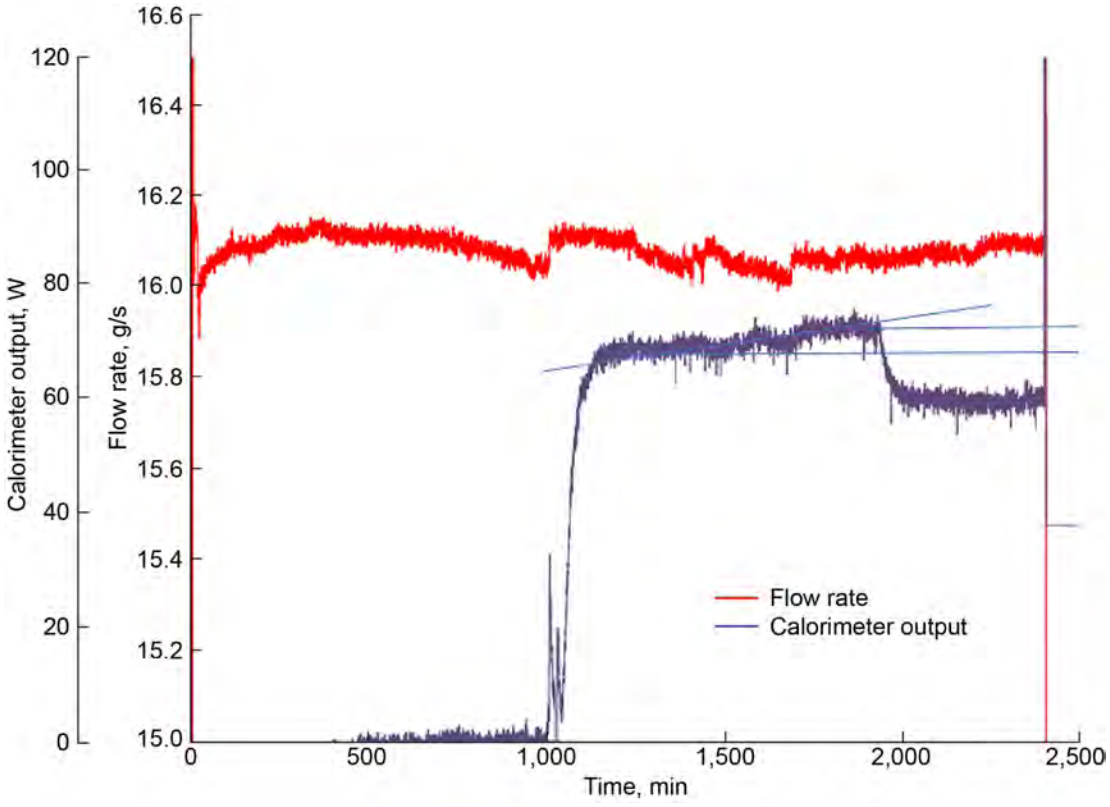

Figure 77.—Calorimeter output minus heater input and flow rate.

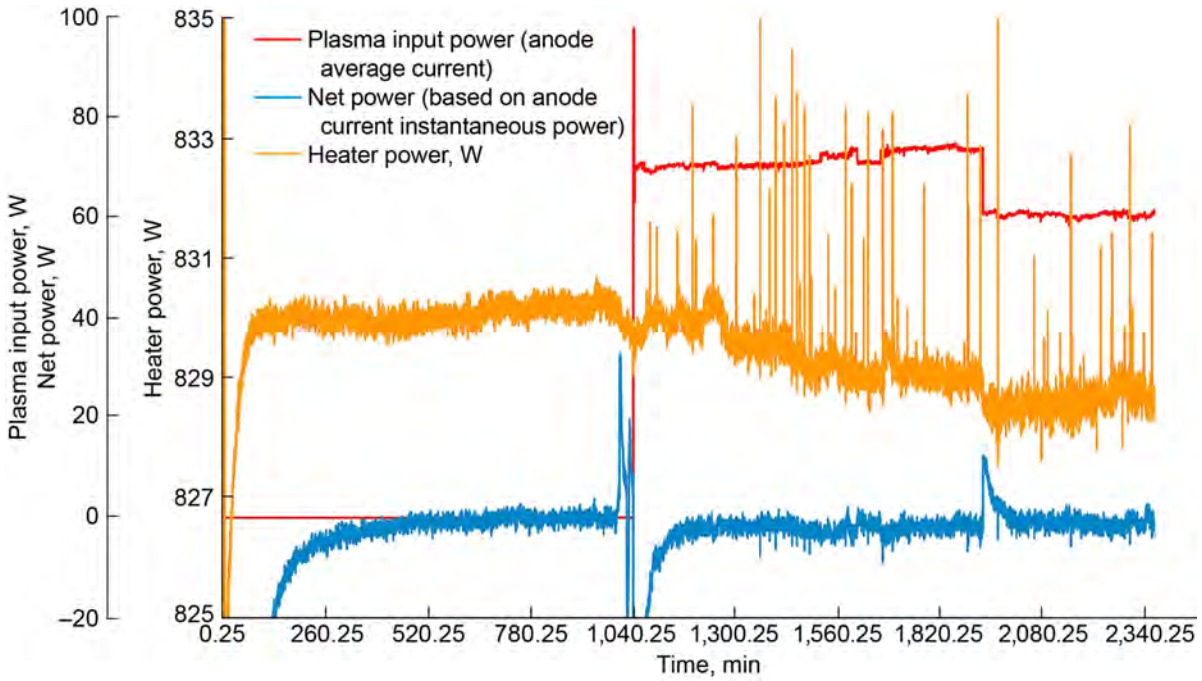

Figure 78.—Heater, plasma, and net powers.

The temperature data, in Figure 79, shows that the insulation surface temperature tracks the room ambient temperature throughout the test. Therefore, the heat loss through the insulation will be constant as the temperature difference between the insulation and room remains constant during the test. Monitoring these temperatures assists in determining the baseline heat loss to the room during the test period. In addition to affecting the heat loss to the surroundings, the room temperature can also affect the measurement accuracy of some of the electrical equipment used during the testing. These accuracy changes can be subtle but added up over a number of different test and data collection components. The change in measurement accuracy can factor into the test data. Therefore, to minimize these effects, the room temperature was held to within fluctuations of no more than 2 degrees during a test.

The internal chamber pressure is collected to ensure that the desired pressure was maintained within the chamber. The chamber pressure affects the plasma breakdown voltage and, therefore, internal resistance within the chamber. The lower the pressure, the lower the internal resistance will be until the bottom of the Paschen curve for the gas is reached, as shown in Figure 2. If the pressure within the chamber is decreased, then the plasma power will decrease. This test was run at a constant pressure of 500 torr as shown in Figure 80. This pressure was held constant throughout the test. The fluctuations seen prior to the plasma being ignited were due to the chamber being purged and filled to provide a pretest gas sample as well as to ensure clean gas for the test.

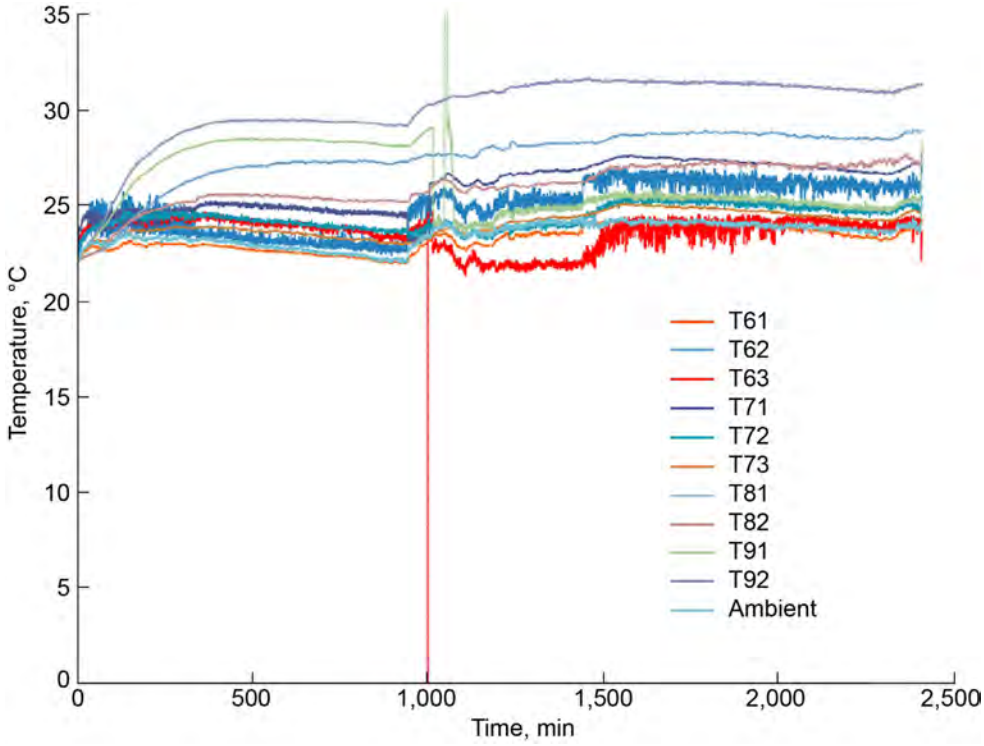

Figure 79.—Reactor insulation surface and ambient room temperature.

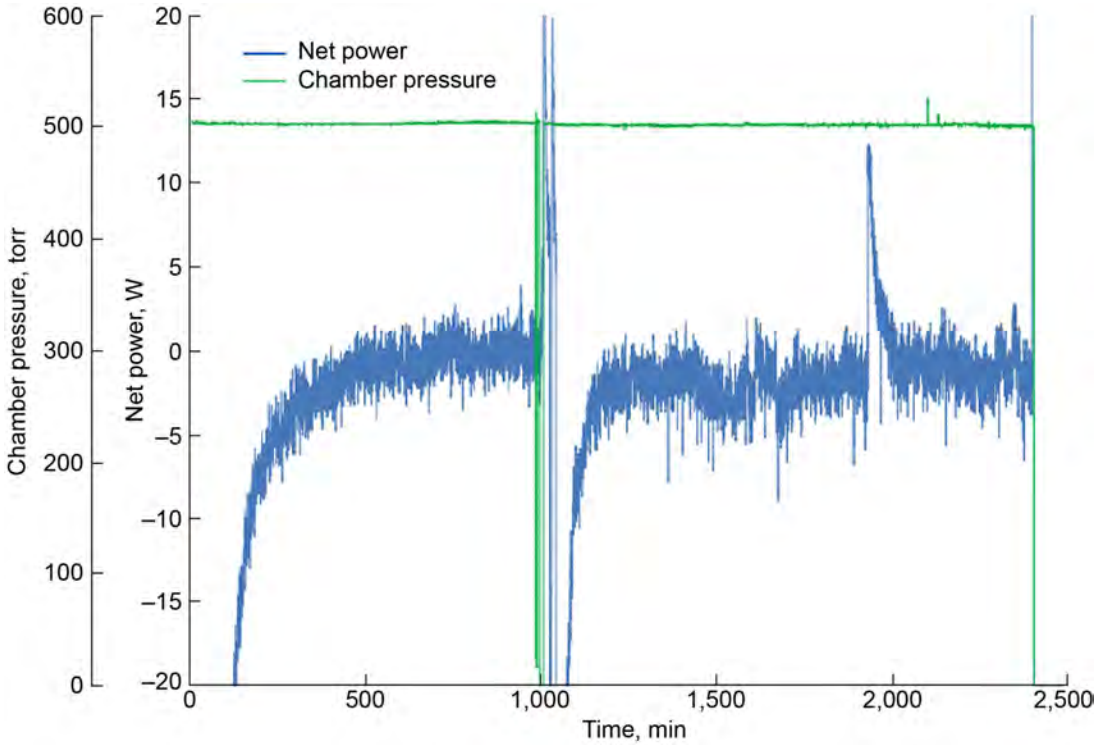

Figure 80.—Reactor chamber pressure and net power from anode current instantaneous power.

11.0 Concluding Remarks

A plasma reactor test system was designed, constructed, and tested. The purpose of the reactor is to expose materials to a pulsed plasma environment while contained within a controlled temperature and gas environment. The reactor was designed to be flexible and accommodate a number of test conditions and test samples. It was capable of heating the plasma chamber up to a maximum temperature of approximately 350 °C and supplying a variety of different gases to the chamber at a selectable pressure from vacuum levels to 200 psi. The calorimeter that was constructed around the plasma chamber is used to accurately monitor the thermal power exiting the plasma chamber. The measurement uncertainty analysis indicated the plasma reactor system is able to measure the total power inputted and produced within the reactor to ±7.6 W with a 95 percent probability. The chamber is designed flexibly so that the plasma column runs either directly between the two electrodes or was forced to run through porous beds of metal foam disks with or without powders pre-impregnated therein. Both a steady state or pulsed plasma could be generated.

There were a number of sensors and instrumentation incorporated in the test system to measure and monitor a various parameter related to the operation of the test stand and the test materials.

- Thermocouples were used to monitor the temperature at a number of locations on the reactor, calorimeter, and insulation.
- The calorimeter utilized resistance temperature detectors (RTDs) and high precision flowmeters to determine the total heat being removed from the reactor chamber.
- To monitor the gas within the chamber during operation, a residual gas analyzer (RGA) was used. Gas could be bled from the chamber and sent to the RGA for real-time analysis. This capability enabled the gas to be actively sampled and any change to its composition could be determined.
- To monitor and control the heater output, voltage and current measurements were made of the power being applied to the heaters.
- The plasma power input to the chamber was the most difficult parameter to measure of the reactor system. This measurement was done by monitoring the input and output voltage and current from the plasma electrodes and utilizing an oscilloscope-based monitoring system to determine the average pulse power electrode input to the reactor.

To further develop the plasma input power determination, the following items have been identified:

1. The National Instruments™ CompactRIO (cRIO) system clock must be in sync with the rest of the lab computers. The clocks should not be out of sync more than a few seconds. Anything more than this renders comparison between the high time resolution system and the National Instruments™ LabVIEW systems difficult at best.
2. In order to improve sampling of the underlying distribution of pulse power, one method of reducing scope repetition rate is to move from two Tektronix® scopes to one. The original system design called for five channels of data acquisition on the scopes, hence the two scopes. We are currently using only three channels, which one scope can support. Communicating with only one scope as compared to two should reduce transfer times.
3. If the impact in operational speed is not too large, we should utilize the high-resolution acquisition mode on the Tektronix® scope. This would reduce uncertainty in measuring lower current and voltage levels. In the current setup, it was deemed to add too much in communications overhead (twice as much data must be transmitted), but moving to one scope could make this a viable option again.

4. Think about dropping down to one pulse instead of four. If we can justify 1 pulse at 100,000 samples, and can read that significantly faster than 4 pulses at 1,000,000 samples, we could obtain a more random statistical sampling of the data. The high-resolution scope data suggests that a better statistical sampling is called for. A simple investigation of timing with the different configurations would show which solution is optimal.

To determine the output power from the calorimeter and compare it to the input power, the heater and electrode input power was monitored. Output electrical power for creating the plasma was monitored and the current and voltage waveforms were observed and recorded using a series of oscilloscopes. The results showed the accuracy of measuring the plasma input power and of the calorimeter in measuring the total heat output of the system. It was determined that the system had a total power measurement accuracy of ±1.36 percent.

The test samples utilized for the testing consisted of a nickel metal foam. A metal foam can be filled with metal powder. This combination provides an extremely high material surface area and provides a good method for investigating material-gas-plasma interactions.

The test stand also has the capability to collect the gas from the reactor chamber once a test is completed. This gas can be used for further analysis as needed.

A checkout test of the system was performed, which had a 16-h heatup time to reach pretest equilibrium within the reactor and a 24-h plasma operation time. The collected data was analyzed using different methods to determine the analysis that provided the lowest error in estimating the total power output of the reactor. The first method utilized the root mean square (RMS) cathode current to calculate the plasma power. The net power (input to output) from the reactor using this method produced –14.3 W. The next method used RMS anode current and produced a net power difference of –7.7 W. The next two methods used the cathode and anode instantaneous power. These produced net power differences of –1.06 and –1.52 W, respectively. This evaluation showed that the instantaneous power was the most accurate method for measuring the plasma power and, of these, using the cathode current instantaneous power provided a slight benefit over using the anode current instantaneous power.

Overall, the plasma chamber and calorimeter functioned as designed and performed well. The system has a number of capabilities for determining the power into and out of the reactor as well as providing a means of analyzing the gas within the chamber both during the testing as well as enabling posttest analysis.

Appendix A.—Sensor and Data Collection

Figure A.1 to Figure A.4 display the piping and instrumentation diagrams (P&IDs).

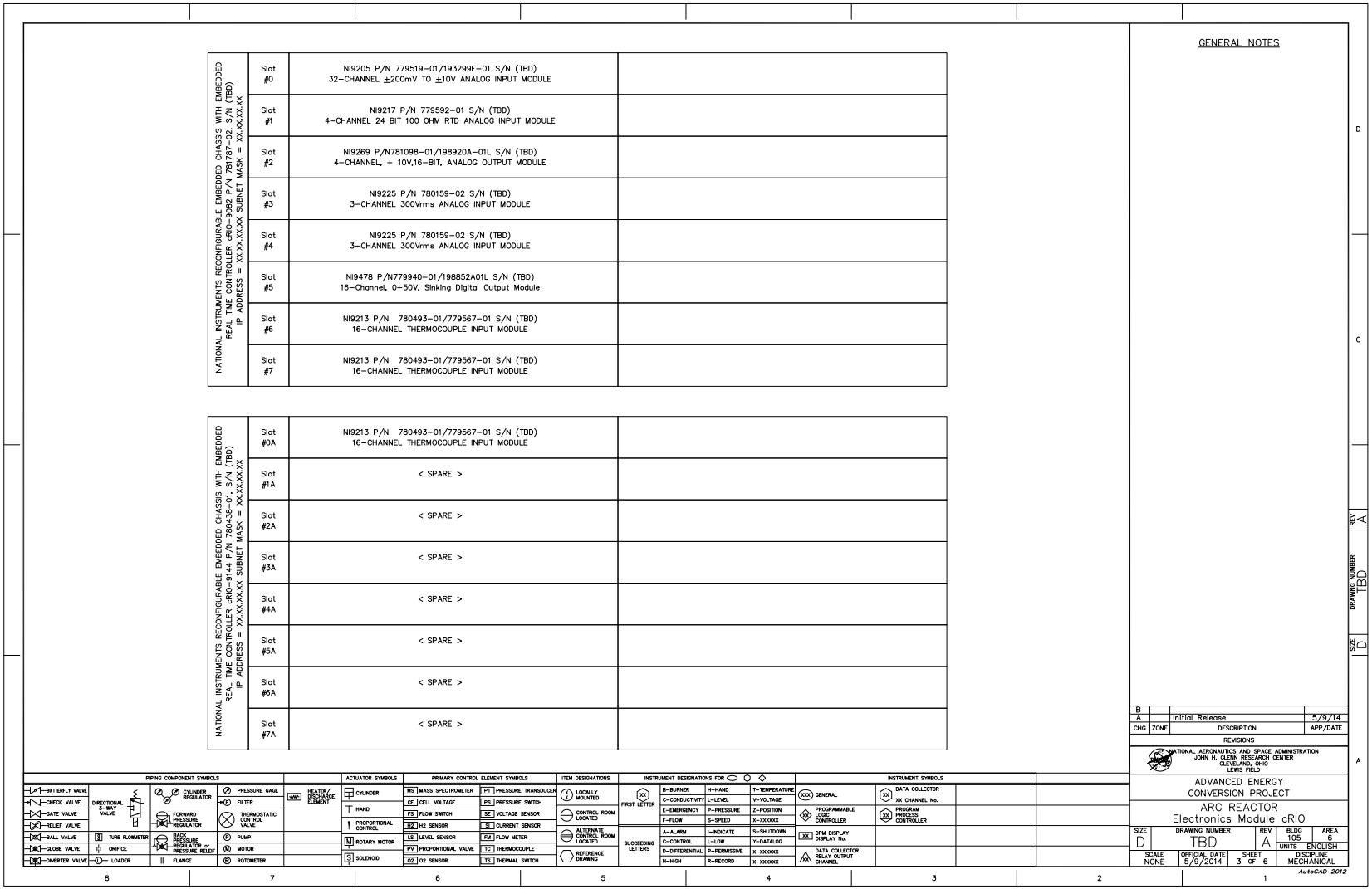

Figure A.1.—National Instruments™ CompactRIO (cRIO) data collection slot layout.

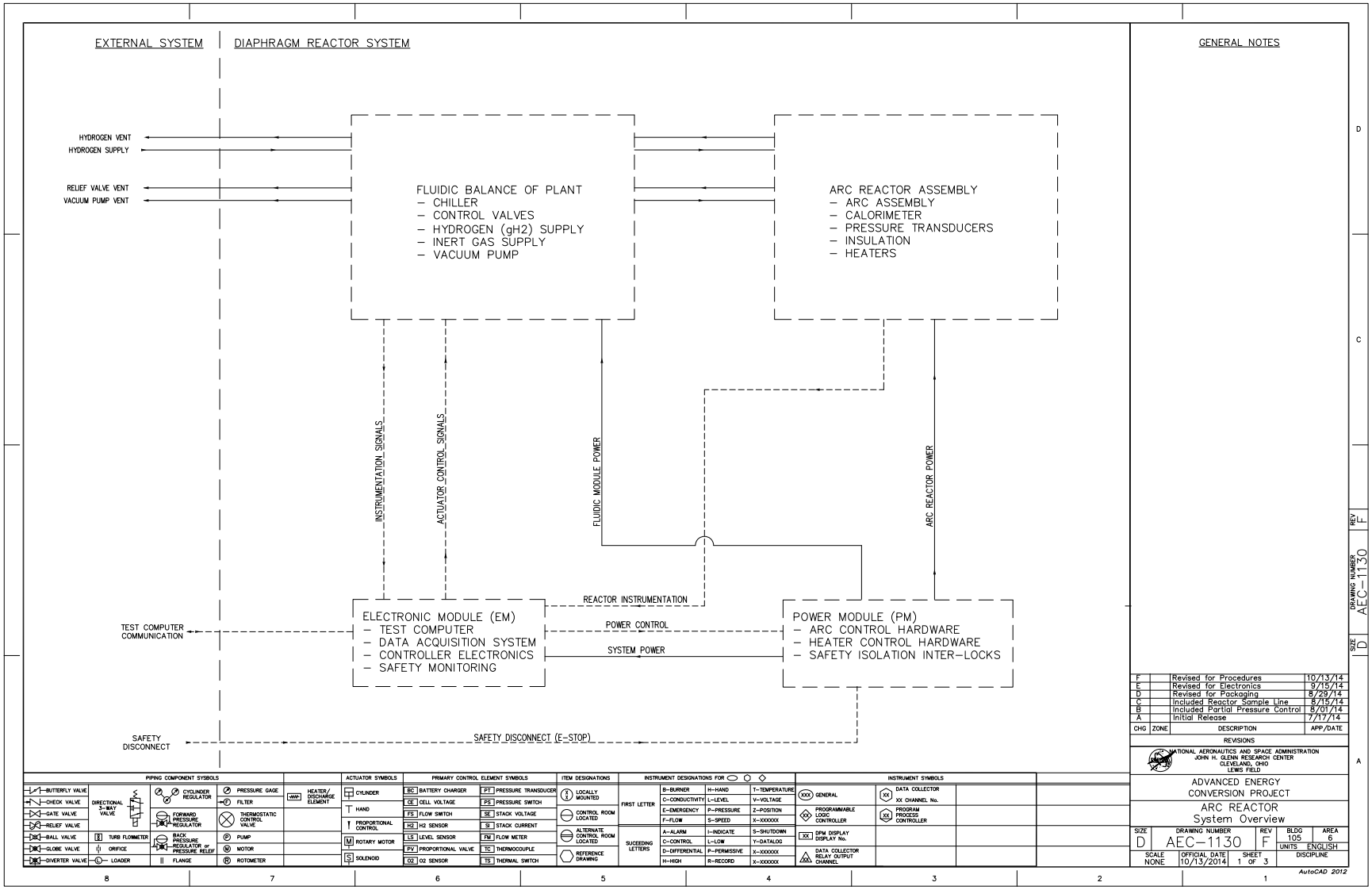

Figure A.2.—Overall piping and instrumentation diagram (P&ID) system layout.

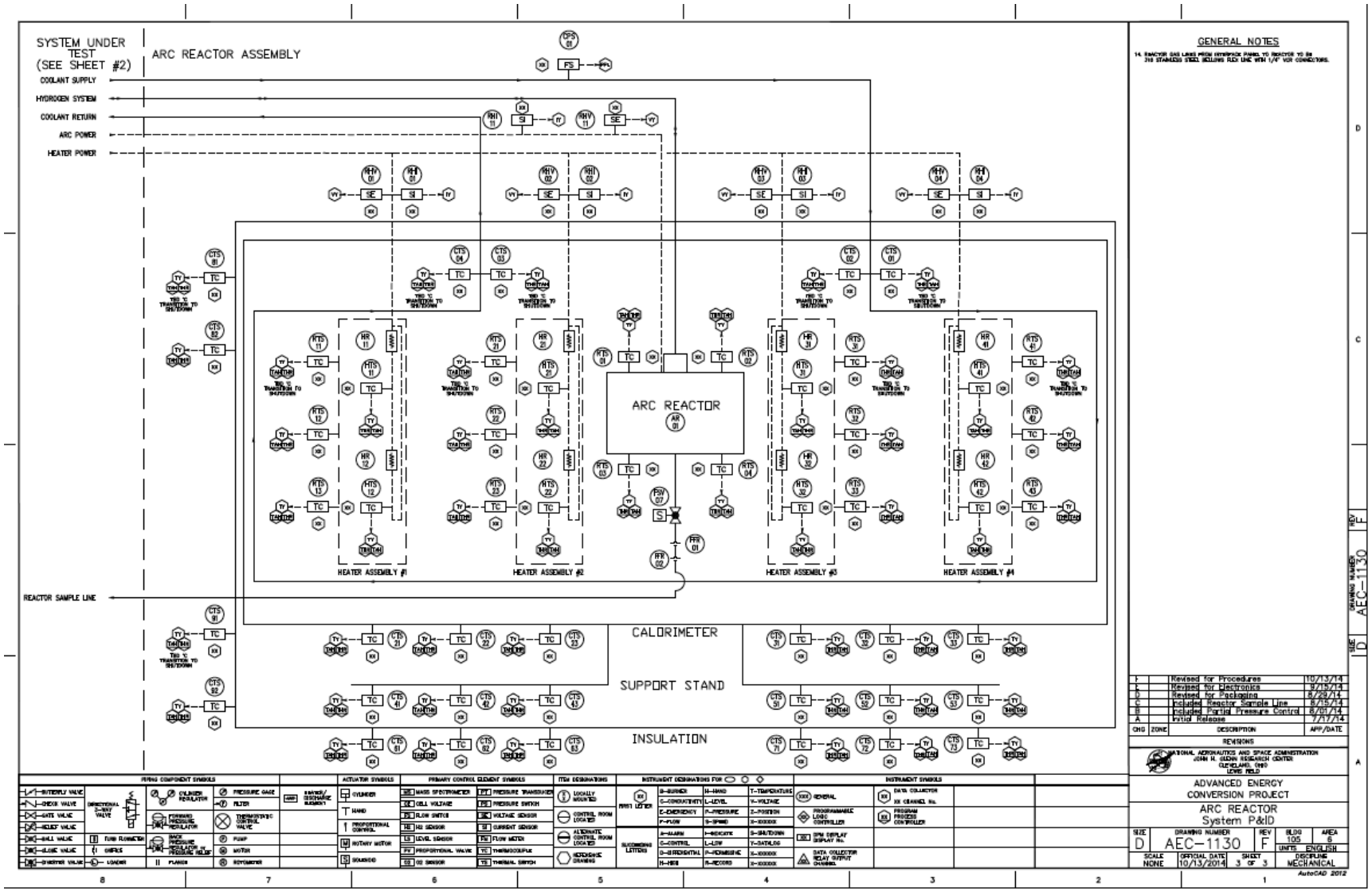

Figure A.3.—Temperature measurement piping and instrumentation diagram (P&ID).

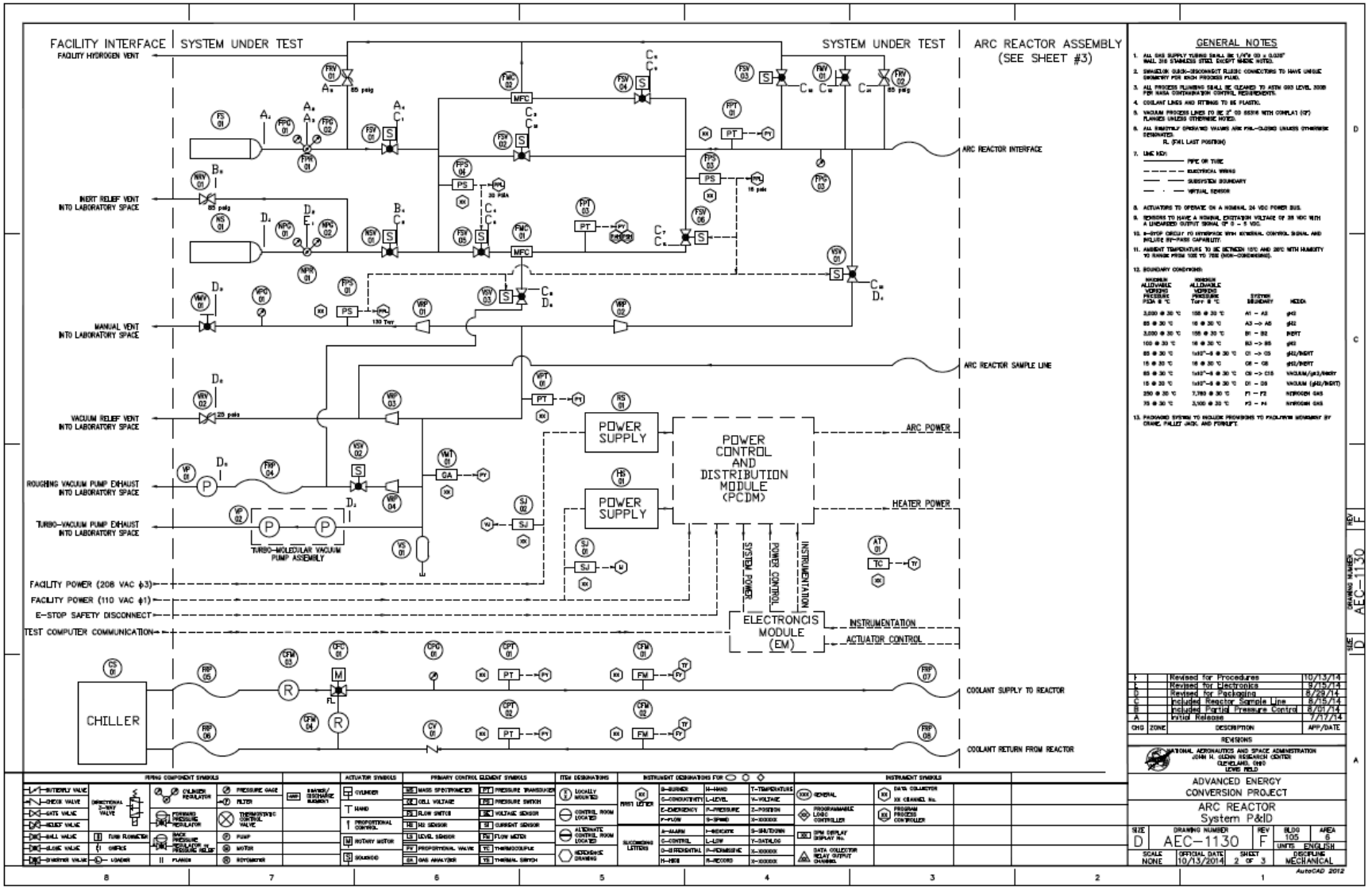

Figure A.4.—Fluid layout piping and instrumentation diagram (P&ID).

Appendix B.—Electronic Component List and Specifications

Table B.1 and Table B.2 contain a list of the electronic components and their specifications.

TABLE B.1.—COMPONENT LIST

[Reference Figure A.3 and Figure A.4 for piping and instrumentation diagram (P&ID).]

Item	P&ID identifier	Parameter	Sensor/actuator type	Part number	Model number	Manufacturer
Current						
C1	RHI01	Heater block #1 current	CompactRIO (cRIO) module - calibrated resistor	781099-01/ TB196375-01	NI–9227	National Instruments™
C2	RHI02	Heater block #2 current	cRIO module - calibrated resistor	781099-01/TB196375-01	NI–9227	National Instruments™
C3	RHI03	Heater block #3 current	cRIO module - calibrated resistor	781099-01/TB196375-01	NI–9227	National Instruments™
C4	RHI04	Heater block #4 current	cRIO module - calibrated resistor	781099-01/TB196375-01	NI–9227	National Instruments™
C5	RHI11	Arc current	0.1 V/A BNC terminal	NA	110	Pearson Electronics
Heater						
H1	HR11	Reactor heater block #1A	Resistive heating element	J6A–15311	Cartridge	Watlow®
H2	HR12	Reactor heater block #1B	Resistive heating element	J6A–15311	Cartridge	Watlow®
H3	HR21	Reactor heater block #2A	Resistive heating element	J6A–15311	Cartridge	Watlow®
H4	HR22	Reactor heater block #2B	Resistive heating element	J6A–15311	Cartridge	Watlow®
H5	HR31	Reactor heater block #3A	Resistive heating element	J6A–15311	Cartridge	Watlow®
H6	HR32	Reactor heater block #3B	Resistive heating element	J6A–15311	Cartridge	Watlow®
H7	HR41	Reactor heater block #4A	Resistive heating element	J6A–15311	Cartridge	Watlow®
H8	HR42	Reactor heater block #4B	Resistive heating element	J6A–15311	Cartridge	Watlow®
H9	HS01-1	Reactor heater power supply	Actuator, power, proportional	DLM300-10E	DLM300	Sorensen
H10	RS01-1	Plasma reactor power supply	Actuator, power, proportional	AMP–10B40	AMP–10B40	Matsusada Precision
Mass flow rate						
Q1	CFM01	Coolant supply flowmeter	Turbine	FTO–4AIYWBLHCT5 with LAT–3–C0–V2B6	FTO	FTI Flow Technologies™
Q2	CFM02	Coolant return flowmeter	Turbine	FTO–4AIYWBLHCT5 with LAT–3–C0–V2B6	FTO	FTI Flow Technologies™
Q3	FMC01	Partial pressure control valve output	Actuator, flow, automated	PCD–30PSIA-D-PCV10,5P,5IN	PCD	Alicat Scientific
Q4	FMC01-1	Partial pressure control valve set point	Actuator, flow, automated	PCD–30PSIA–D–PCV10,5P,5IN	PCD	Alicat Scientific
Q5	FMC02	Pressure control valve output	Actuator, flow, automated	PCD–100PSIA–D,5P,5IN	PCD	Alicat Scientific

TABLE B.1.—COMPONENT LIST

[Reference Figure A.3 and Figure A.4 for piping and instrumentation diagram (P&ID).]

Item	P&ID identifier	Parameter	Sensor/actuator type	Part number	Model number	Manufacturer
Q6	FMC02-1	Pressure control valve set point	Actuator, flow, automated	PCD–100PSIA–D,5P,5IN	PCD	Alicat Scientific
Power						
J1	SJ01	Facility power 120 Vac	Power transducer	APS–1–420–24L–5	APS	NK Technologies
J2	SJ02	Facility power 208 Vac	Power transducer	APS–2–420–24L–1	APS	NK Technologies
Pressure						
P1	FPT01	Hydrogen line pressure	Diaphragm/strain gage	225G-Z01P-A-D4-2B-B1	225	Setra®
P2	FPT02	Reactor internal pressure	Diaphragm/strain gage	225G-Z01P-A-D4-2B-B1	225	Setra®
P3	VPT01	Vacuum line pressure	Pirani and cold cathode	PKR 251, PT R26 002	D–35614 Assiar	Pfeiffer Vacuum
P4	CPT01	Coolant flowmeter supply pressure	Diaphragm/strain gage	225G-Z01P-A-D4-2B-B1	225	Setra®
P5	CPT02	Coolant flowmeter return pressure	Diaphragm/strain gage	225G-Z01P-A-D4-2B-B1	225	Setra®
P6	FPT03	Reactor vacuum pressure	Pirani and cold cathode	PKR 251, PT R26 002	D–35614 Assiar	Pfeiffer Vacuum
P7	FPS01	Vacuum switch	Single pole double throw (SPDT) switch	PSW–696–N5	PSW–690	Omega™
P8	FPS03	Partial pressure control isolation valve-downstream switch	SPDT switch	PSW–633	PSW–630	Omega™
P9	FPS04	Partial pressure control isolation valve-upstream switch	SPDT switch	PSW–633	PSW–630	Omega™
P10		Low pressure gauge	Variable-capacitance sensor	Type 122A	Type 122A	MKS Instruments, Baratron®
Temperature						
T1	AT01	Ambient temperature	“T” type thermocouple	TMQSS–062U–6 or equivalent P/N	KMQSS	Omega™
T2	CTS01	Calorimeter coolant inlet temperature	Resistance temperature detector (RTD)	P–M–1/10–1/8–6–0–TS–3	P-M	Omega™
T3	CTS02	Calorimeter coolant inlet temperature	RTD	P–M–1/10–1/8–6–0–TS–3	P-M	Omega™
T4	CTS03	Calorimeter coolant outlet temperature	RTD	P–M–1/10–1/8–6–0–TS–3	P-M	Omega™
T5	CTS04	Calorimeter coolant outlet temperature	RTD	P–M–1/10–1/8–6–0–TS–3	P-M	Omega™
T6	---	---	---	---	---	---
T7	---	---	---	---	---	---
T8	CTS21	Calorimeter surface - side a, forward	“T” type thermocouple	SA1–T–SC	SA1	Omega™
T9	CTS22	Calorimeter surface - side a, mid	“T” type thermocouple	SA1–T–SC	SA1	Omega™
T10	CTS23	Calorimeter surface - side a, aft	“T” type thermocouple	SA1–T–SC	SA1	Omega™
T11	CTS31	Calorimeter surface - side b, forward	“T” type thermocouple	SA1–T–SC	SA1	Omega™
T12	CTS32	Calorimeter surface - side b, mid	“T” type thermocouple	SA1–T–SC	SA1	Omega™

TABLE B.1.—COMPONENT LIST

[Reference Figure A.3 and Figure A.4 for piping and instrumentation diagram (P&ID).]

Item	P&ID identifier	Parameter	Sensor/actuator type	Part number	Model number	Manufacturer
T13	CTS33	Calorimeter surface - side b, aft	“T” type thermocouple	SA1–T–SC	SA1	Omega™
T14	CTS41	Support stand - forward leg, high	“T” type thermocouple	SA1–T–SC	SA1	Omega™
T15	CTS42	Support stand - forward leg, mid	“T” type thermocouple	SA1–T–SC	SA1	Omega™
T16	CTS43	Support stand - forward leg, low	“T” type thermocouple	SA1–T–SC	SA1	Omega™
T17	CTS51	Support stand - aft leg, high	“T” type thermocouple	SA1–T–SC	SA1	Omega™
T18	CTS52	Support stand - aft leg, mid	“T” type thermocouple	SA1–T–SC	SA1	Omega™
T19	CTS53	Support stand - aft leg, low	“T” type thermocouple	SA1–T–SC	SA1	Omega™
T20	CTS61	Insulation surface -side a, forward	“T” type thermocouple	SA1–T–SC	SA1	Omega™
T21	CTS62	Insulation surface -side a, mid	“T” type thermocouple	SA1–T–SC	SA1	Omega™
T22	CTS63	Insulation surface - side a, aft	“T” type thermocouple	SA1–T–SC	SA1	Omega™
T23	CTS71	Insulation surface - side b, forward	“T” type thermocouple	SA1–T–SC	SA1	Omega™
T24	CTS72	Insulation surface - side b, mid	“T” type thermocouple	SA1–T–SC	SA1	Omega™
T25	CTS73	Insulation surface - side b, aft	“T” type thermocouple	SA1–T–SC	SA1	Omega™
T26	CTS81	Insulation surface - forward face, high	“T” type thermocouple	SA1–T–SC	SA1	Omega™
T27	CTS82	Insulation surface - forward face, low	“T” type thermocouple	SA1–T–SC	SA1	Omega™
T28	CTS91	Insulation surface - aft face, high	“T” type thermocouple	SA1–T–SC	SA1	Omega™
T29	CTS92	Insulation surface - aft face, low	“T” type thermocouple	SA1–T–SC	SA1	Omega™
T30	RTS01	Arc reactor surface - forward face, high	“K” type thermocouple	EI1106107–XCIB–K–4–5–3	XCIB	Omega™
T31	RTS02	Arc reactor surface - forward face, low	“K” type thermocouple	EI1106107–XCIB–K–4–5–4	XCIB	Omega™
T32	RTS03	Arc reactor surface - aft face, high	“K” type thermocouple	EI1106107–XCIB–K–4–5–5	XCIB	Omega™
T33	RTS04	Arc reactor surface - aft face, low	“K” type thermocouple	EI1106107–XCIB–K–4–5–6	XCIB	Omega™
T34	RTS11	Heater block 1-2 assembly temperature, forward	“K” type thermocouple	EI1106107–XCIB–K–4–5–7	XCIB	Omega™
T35	RTS12	Heater block 1-2 assembly temperature, mid	“K” type thermocouple	EI1106107–XCIB–K–4–5–8	XCIB	Omega™
T36	RTS13	Heater block 1-2 assembly temperature, aft	“K” type thermocouple	EI1106107–XCIB–K–4–5–9	XCIB	Omega™

TABLE B.1.—COMPONENT LIST

[Reference Figure A.3 and Figure A.4 for piping and instrumentation diagram (P&ID).]

Item	P&ID identifier	Parameter	Sensor/actuator type	Part number	Model number	Manufacturer
T37	RTS21	Heater block 2-3 assembly temperature, forward	“K” type thermocouple	EI1106107–XCIB–K–4–5–10	XCIB	Omega™
T38	RTS22	Heater block 2-3 assembly temperature, mid	“K” type thermocouple	EI1106107–XCIB–K–4–5–11	XCIB	Omega™
T39	RTS23	Heater block 2-3 assembly temperature, aft	“K” type thermocouple	EI1106107–XCIB–K–4–5–12	XCIB	Omega™
T40	RTS31	Heater block 3-4 assembly temperature, forward	“K” type thermocouple	EI1106107–XCIB–K–4–5–13	XCIB	Omega™
T41	RTS32	Heater block 3-4 assembly temperature, mid	“K” type thermocouple	EI1106107–XCIB–K–4–5–14	XCIB	Omega™
T42	RTS33	Heater block 3-4 assembly temperature, aft	“K” type thermocouple	EI1106107–XCIB–K–4–5–15	XCIB	Omega™
T43	RTS41	Heater block 4-1 assembly temperature, forward	“K” type thermocouple	EI1106107–XCIB–K–4–5–16	XCIB	Omega™
T44	RTS42	Heater block 4-1 assembly temperature, mid	“K” type thermocouple	EI1106107–XCIB–K–4–5–17	XCIB	Omega™
T45	RTS43	Heater block 4-1 assembly temperature, aft	“K” type thermocouple	EI1106107–XCIB–K–4–5-18	XCIB	Omega™
T46	HTS11	Heater #1a heater temperature	“K” type thermocouple	J6A–15311	Style B	Watlow®
T47	HTS12	Heater #1b heater temperature	“K” type thermocouple	J6A–15311	Style B	Watlow®
T48	HTS21	Heater #2a heater temperature	“K” type thermocouple	J6A–15311	Style B	Watlow®
T49	HTS22	Heater #2b heater temperature	“K” type thermocouple	J6A–15311	Style B	Watlow®
T50	HTS31	Heater #3a heater temperature	“K” type thermocouple	J6A–15311	Style B	Watlow®
T51	HTS32	Heater #3b heater temperature	“K” type thermocouple	J6A–15311	Style B	Watlow®
T52	HTS41	Heater #4a heater temperature	“K” type thermocouple	J6A–15311	Style B	Watlow®
T53	HTS42	Heater #4b heater temperature	“K” type thermocouple	J6A–15311	Style B	Watlow®
Voltage						
V1	RHV11	Arc voltage	BNC terminal	P6015A	P6015A	Tektronix®
V2	RHV01	Heater block #1 voltage	Heater voltage	780159–01	NI–9225	National Instruments™
V3	RHV02	Heater block #2 voltage	Heater voltage	780159–01	NI–9225	National Instruments™
V4	RHV03	Heater block #3 voltage	Heater voltage	780159–01	NI–9225	National Instruments™
V5	RHV04	Heater block #4 voltage	Heater voltage	780159–01	NI–9225	National Instruments™

TABLE B.1.—COMPONENT LIST

[Reference Figure A.3 and Figure A.4 for piping and instrumentation diagram (P&ID).]

Item	P&ID identifier	Parameter	Sensor/actuator type	Part number	Model number	Manufacturer
Pump						
A6	---------	----------	----------	----------	----------	----------
A7	VP02	Turbomolecular pump assembly	Vacuum pump	PM015887–T	015 887–T/ S03 556A	Pfeiffer Vacuum
Valve, diverter						
A8	CFC01	Coolant diverter valve	3–way continuous valve	D4466TSEV1	D Series	Flowserve® Worcester Control
A8	CFC01-1	Coolant diverter valve - motor controller	Actuator, flow, proportional	10754W24D/AF17–5V	75 Series	Flowserve® Worcester Control
Valve, solenoid						
A1	FSV01	Hydrogen supply isolation solenoid valve	2–way, normally closed (N.C.)	A2011–4M–SB5–V–VO–24VDC–OC	A Series	Gems™ Sensors and Controls
A2	FSV02	Reactor isolation solenoid valve	2–way, N.C.	A2011–4M–SB5–V–VO–24VDC–OC	A Series	Gems™ Sensors and Controls
A3	FSV03	Hydrogen vent solenoid	2–way, N.C.	A2011–4M–SB5–V–VO–24VDC–OC	A Series	Gems™ Sensors and Controls
A4	FSV04	Reactor assembly isolation solenoid valve	2–way, N.C.	A2011–4M–SB5–V–VO–24VDC–OC	A Series	Gems™ Sensors and Controls
A11	FSV05	Partial pressure control isolation valve - upstream	2–way, N.C.	A2011–4M–SB5–V–VO–24VDC–OC	A Series	Gems™ Sensors and Controls
A12	FSV06	Partial pressure control isolation valve - downstream	2–way, N.C.	A2011–4M–SB5–V–VO–24VDC–OC	A Series	Gems™ Sensors and Controls
A13	FSV07	Transducer protection valve	2–way, N.C.	A2011–4M–SB5–V–VO–24VDC–OC	A Series	Gems™ Sensors and Controls
A5	VSV01	Reactor evacuation solenoid valve	2–way, N.C.	A2011–4M–SB5–V–VO–24VDC–OC	A Series	Gems™ Sensors and Controls
A9	NSV01	Inert gas supply solenoid valve	2–way, N.C.	A2011–4M–SB5–V–VO–24VDC–OC	A Series	Gems™ Sensors and Controls
A10	VSV02	Roughing pump isolation valve	2–way, N.C.	A2011–4M–SB5–V–VO–24VDC–OC	A Series	Gems™ Sensors and Controls
A14	VSV03	Partial pressure controller isolation valve	2–way, N.C.	A2011–4M–SB5–V–VO–24VDC–OC	A Series	Gems™ Sensors and Controls

TABLE B.2.—COMPONENT SPECIFICATIONS

[Reference Figure A.3 and Figure A.4 for piping and instrumentation diagram (P&ID).]

Item	P&ID identifier	Display range, nom (cal)	Signal out, nom (cal) for range	Excitation or power	Electrical interface	Mechanical interface
Current						
C1	RHI01	0.00 to 5.00	0.00 to 5.00 A	N/A	Screw terminal	Strain relief NI–9971 (196375-01)
C2	RHI02	0.00 to 5.00 A	0.00 to 5.00 A	N/A	Screw terminal	Strain relief NI–9971 (196375-01)
C3	RHI03	0.00 to 5.00 A	0.00 to 5.00 A	N/A	Screw terminal	Strain relief NI–9971 (196375-01)

TABLE B.2.—COMPONENT SPECIFICATIONS

[Reference Figure A.3 and Figure A.4 for piping and instrumentation diagram (P&ID).]

Item	P&ID identifier	Display range, nom (cal)	Signal out, nom (cal) for range	Excitation or power	Electrical interface	Mechanical interface
C4	RHI04	0.00 to 5.00 A	0.00 to 5.00 A	N/A	Screw terminal	Strain relief NI–9971 (196375-01)
C5	RHI11	– 10 to 10 mA	– 10 to 10 Vdc	N/A	BNC	Screw terminals
Heater						
H1	HR11	N/A	N/A	0 to 300 Vdc	Flying leads	Cartridge heater (press fit)
H2	HR12	N/A	N/A	0 to 300 Vdc	Flying leads	Cartridge heater (press fit)
H3	HR21	N/A	N/A	0 to 300 Vdc	Flying leads	Cartridge heater (press fit)
H4	HR22	N/A	N/A	0 to 300 Vdc	Flying leads	Cartridge heater (press fit)
H5	HR31	N/A	N/A	0 to 300 Vdc	Flying leads	Cartridge heater (press fit)
H6	HR32	N/A	N/A	0 to 300 Vdc	Flying leads	Cartridge heater (press fit)
H7	HR41	N/A	N/A	0 to 300 Vdc	Flying leads	Cartridge heater (press fit)
H8	HR42	N/A	N/A	0 to 300 Vdc	Flying leads	Cartridge heater (press fit)
H9	HS01	0 to 300 Vdc	0 to 300 Vdc	0 to 300 Vdc	Flying leads	19 in. rack mount
H10	RS01	–10 to 10 kV	–10 to 10 kV	–10 to 10 kV	Flying leads	19 in. rack mount
Mass flow rate						
Q1	CFM01	0.08 to 2 L/min, –40 to 120 °C	0 to 5 Vdc,	12 to 32 Vdc	1/2 in. conduit	1/2 in. AN
Q2	CFM02	0.08 to 2 L/min, –40 to 120 °C	0 to 5 Vdc	12 to 32 Vdc	1/2 in. conduit	1/2 in. AN
Q3	FMC01	0 to 800 torr (0.0 to 800.3)	0 to 5.00 Vdc	12 to 30Vdc	8 pin mini DIN connector	1/8 nominal pipe thread (NPT) both sides
Q4	FMC01-1	0 to 800 torr (0.0 to 800.3)	0 to 5.00 Vdc (analog set point)	12 to 30Vdc	8 pin mini DIN connector	1/8 NPT both sides
Q5	FMC02	0 to 800 torr (0.0 to 800.3)	`	12 to 30Vdc	8 pin mini DIN connector	1/8 NPT both sides
Q6	FMC01-1	0 to 800 torr (0.0 to 800.3)	0 to 5.00 Vdc (analog set point)	12 to 30Vdc	8 pin mini DIN connector	1/8 NPT both sides
Power						
J1	SJ01	0 to 5 kW	4 to 20 mA	24 V loop powered	14–22 Ga / screw terminal	M5 or #10 × 2 through holes
J2	SJ02	0 to 1 kW	4 to 20 mA	24 V loop powered	14–22 Ga / screw terminal	M5 or #10 × 2 through holes
Pressure						
P1	FPT01	0 to 75 psia	0 to 5.0 Vdc (0.0434 to 5.0427 Vdc)	10 to 30 Vdc	4 pin bayonet connector	#4 male face seal swivel
P2	FPT02	0 to 75 psia	0 to 5.0 Vdc (0.0434 to 5.0427 Vdc)	10 to 30 Vdc	4 pin bayonet connector	#4 male face seal swivel
P3	VPT01	3.75×10^{-9} to 7,500 torr	0 to 10.0 Vdc (1.8 to 8.6 Vdc)	15 to 30 Vdc	Connector B 4707 283 MA	DN 40 CF-F

TABLE B.2.—COMPONENT SPECIFICATIONS

[Reference Figure A.3 and Figure A.4 for piping and instrumentation diagram (P&ID).]

Item	P&ID identifier	Display range, nom (cal)	Signal out, nom (cal) for range	Excitation or power	Electrical interface	Mechanical interface
P4	CPT01	0 to 75 psia	0 to 5.0 Vdc (0.0434 to 5.0427 Vdc)	10 to 30 Vdc	4 pin bayonet connector	#4 male face seal swivel
P5	CPT02	0 to 75 psia	0 to 5.0 Vdc (0.0434 to 5.0427 Vdc)	10 to 30 Vdc	4 pin bayonet connector	#4 male face seal swivel
P6	FPT03	3.75×10^{-9} to 7,500 torr	0 to 10.0 Vdc (1.8 to 8.6 Vdc)	15 to 30 Vdc	Connector B 4707 283 MA	DN 40 CF-F
P7	FPS01	Close on falling pressure	1.6 – 27.0 inHg, set point <130 torr (<3 psia)	3A at 28 Vdc	12 in., 20 ga polyvinyl chloride (PVC) wire leads	Pressure port 1/8-27 NPT
P8	FPS03	Open on rising pressure	4.5 to 100 psi, S.P.>980 torr (>19 psia)	3A at 28 Vdc	12 in., 20 ga PVC wire leads	Pressure port 1/8-27 NPT
P9	FPS04	Open on rising pressure	4.5 to 100 psi, S.P.>980 torr (>19 psia)	3A at 28 Vdc	12 in., 20 ga PVC wire leads	Pressure port 1/8-27 NPT
Temperature						
T1	AT01	–60 to 175 °C	–2.397 to 8.138 mVdc, per temperature per conversation table for a standard type T thermocouple	N/A	Male “T” mini connector	6 in. × 0.062 in. dia. probe, 316SS
T2	CTS01	0 to 100 °C	100 Ω Resistor, 0.00385 Ω/Ω/°C	1 mA (NI–9217)	3 ft flying leads	1/8 in. sheath - use nylon ferrule
T3	CTS02	0 to 100 °C	100 Ω Resistor, 0.00385 Ω/Ω/°C	1 mA (NI–9217)	3 ft flying leads	1/8 in. sheath - use nylon ferrule
T4	CTS03	0 to 100 °C	100 Ω Resistor, 0.00385 Ω/Ω/°C	1 mA (NI–9217)	3 ft flying leads	1/8 in. sheath - use nylon ferrule
T5	CTS04	0 to 100 °C	100 Ω Resistor, 0.00385 Ω/Ω/°C	1 mA (NI–9217)	3 ft flying leads	1/8 in. sheath - use nylon ferrule
T6	----------	----------	----------	----------	----------	----------
T7	----------	----------	----------	----------	----------	----------
T8	CTS21	–60 to 175 °C	–2.153 to 7.977 mVdc, per T/C tables	N/A	Male “T” mini connector	1 in. × 0.8 in. surface mount pad
T9	CTS22	–60 to 175 °C	–2.153 to 7.977 mVdc, per T/C tables	N/A	Male “T” mini connector	1 in. × 0.8 in. surface mount pad
T10	CTS23	–60 to 175 °C	–2.153 to 7.977 mVdc, per T/C tables	N/A	Male “T” mini connector	1 in. × 0.8 in. surface mount pad
T11	CTS31	–60 to 175 °C	–2.153 to 7.977 mVdc, per T/C tables	N/A	Male “T” mini connector	1 in. × 0.8 in. surface mount pad
T12	CTS32	–60 to 175 °C	–2.153 to 7.977 mVdc, per T/C tables	N/A	Male “T” mini connector	1 in. × 0.8 in. surface mount pad
T13	CTS33	–60 to 175 °C	–2.153 to 7.977 mVdc, per T/C tables	N/A	Male “T” mini connector	1 in. × 0.8 in. surface mount pad
T14	CTS41	–60 to 175 °C	–2.153 to 7.977 mVdc, per T/C tables	N/A	Male “T” mini connector	1 in. × 0.8 in. surface mount pad
T15	CTS42	–60 to 175 °C	–2.153 to 7.977 mVdc, per T/C tables	N/A	Male “T” mini connector	1 in. × 0.8 in. surface mount pad
T16	CTS43	–60 to 175 °C	–2.153 to 7.977 mVdc, per T/C tables	N/A	Male “T” mini connector	1 in. × 0.8 in. surface mount pad
T17	CTS51	–60 to 175 °C	–2.153 to 7.977 mVdc, per T/C tables	N/A	Male “T” mini connector	1 in. × 0.8 in. surface mount pad
T18	CTS52	–60 to 175 °C	–2.153 to 7.977 mVdc, per T/C tables	N/A	Male “T” mini connector	1 in. × 0.8 in. surface mount pad

TABLE B.2.—COMPONENT SPECIFICATIONS

[Reference Figure A.3 and Figure A.4 for piping and instrumentation diagram (P&ID).]

Item	P&ID identifier	Display range, nom (cal)	Signal out, nom (cal) for range	Excitation or power	Electrical interface	Mechanical interface
T19	CTS53	–60 to 175 °C	–2.153 to 7.977 mVdc, per T/C tables	N/A	Male “T” mini connector	1 in. × 0.8 in. surface mount pad
T20	CTS61	–60 to 175 °C	–2.153 to 7.977 mVdc, per T/C tables	N/A	Male “T” mini connector	1 in. × 0.8 in. surface mount pad
T21	CTS62	–60 to 175 °C	–2.153 to 7.977 mVdc, per T/C tables	N/A	Male “T” mini connector	1 in. × 0.8 in. surface mount pad
T22	CTS63	–60 to 175 °C	–2.153 to 7.977 mVdc, per T/C tables	N/A	Male “T” mini connector	1 in. × 0.8 in. surface mount pad
T23	CTS71	–60 to 175 °C	–2.153 to 7.977 mVdc, per T/C tables	N/A	Male “T” mini connector	1 in. × 0.8 in. surface mount pad
T24	CTS72	–60 to 175 °C	–2.153 to 7.977 mVdc, per T/C tables	N/A	Male “T” mini connector	1 in. × 0.8 in. surface mount pad
T25	CTS73	–60 to 175 °C	–2.153 to 7.977 mVdc, per T/C tables	N/A	Male “T” mini connector	1 in. × 0.8 in. surface mount pad
T26	CTS81	–60 to 175 °C	–2.153 to 7.977 mVdc, per T/C tables	N/A	Male “T” mini connector	1 in. × 0.8 in. surface mount pad
T27	CTS82	–60 to 175 °C	–2.153 to 7.977 mVdc, per T/C tables	N/A	Male “T” mini connector	1 in. × 0.8 in. surface mount pad
T28	CTS91	–60 to 175 °C	–2.153 to 7.977 mVdc, per T/C tables	N/A	Male “T” mini connector	1 in. × 0.8 in. surface mount pad
T29	CTS92	–60 to 175 °C	–2.153 to 7.977 mVdc, per T/C tables	N/A	Male “T” mini connector	1 in. × 0.8 in. surface mount pad
T30	RTS01	–190 to 370 °C	–5.730 to 15.133 mVdc, per T/C tables	N/A	Male “K” mini connector	Cement on surface mount
T31	RTS02	–190 to 370 °C	–5.730 to 15.133 mVdc, per T/C tables	N/A	Male “K” mini connector	Cement on surface mount
T32	RTS03	–190 to 370 °C	–5.730 to 15.133 mVdc, per T/C tables	N/A	Male “K” mini connector	Cement on surface mount
T33	RTS04	–190 to 370 °C	–5.730 to 15.133 mVdc, per T/C tables	N/A	Male “K” mini connector	Cement on surface mount
T34	RTS11	–190 to 370 °C	–5.730 to 15.133 mVdc, per T/C tables	N/A	Male “K” mini connector	Cement on surface mount
T35	RTS12	–190 to 370 °C	–5.730 to 15.133 mVdc, per T/C tables	N/A	Male “K” mini connector	Cement on surface mount
T36	RTS13	–190 to 370 °C	–5.730 to 15.133 mVdc, per T/C tables	N/A	Male “K” mini connector	Cement on surface mount
T37	RTS21	–190 to 370 °C	–5.730 to 15.133 mVdc, per T/C tables	N/A	Male “K” mini connector	Cement on surface mount
T38	RTS22	–190 to 370 °C	–5.730 to 15.133 mVdc, per T/C tables	N/A	Male “K” mini connector	Cement on surface mount
T39	RTS23	–190 to 370 °C	–5.730 to 15.133 mVdc, per T/C tables	N/A	Male “K” mini connector	Cement on surface mount
T40	RTS31	–190 to 370 °C	–5.730 to 15.133 mVdc, per T/C tables	N/A	Male “K” mini connector	Cement on surface mount
T41	RTS32	–190 to 370 °C	–5.730 to 15.133 mVdc, per T/C tables	N/A	Male “K” mini connector	Cement on surface mount
T42	RTS33	–190 to 370 °C	–5.730 to 15.133 mVdc, per T/C tables	N/A	Male “K” mini connector	Cement on surface mount
T43	RTS41	–190 to 370 °C	–5.730 to 15.133 mVdc, per T/C tables	N/A	Male “K” mini connector	Cement on surface mount
T44	RTS42	–190 to 370 °C	–5.730 to 15.133 mVdc, per T/C tables	N/A	Male “K” mini connector	Cement on surface mount

TABLE B.2.—COMPONENT SPECIFICATIONS

[Reference Figure A.3 and Figure A.4 for piping and instrumentation diagram (P&ID).]

Item	P&ID identifier	Display range, nom (cal)	Signal out, nom (cal) for range	Excitation or power	Electrical interface	Mechanical interface
T45	RTS43	–190 to 370 °C	–5.730 to 15.133 mVdc, per T/C tables	N/A	Male “K” mini connector	Cement on surface mount
T46	HTS11	–190 to 370 °C	–5.730 to 15.133 mVdc, per T/C tables	N/A	12 in. flying leads	Integrated with cartridge heater
T47	HTS12	–190 to 370 °C	–5.730 to 15.133 mVdc, per T/C tables	N/A	12 in. flying leads	Integrated with cartridge heater
T48	HTS21	–190 to 370 °C	–5.730 to 15.133 mVdc, per T/C tables	N/A	12 in. flying leads	Integrated with cartridge heater
T49	HTS22	–190 to 370 °C	–5.730 to 15.133 mVdc, per T/C tables	N/A	12 in. flying leads	Integrated with cartridge heater
T50	HTS31	–190 to 370 °C	–5.730 to 15.133 mVdc, per T/C tables	N/A	12 in. flying leads	Integrated with cartridge heater
T51	HTS32	–190 to 370 °C	–5.730 to 15.133 mVdc, per T/C tables	N/A	12 in. flying leads	Integrated with cartridge heater
T52	HTS41	–190 to 370 °C	–5.730 to 15.133 mVdc, per T/C tables	N/A	12 in. flying leads	Integrated with cartridge heater
T53	HTS42	–190 to 370 °C	–5.730 to 15.133 mVdc, per T/C tables	N/A	12 in. flying leads	Integrated with cartridge heater
Voltage						
V1	RHV11	–10 kV to 10 kV	–10 Vdc to 10 Vdc	N/A	BNC	Screw terminals
V2	RHV01	0 to 300 Vdc	0 to 300 Vdc	N/A	Flying leads	Screw terminals
V3	RHV02	0 to 300 Vdc	0 to 300 Vdc	N/A	Flying leads	Screw terminals
V4	RHV03	0 to 300 Vdc	0 to 300 Vdc	N/A	Flying leads	Screw terminals
V5	RHV04	0 to 300 Vdc	0 to 300 Vdc	N/A	Flying leads	Screw terminals
V6	FV01	0 to 120 Vac	0 to 120 Vac	N/A	Flying leads	Screw terminals
Pump						
A6	----------	----------	----------	----------	----------	----------
A7	VP02	N/A	N/A	110 Vac	Grounded Edison plug	TBD
Valve, diverter						
A8	CFC01	N/A	N/A	24 Vdc, 0 .25 A run, 5 A load rated	Screw terminal, 18 Ga	1/2 in. NPT female ports
A8	CFC01-1	N/A	N/A	0–5 Vdc, degree of open/close	Screw terminal, 18 Ga	1/2 in. NPT conduit
Valve, solenoid						
A1	FSV01	N/A	N/A	24 Vdc, 0.25 A, 6 W	0.25 in. spade terminals	Port, 1/8 in.–27 NPT female thread
A2	FSV02	N/A	N/A	24 Vdc, 0.25 A, 6 W	0.25 in. spade terminals	Port, 1/8 in.–27 NPT female thread
A3	FSV03	N/A	N/A	24 Vdc, 0.25 A, 6 W	0.25 in. spade terminals	Port, 1/8 in.–27 NPT female thread
A4	FSV04	N/A	N/A	24 Vdc, 0.25 A, 6 W	0.25 in. spade terminals	Port, 1/8 in.–27 NPT female thread
A11	FSV05	N/A	N/A	24 Vdc, 0.25 A, 6 W	0.25 in. spade terminals	Port, 1/8 in.–27 NPT female thread
A12	FSV06	N/A	N/A	24 Vdc, 0.25 A, 6 W	0.25 in. spade terminals	Port, 1/8 in.–27 NPT female thread

TABLE B.2.—COMPONENT SPECIFICATIONS

[Reference Figure A.3 and Figure A.4 for piping and instrumentation diagram (P&ID).]

Item	P&ID identifier	Display range, nom (cal)	Signal out, nom (cal) for range	Excitation or power	Electrical interface	Mechanical interface
A13	FSV07	N/A	N/A	24 Vdc, 0.25 A, 6 W	0.25 in. spade terminals	Port, 1/8 in.–27 NPT female thread
A5	VSV01	N/A	N/A	24 Vdc, 0.25 A, 6 W	0.25 in. spade terminals	Port, 1/4 in.–18 NPT female thread
A9	NSV01	N/A	N/A	24 Vdc, 0.25 A, 6 W	0.25 in. spade terminals	Port, 1/8 in.–27 NPT female thread
A10	VSV02	N/A	N/A	24 Vdc, 0.25 A, 6 W	0.25 in. spade terminals	Port, 1/8 in.–27 NPT female thread
A14	VSV03	N/A	N/A	24 Vdc, 0.25 A, 6 W	0.25 in. spade terminals	Port, 1/8 in.–27 NPT female thread

Appendix C.—Reactor Operating Procedure

An example of the reactor operating procedure. Plasma II Reactor test rig shown in Figure C.1.

TEST NAME: _____

TEST SAMPLE ID: _____

TEST DIRECTOR: _____ DATE: _____/_____/_____

TEST ENGINEER: _____ TIME: _____am / pm

	GAS SPECIES	BOTTLE LOT #	BOTTLE FILL DATE	TANK PRESSURE (psig)	
				INITIAL	FINAL
Test Gas					
Inert Gas					

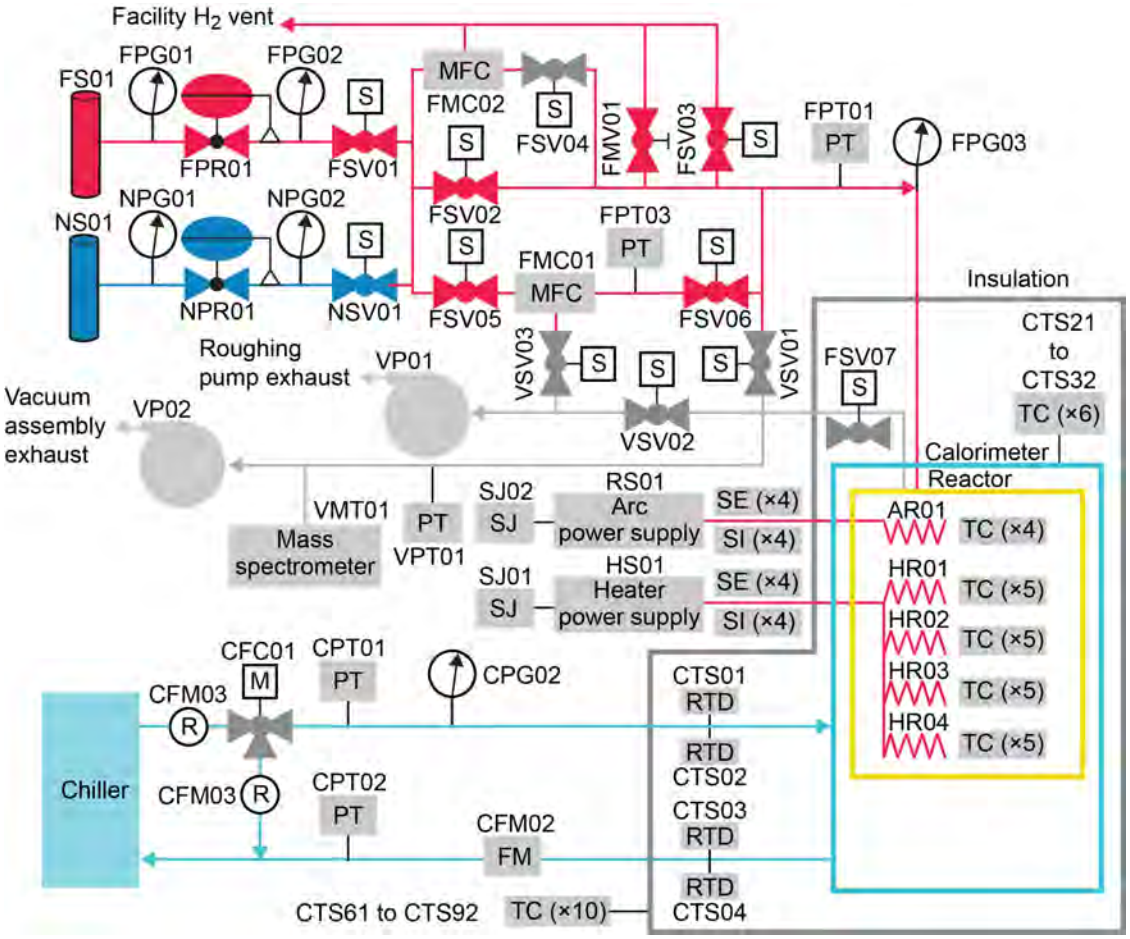

Figure C.1.—Plasma II reactor test rig, revision H.

	ITEM	COMPLETE (check and initial)
PRELIMINARY SETUP		
P.1	Verify test schedule per approved Plasma II Reactor Test Plan	_____
P.2	Update AEC Sample Travel Log	_____
P.3	Update test stand specific logbook to include scheduled test and test sample	_____
P.4	Turn on fume hood light by placing light switch on the fume hood pillar in the Up position	_____
P.5	Verify installation of appropriate test article	_____
P.6	Verify installation of insulation	_____
P.7	Verify proper gas bottles are properly installed into bottle holders	_____
P.8	Connect ground strap between test gas bottle and the dedicated test stand electrical ground	_____
P.9	Perform a visual inspection of all connections - Wiring between test cart and facility - Wiring between reactor and test cart - Plumbing within test cart - Plumbing between reactor and test cart - Plumbing between chiller and test cart	_____
P.10	Verify the following manual valves are closed: FS01 _____ NS01 _____ FMV01 _____ VMV01 _____	_____
P.11	Verify the following pressure regulators are fully backed out: FRP01 _____ NPR01 _____	_____
P.12	Turn on test cart by placing “24 VDC System Power” switch into the Up position	_____
P.13	Press E-STOP reset button on Plasma II Rig Test Stand	_____
P.14	Verify Vacuum (FPS01) and Coolant Flow (CPS01) Bypass switches are in the Up (E-STOP Bypass) position	_____
P.15	Verify Safety relay K1 has Power, CH. 1, and CH. 2 green LED are lit	_____
P.16	Exercise E-STOP Reset button on Plasma II Rig Test Stand to ensure that the latching button is in the “Run” (latched or “Up”) state	_____
P.17	Press E-STOP reset button on Plasma II Rig Test Stand	_____
P.18	Verify Safety relay K1 has Power, CH. 1, and CH. 2 green LED are lit	_____
P.19	Exercise E-STOP Reset button in the Operator area to ensure that the latching button is in the “Run” (latched or “Up”) state	_____

P.20	Press E-STOP reset button on Plasma II Rig Test Stand	_____
P.21	Verify Safety relay K1 has Power, CH. 1, and CH. 2 green LED are lit	_____
P.22	Turn on the roughing pump (VP01)	_____
P.23	Turn on the cRIO controller and data collection system by pressing the recessed power button on the Master controller chassis (CC1)	_____
P.24	Turn on the test computer	_____
P.25	Log into the test computer	_____
P.26	Select the Project.proj link to the LabVIEW project on the test computer Desktop	_____
P.27	Open and run the Plasma II Rig LabVIEW software, “Prelim” VI from the Project.proj	_____
P.28	Verify that the loaded Actuator List and Fault Table match latest version	_____
P.29	Verify that the thermocouples and pressure transducers are operational (all display ambient readings)	_____
P.30	Verify cRIO communication with all external devices - Arc Power Supply (RS01) - Heater Power Supply (HS01) - Diverter valve (CFC01) - Partial Pressure Controller (FMC01) - Test Gas Pressure Controller (FMC02)	_____
P.31	Verify Data Save is set to 15 seconds on the Data Control tab	_____
P.32	Verify four-(4) coolant isolation valves are in open configuration	_____
P.33	Turn on Facility chiller (CS01)	_____
P.34	Set coolant flow rate by adjusting the chiller to desired control set point by using the chiller front panel menu Set point = _____ °C	_____
P.35	Visually verify coolant flow using rotometers (CFM03 and CFM04)	_____
P.36	Set chiller to desired control on *Process Diagram* Tab set point by turning on CFC01-1, setting the control set point, then turn off CFC01-1 Flow Rate = _____ grams/second	_____
P.37	Turn on fume hood exhaust fan by pressing the green push-button on the fume hood tower	_____
P.38	Verify that the lecture bottles are closed	_____
P.39	Verify the following pressure regulators are fully backed out: FRP01 _____ NPR01 _____	_____
P.40	Verify Vacuum (FPS01) and Coolant Flow (CPS01) Bypass switches are in the Down (E-STOP Enable) position	_____

P.41 If the system is ≥ 780 Torr/15 psia, open manual FMV001 to vent the system to atmospheric pressure. Close the valve once the system is fully vented. _____

P.42 Turn on the roughing pump assembly (VP01) _____

P.43 Open the following valves: _____

FSV06 _____ FSV07 _____ VSV01 _____ VSV02 _____ VSV03 _____

P.44 Set low-pressure mass flow controller (FMC01) to 5 Torr _____

P.45 Turn on the Turbomolecular vacuum pump assembly (VP02) _____

P.46 Wait for the green "Status" light on turbo pumping station (VP02) to blink _____

P.47 Press the Start/Stop button to activate the pumping station _____

P.48 Wait for VPT01 < $1x10^{-2}$ Torr _____

P.49 From the Process Diagram panel of the LabVIEW screen, manually de-energize FSV02 and VSV02 _____

P.50 Turn on heater power supply (HS01) _____

P.51 Set heater power supply to test-specific power level _____
Voltage _____ Vdc Current _____ Amps Power _____Watts

P.52 Wait for calculated power (CA001) to stabilize (dP/dt ≤ 2 Watts/hour) _____

P.53 Verify VPT01 < $5x10^{-5}$ Torr _____

P.54 Prop open both lab doors to minimize lab space thermal fluctuations _____

P.55 Verify that the RGA is connected to designated laptop computer _____

P.56 Turn on and configure RGA _____

P.56.1. On RGA test computer, select the "RGA" shortcut on the desktop. _____

P.56.2. From the dropdown Menu under *Head* select "Connect List Setup" in the dialog window that appears _____

P.56.3. Select Refresh _____

P.56.4. Highlight the RGA on Com 1 _____

P.56.5. Select Connect _____

P.56.6. Turn on the RGA Filament Head by selecting "Filament On" under *Head* in the dropdown menu _____

P.56.7. Verify that the scan range is set correctly (0 to 42 AMU) by selecting Scan Parameters under the *Scan* dropdown menu _____

P.56.8. Format RGA Graph by simultaneously pressing "ctrl+K" _____

P.56.9. Select "Total Pressure" under *Utilities* from the dropdown menu

P.56.10. Select “Start” under *Scan* from the dropdown menu _____

P.57 Take baseline RGA scan and save as ASCII file for RGA Baseline _____

P.58 Verify FSV06 is closed _____

P.59 Turn on Camera _____

P.60 Turn on Closed Circuit TV _____

P.61 Open supply tank(s) isolation valves as required (FS01 and/or NS01) _____

P.62 Set test gas pressures on test gages using forward pressure regulators as required per test plan: _____

FPG02 for Hydrogen (FPR01) Set point = _____ psig

NPG02 for Inert (NPR01) Set point = _____ psig

P.63 Open supply valve FSV05 _____

P.64 Set low pressure controller set point (FMC01-1) to 5 Torr _____

P.65 Energize gas species specific isolation valve _____

FSV01 for H2/D2 NSV01 for Inert test gas

P.66 Follow the purge procedure at least seven-(7) times for purity

P.66.1 Set low pressure controller set point (FMC01-1) to 5 Torr _____

P.66.2 Wait until FPT03 < 25 Torr _____

P.66.3 Set low pressure controller set point (FMC01-1) to 500 Torr _____

P.66.4 Wait until FPT03 = 500 ± 10 Torr _____

P.67 From the Process Diagram panel of the LabVIEW screen, manually de-energize the valves: _____

FSV07 _____ VSV01 _____

P.68 Set low pressure controller set point (FMC01-1) to 5 Torr _____

P.69 Open FSV006 _____

P.70 Set low pressure controller set point (FMC01-1) to Test pressure _____

P.71 Verify that the 1/8” audio port on the Mazur PRM-9000 Radiation Monitor is wired to the upper USB port on the Ludlum laptop computer _____

P.72 Turn on Mazur PRM-9000 Radiation Monitor _____

P.73 Verify that the Mazur Ext/Audio Output option is set to “Data” _____

P.74 Turn on Ludlum/Mazur laptop computer _____

P.75 Turn on Ludlum Model 2363 detector _____

P.75.1. Check the status of the battery. Change if <75% _____

Battery State of Charge = _____%

P.75.2. Verify that the detection type knob is set to “N+G” _____

P.75.3. Turn the sensitivity adjustment knob to “x10” _____

P.76 Select the “Ludlum and Mazur” shortcut on the Ludlum-specific computer _____

P.77 Choose whether or not to save or expunge the sampled data from the test _____

P.78 Verify that the values that appear on the screen match the values in the table below: _____

Ludlum Date:	<Today’s Date>
Ludlum Time:	<Computer Clock Time>
Test Location:	Plasma II
Header #1:	NASA GLENN
Header #2:	RESEARCH CENTER
Header #3:	SN: 316017
Header #4:	SN: PR343975
Header #5:	
Header #6:	

Calibration Due Date	06/17/2016
Neutron Cal Constant:	0350
Gamma Cal Constant:	1000
Time Constant:	02
Paralyzed Time:	098
Neutron Alarm:	1000.00
Gamma Alarm:	2000.00
Neutron + Gamma Alarm:	3000.00
Integrated Dose Alarm:	4000.0

P.78.1 If the values are not accurate, update the value in the table and select “Update Instrument.” Wait until the yellow “Progress” bar is 100% and re-check the values. Repeat as necessary. _____

P.78.2 Once all values are correct, select the “Instrument Set Up” button _____

P.78.3 Set the “Sample Time” control box to 15 seconds _____

P.79 Turn on the Tektronix® Oscilloscope _____

P.80 Verify that the Tektronix® Internal Ethernet Server is active _____

P.81 Open and run the Tektronix® LabVIEW software, “Tektronix 7000 Acquire Continuous Waveform” VI from the Project.proj _____

P.82 Turn on and configure Agilient E4411B Spectrum Analyzer _____

P.83 Turn on and configure Advantest R3265A Spectrum Analyzer _____

P.84 Turn on and configure Hitachi V-1585 Oscilloscope _____

P.85 Turn on and configure Tektronix TDS220 Oscilloscope _____

P.86 Turn on and configure Keithley 33900 Waveform Generator _____

P.87 Turn on and configure Vitrek 4700 Precision high voltage meter _____

P.88 If using the FLIR Thermal Camera, configure the camera per **Section F. Special Procedure #4: Configure FLIR Thermal Camera** _____

A. TESTING

A.1 If using powers within test sample, disconnect Heater (HS01) external control D-connector _____

A.2 Verify with Electrical Engineer that supporting oscilloscopes are on and properly configured _____

A.3 Ensure the borated polyethylene barriers are in position to shield line of sight between the reactor and test operator locations _____

A.4 Get verbal approval from Electrical Engineer and Test Director that the Arc Power may be supplied _____

A.5 Initiate a baseline RGA data scan _____

A.6 Save baseline RGA scan using the AEC nomenclature _____

A.7 From the website SpaceWeather.com (http://www.spaceweather.com/) record the 24-hour X-Ray level both here and in the test stand log book _____
24-Hour X-Ray Level: _____

A.8 Turn on the Arc power supply (RS01) _____

A.9 Pressurize reactor _____

If Test Pressure < 15 psia, use mass flow controller #1 (FMC01) to control reactor pressure

If Test Pressure ≥15 psia, use procedure outlined in section **F. Special Procedure #4: MANUAL OPERATION– High Pressure**

A.10 Manually operate the system as required per Approved test plan in Step # P.1 _____

A.11 Follow test Plan accordingly by adjusting the functional parameters within the ranges listed below: _____

Partial Pressure Controller (FMC01-1): 0 – 5 Vdc / 0 – 800 Torr
High Pressure Controller (FMC02-1): 0 – 5Vdc / 15 – 100 psia
Heater Power Supply (HS01-1): 0 – 5 Vdc / 0 – 300 Vdc
Diverter Valve (CFC01-1): Do **NOT** change control values!
Arc Power Supply (RS01):
Frequency: **By Test** Duty Cycle: 0 – 100%
Voltage Offset: **By Test** Amplitude: **By Test**

A.12 At the conclusion of testing, follow Shutdown procedures in section **B. SHUTDOWN** _____

B. SHUTDOWN

B.1. Set Arc Power to (RS01-1) to 0.0 Vdc _____

B.2. Turn off the Arc power supply (RS01) _____

B.3. If using powers within test sample, re-connect Heater (HS01) external control D-connector _____

B.4. Set Heater Power Supply (HS01-1) to 0.0 Vdc _____

B.5. Turn off the Heater power supply (HS01) _____

B.6. Record the pressure of each supply lecture bottle as indicated on FPG01 and NPG01 _____

B.7. Close supply tank isolation valves for FS01 and NS01 _____

B.8. Set chiller set point to 10 °C _____

B.9. Take last RGA scan and record per AEC nomenclature _____

B.10. Turn off Agilient E4411B Spectrum Analyzer _____

B.11. Turn off Advantest R3265A Spectrum Analyzer _____

B.12. Turn off Hitachi V-1585 Oscilloscope _____

B.13. Turn off Tektronix TDS220 Oscilloscope _____

B.14. Turn off Keithley 33900 Waveform Generator _____

B.15. Turn off Vitrek 4700 Precision high voltage meter _____

B.16. On the Ludlum-specific test computer, exit software package by selecting the "STOP" button _____

B.17. Shut down the Ludlum-specific test computer _____

B.18. Turn off the Mazur PRM-9000 radiation detector _____

B.19. Turn off the Ludlum PRISCILLA radiation detector _____

B.20. On the RGA-specific, test computer. In the RGA software

- B.20.1. Select "Stop Now" under *Scan* under the dropdown menu _____
- B.20.2. Select "Filament On" under *Head* under the dropdown menu to turn off the Filament _____
- B.20.3. From the dropdown Menu under *Head* select "Connect List Setup" in the dialog window that appears _____
- B.20.4. High-light the RGA on Com 1 _____
- B.20.5. Select disconnect _____
- B.20.6. Exit RGA software _____
- B.20.7. Shut down the RGA-specific test computer _____

B.21. Turn off Main Power Switch on the back of the RGA _____

B.22. Verify reactor temperature to drop below 80 °C as indicated by all channels RTS11 thru RTS43 _____

B.23. Turn off facility chiller (CS01) _____

B.24. Visually verify no coolant flow using rotometers (CFM03 and CFM04) _____

B.25. Verify the following pressure regulators are fully backed out: _____
FRP01 _____ NPR01 _____

B.26. Press the Start/Stop button (not its main power switch) on the turbomolecular vacuum pump station (VP02) _____

B.27. From the Process Diagram panel of the LabVIEW screen, manually de-energize the following valves: _____
FSV01 _____ FSV02 _____ FSV03 _____ FSV04 _____ FSV06 _____
FSV07 _____ NSV01 _____ VSV01 _____ VSV02 _____

B.28. From the Process Diagram panel of the LabVIEW screen, manually energize the following valves: _____
FSV05 _____ VSV03 _____

B.29. Cycle FMC01-1 between 5 and 500 Torr until FMC01 no longer rises above 10 Torr _____

B.30. De-energize solenoid valves FSV05 and VSV03 _____

B.31. Turn off the roughing pump _____

B.32. Verify that the supply lecture bottles are closed _____

B.33. If accessing the reactor to interact with the samples, follow Steps B.29.1 thru B.29.11, or skip to Step B.30

B.33.1. Open manual vent valve FMV01 _____

B.33.2. From the Actuator panel of the LabVIEW screen, manually energize FSV02 _____

B.33.3. Energize solenoid valve FSV01 _____

B.33.4. Dial in pressure regulator FPR01 until FPG01 indicates < 5 psig _____

B.33.5. Completely back out pressure regulator FPR01 _____

B.33.6. De-energize solenoid valve FSV01 _____

B.33.7. Energize solenoid valve NSV01 _____

B.33.8. Dial in pressure regulator NPR01 until NPG01 indicates < 5 psig _____

B.33.9. Completely back out pressure regulator NPR01 _____

B.33.10. De-energize solenoid valve NSV01 _____

B.33.11. Vent system to atmospheric pressure by slowly opening manual reactor vent valve (FMV03) until reactor pressure gauge (FPG03) indicates atmospheric pressure (14 ± 2 psia) _____

B.34. Press an E-STOP mushroom button to disable actuator bus power _____

B.35. Turn off fume hood exhaust fan by pressing the red push-button on the fume hood tower _____

B.36. Turn off fume hood light by placing light switch on the fume hood pillar in the down position _____

B.37. Once both inverted triangles are gone from the turbomolecular vacuum pump station (VP02) LCD, turn off its main power switch _____

B.38. Press the Quit button on the Process Display tab _____

B.39. Press the Quit button on the Prelim screen _____

B.40. Download the test data from the cRIO _____

B.41. Turn off the test cart by placing “24 VDC System Power” switch into the down position.

References

1. Armstrong, R.J.; and Bennett, T.K.: Electric Breakdown in Deuterium and Hydrogen at Low Pressures. J. Appl. Phys., vol 82, no. 5, 1996, pp. 2147–2149.
2. National Aeronautics and Space Administration: Procedures for Cleaning of Systems and Equipment for Oxygen Service. NASA LAPG 1740.5, 2001.
3. ASTM G93–03(2011): Standard Practice for Cleaning Methods and Cleanliness Levels for Material and Equipment Used in Oxygen-Enriched Environments. ASTM International, West Conshohocken, PA, 2011.